

Université du Québec  
Institut National de la Recherche Scientifique  
Centre Énergie Matériaux Télécommunications

**Transmission Electron Microscopy studies of the nanostructural characteristics  
of the Inductively Coupled Plasma synthesized Silicon Nanowires**

Par  
Marta Antonella Agati

Thèse présentée pour l'obtention du grade de Philosophiae Doctor (Ph.D)  
en Sciences de l'énergie et des Matériaux

**Jury d'évaluation**

Président du jury et Examineur interne	Prof. Antonio Terrasi Università delgi Studi di Catania (Italy)
Examineur externe	Dr. Caroline Bonafos CEMES-CNRS (Toulouse, France)
Examineur externe	Prof. Paola Castrucci Università degli Studi di Roma Tor Vergata (Italy)
Directeur de recherche	Prof. My Ali El Khakani INRS-EMT (Varenes, QC, Canada)
Codirecteur de recherche	Dr. Simona Boninelli CNR-IMM (Catania, Italy)







# Acknowledgements

At the end of this PhD it is highly difficult to express the acknowledgement for everyone who offered his own personal and scientific contribution during these three intense years. While trying to go back to the beginning of the story, I think to what I gained from them in terms of knowledge and personal growth.

First of all, I would like to express my sincere gratitude for my supervisors: Prof. My Ali El Khakani (INRS-EMT, Canada), whose great experience and wisdom constitute an important inspiration for me, and Dr. Simona Boninelli (CNR-IMM, Italy), who represented a significant example as scientist and woman. I thank both of them for having given me the opportunity to develop this project in the frame of a “cotutelle” agreement between Italy and Canada, which was crucial for the project as well as for my working and personal experience. I would like to thank I would like to thank also Prof. G. Angilella who never denies his friendly attitude towards the students and always offered me his support in facing the difficulties of these years.

A special acknowledgement is dedicated to my friend and colleague Dr. Guillaume Amiard. I thank him not only for the feeling of security he managed to communicate to me in using the microscopes, but above all for his capability to conjugate a great scientific experience and knowledge with friendship and kindness.

I thank Prof. Paola Castrucci (Università di Roma Tor Vergata, Rome) for her important role during all the scientific discussions and for the kindness and availability she always demonstrates toward us; for her important work in this project and for her contribution in my economic support during the conferences and the travels abroad. With her and Prof. Maurizio De Crescenzi (Università di Roma Tor Vergata, Rome) I had also the opportunity to experience Scanning Tunneling Microscopy measurements in Rome during the first year. This was just the beginning of my experience of travelling for the PhD project and that is the time when a student is highly enthusiastic to learn from the experience developed by external scientific communities. I would like to thank them for having given me this opportunity and for having fulfilled my expectations.

I would like to thank also our scientific collaborators Prof. Stefania Pagliara and Dr. Stefano Ponzoni (Università Cattolica del Sacro Cuore, Brescia) who gave an significant contribution to the study of the ICP-SiNWs.

My sincere thanks go also to the electron microscopy team of CNR-IMM, including Corrado Bongiorno, Antonio Mio, Rosa Ruggeri, Mario Scuderi. I learnt a lot from their huge experience and their teaching was precious for my experience and knowledge.

Moreover, since no high-quality work can be pursued without the frame of a friendly work environment, I would like to thank my colleagues from the University of Catania and CNR-IMM (Adriana, Brunilde, Emanuele, Enrica, Giacomo, Giovanna, Giuseppe -Cacciato and Suriani- Laura, Lucia, Maria -Cantarella and Censabella-, Maria Josè, Martina, Saro, Vicky) as well as my colleagues from Montréal (Alessandra, Alessandro, Andrea, Catalin, Chiara, Dawitt, Dimitra, Domenico, Giacomo, Gianluca, Jonathan, Joy, Manuel, Massimiliano, Matteo -Basti and Duca-, Rajesh, Riccardo, Ruben, Simona, Stefania, Sudipta, Tomoyuki, Vincent, Zakaria).

A highly significant acknowledgement goes to my family, always supporting my choices although suffering each time at the airport, always giving me their support. One of my deepest feeling of acknowledgment is for Francesco, who was always present although the distance and sincerely shares with me the joyful moments and the troubles.

# RÉSUMÉ

Récemment, la recherche sur les nanomatériaux a atteint sa maturité puisque plusieurs applications de la nanotechnologie ont déjà rejoint le marché. À juste titre, plusieurs nanomatériaux se retrouvent déjà dans les produits de la vie quotidienne. Dans ce contexte, l'étude des matériaux à base de silicium (Si), pierre angulaire du développement de la microélectronique pendant les dernières décennies, conservera sans doute un rôle important dans le panorama scientifique et technologique. En particulier, les nanostructures de Si, grâce aux effets de confinement quantique (QC), peuvent avoir des propriétés améliorées et de nouvelles fonctionnalités par rapport au Si massif. Parmi les nanostructures de Si, les nanofils de Si, structure unidimensionnelle, soulèvent un grand intérêt de la part des chercheurs au cours des dernières années. En effet, les nanofils de Si ont été intégrés avec succès dans des dispositifs de détection chimique et biologique avec haute performance, dans des anodes de batterie au lithium de haute qualité et dans les dispositifs thermoélectriques. Les effets de QC dans les nanostructures de Si ont conduit à une émission optique remarquablement efficace, ce qui ne serait pas le cas pour le Si massif puisque il s'agit d'un matériau à bande interdite indirecte. Ceci ouvre la perspective d'aller vers des dispositifs nanophotoniques et photovoltaïques de nouvelle génération. De plus, l'émission optique des nanostructures de silicium peut être ajustée dans le visible en contrôlant la largeur de leur bande interdite, qui dépend directement de la taille de nanocristaux de silicium.

Dans cette perspective, ce projet de thèse porte sur l'étude des nanofils de Si synthétisés au moyen d'une nouvelle approche basée sur l'utilisation d'une torche de plasma inductif (connu sous le terme anglosaxon par Inductively coupled Plasma; ICP). La technique ICP est utilisée, depuis quelques années, pour la production industrielle de microsphères de Si au moyen d'un procédé de sphéroïdisation. Au cours de ce procédé de sphéroïdisation, il y a formation concomitante de nanostructures de silicium avec une large proportion de nanofils de Si, qui feront l'objet d'étude de cette thèse de doctorat. Nous nous sommes plus concentrés sur l'étude et la compréhension des mécanismes de croissance de ces nanofils de Si produits dans le système ICP, qui ont, entre autres, la particularité d'être le plus fins dans tous les nanofils rapportés dans la littérature à ce jour. Pour ce faire, nous avons adopté une approche basée sur les caractérisations par une foule de techniques de microscopie électronique à transmission (MET) pour étudier en profondeur les caractéristiques nanostructurales morphologiques et chimiques des nanofils de Si. Ainsi, des techniques liées à la microscopie électronique à transmission ont été utilisées, tels que l'énergie filtrée, le MET à haute résolution, la tomographie électronique, la spectroscopie par

rayons X, la cathodoluminescence, et la microscopie électronique à perte d'énergie. Nous avons ainsi pu identifier trois familles de nanofils de Si, à savoir, (i) les nanofils de Si avec un cœur cylindrique continu de Si (ayant des diamètres allant de 2 à 15 nm) entouré d'une couche concentrique de SiO<sub>2</sub> (ayant une épaisseur de 4 à 15 nm); (ii) les nanofils de Si dont le cœur en Si est formé d'un chapelet de nanocristaux sous forme d'amande connectés par un nanofil de Si très fin, et le tout enveloppé dans une couche de silice; et (iii) les nanofils de Si dont le cœur en Si est formé par une chaîne de nanocristaux de Si déconnectés les uns des autres et le tout est dans la croute nanocylindrique de silice (de 4 à 5 nm d'épaisseur). En étudiant ces différentes nanostructures de Si, nous avons pu mettre en évidence deux mécanismes de croissance compétitifs qui mènent à la croissance unidimensionnelle de ces trois classes de nanofils de Si via la technique ICP, à savoir la croissance assistée par l'oxyde et, dans une moindre mesure, la croissance catalysée par des nanoparticules de Fe issues des impuretés résiduelles de la poudre de silicium injectée initialement dans le réacteur ICP. Nous avons ensuite, mis l'accent sur la corrélation entre la caractérisation structurale de ces nanostructures de Si et leurs propriétés optoélectroniques par de mesures de photoluminescence (PL), l'objectif étant de confirmer l'émission dans le visible de ces nanostructures de Si, ce qui constitue une signature de la présence d'effets de confinement quantique dans nos nanofils produits par ICP. De plus, la mise au point d'un procédé de purification approprié a été développée par une méthode basée sur la centrifugation afin d'extraire les nanofils de Si du reste de la poudre de nano-silicium issue du procédé de sphéroïdisation par ICP.

Nous avons, enfin, étudié l'effet des traitements thermiques sur les changements nanostructuraux des nanofils-ICP, via des analyses MET in-situ et ex-situ. De cette manière, nous avons pu atteindre les conditions d'instabilité de Rayleigh et transformer structurellement les nanofils de Si en chaînes de nanocristaux de Si à une température de 1200°C. La formation « contrôlée » d'un tel nanocomposite a contribué à la compréhension de l'apparition de structures similaires dans les nanofils de Si tel que produits par ICP (non-recuits). Les propriétés optoélectroniques des nanofils de Si recuits ont été caractérisés par PL et les valeurs de leur émissions optiques ont été déterminés et corrélés avec les tailles des nanocristaux de Si (mesurées directement par MET). Puisque le procédé ICP constitue déjà une technique bien développée industriellement, ces études peuvent ouvrir la voie à l'optimisation du système ICP pour la synthèse intentionnelle de nanofils de Si en grand volume, répondant ainsi aux besoins des applications à grande échelle. Les propriétés optoélectroniques de ces nanofils-ICP (émission PL intense dans le visible et potentiellement contrôlable par une sélection fine de leurs diamètres) ouvre définitivement la voie à leur utilisation dans les futurs dispositifs nanophotoniques et photovoltaïques.

**Mots clefs:** microscopie électronique à transmission, nanofils de silicium, nanocristaux de silicium, torche de plasma inductif, propriétés optiques de silicium nanostructuré.

## SUMMARY

Recently, nanomaterial research has reached its maturity as long as several nanotechnology applications have reached the market. Deservedly, several nanomaterials can be found in every-day life items. In this regard, the study of Silicon (Si) based materials, which represented the cornerstone for the development of microelectronics in the past few decades, will most likely preserve an important role in the scientific and technological panorama. In particular, Si nanostructures have demonstrated to possess enhanced properties and even new functionalities with respect to their bulk counterpart via Quantum Confinement (QC) effects. Among Si nanostructures, Si nanowires (SiNWs), i.e. one dimensional Si nanostructures, have grasped a lot of interest from the researchers in the past few years. In fact, SiNWs have been successfully integrated into high-performance chemical sensing and bio-sensing devices, high-quality lithium battery anodes or thermoelectric devices. QC effects in Si nanostructures have been demonstrated to lead to an efficient optical emission, which is not possible in the bulk Si, as indirect band-gap material. This opens the possibility to prospect new generation nanophotonic and photovoltaic devices. Moreover, the optical emission of Si nanostructures can be tuned in the visible range by controlling the band-gap amplitude, which depends on the Si nanocrystal size.

In this perspective, this PhD project has been devoted to the study of SiNWs synthesized by means of a novel approach based on the exploitation of an inductively coupled plasma torch (indicated as Inductively Coupled Plasma; ICP). So far ICP technique was exploited for the industrial production of Si microspheres by means of a spheroidization process. During this process, the concomitant formation of Si nanostructures occurs, mostly constituted of SiNWs, which have been the subject of this PhD thesis. Here, it will be focused both the study and the understanding of the growth mechanism of these ICP-SiNWs, which have the characteristic of being the thinnest SiNWs reported in literature so far. To this aim, an approach based on Transmission Electron Microscopy (TEM) characterizations has been applied to thoroughly investigate the ICP-SiNW nanostructural morphological and chemical characteristics of the ICP-SiNWs. Hence, TEM related techniques have been used, i.e. Energy Filtered TEM (EFTEM), High Resolution TEM (HRTEM), electron tomography, Scanning TEM Energy Dispersive X-ray spectroscopy (STEM-EDX), cathodoluminescence (CL) and Electron Energy Loss Spectroscopy (EELS). In this way, it has been possible to identify three families of ICP-SiNWs, namely (i) cylindrical SiNWs having a continuous cylindrical Si core (with diameter between 2-15 nm) surrounded by a concentric SiO<sub>2</sub> shell (having thickness from 4 to 15 nm), (ii) SiNWs of which the Si core is represented by a

chapelet-like structure, constituted of almond-shaped Si nanocrystals (SiNCs) connected via a very-thin SiNW, all surrounded by a silica shell, (iii) SiNWs of which the Si core is represented by a chain of SiNCs separated from each other, located along an otherwise silica nanocylinder (with thickness of 4-5 nm). By studying these different Si nanostructures, it has been possible to infer two competitive growth mechanisms which lead to the one dimensional growth of these three classes of SiNWs via the ICP technique, namely the oxide assisted growth (OAG) mechanism and, to a lesser extent, the catalyzed growth by means of iron (Fe) nanoparticles present as impurities in the Si powder initially injected in the ICP reactor as a feedstock. In addition, focus has been put on the correlation between the structural characterization of these ICP-Si nanostructures and their optical properties, probed via Photoluminescence (PL) spectroscopy, in order to confirm the visible emission of these Si nanostructures as a signal of the occurrence of QC effects in the ICP-SiNWs. Moreover, the design of a suitable purification process was developed via a centrifugation based method in order to separate the SiNWs from the residuals of the Si nanopowders produced by the main ICP spheroidization process.

As a further step of the project, the effect of thermal treatments on the nanostructural changes of ICP- SiNWs via both in-situ and ex-situ TEM analyses was studied. In this way, we were able to reach the Rayleigh instability conditions and structurally transform the SiNWs into SiNC chains as long as the temperature was set at 1200°C. The controlled formation of such nanocomposite contributed to the understanding of the occurrence of similar structures in the as-produced ICP-SiNWs (not annealed). The optoelectronic properties of the annealed SiNWs have been probed by means of PL spectroscopy and their optical emissions have been correlated with the SiNC sizes determined by the TEM characterizations. Since the ICP process already constitutes a well-developed technique for nanostructure synthesis at industrial scale, these studies may open the route for the optimization of the ICP system for the intentional synthesis of large volumes of SiNWs, matching the requirements of large-scale applications. The optical properties of ICP-SiNWs (intense PL emission in the visible range and potentially controllable by a precise selection of their diameter) also foster their application in future nanophotonic and photovoltaic devices.

**Keywords:** transmission electron microscopy, silicon nanowires, silicon nanocrystals, inductively coupled plasma, optical properties of nanostructured silicon.

## TABLE OF CONTENTS

<b>CHAPTER 1:</b> .....	<b>1</b>
<b>RELEVANCE OF LOW DIMENSIONAL SILICON FOR NANOTECHNOLOGY</b> .....	<b>1</b>
1.1. Market trend in the Si-based nanotechnology.....	1
1.2. Quantum confinement effects in Si nanostructures .....	4
1.2.a Bandgap engineering .....	6
1.2.b Correlation between theoretical models and experimental results .....	8
1.3. Context and objectives of the PhD Thesis.....	12
Bibliography .....	13
<b>CHAPTER 2:</b> .....	<b>16</b>
<b>GROWTH MECHANISMS OF SI NANOWIRES AND THEIR ASSOCIATED SYNTHESIS TECHNIQUES</b> .....	<b>16</b>
2.1. Growth Mechanisms for SiNW formation.....	16
2.1.a Vapor-Liquid-Solid mechanism.....	16
2.1.b Oxide Assisted Growth mechanism.....	22
2.2. Conventional techniques for SiNW synthesis .....	26
2.2.a Chemical Vapor Deposition.....	28
2.2.b Molecular Beam Epitaxy .....	30
2.2.c Laser ablation.....	31
2.2.d Thermal evaporation .....	32
2.3. Conclusions .....	33
Bibliography .....	34
<b>CHAPTER 3:</b> .....	<b>37</b>
<b>EXPERIMENTAL DETAILS</b> .....	<b>37</b>
3.1. Inductively Coupled Plasma for large scale production.....	37
3.1.a Micropowder synthesis .....	39
3.1.b Si Nanopowder synthesis .....	41
3.2. Transmission Electron Microscopy .....	42
3.2.a Spectroscopic and imaging techniques.....	47
3.2.b Electron tomography .....	52
3.3. Photoluminescence spectroscopy.....	54
3.4. Conclusions .....	56
Bibliography .....	56

<b>CHAPTER 4:</b> .....	<b>59</b>
<b>INVESTIGATION OF SiNWs SYNTHESIZED BY ICP</b> .....	<b>59</b>
4.1. Structural and chemical characterization .....	59
4.2. Growth mechanisms of ICP-produced SiNWs .....	64
4.2.a SiNWs produced by Oxide Assisted Growth mechanism.....	64
4.2.b SiNWs produced by Vapor Liquid Solid mechanism.....	68
4.2.c 3D reconstruction of VLS SiNWs by Scanning Transmission Electron Tomography .....	70
4.2.e Surface diffusion above the Fe catalyst .....	74
4.3. Quantum confinement effect in ICP-SiNWs .....	75
4.4. Conclusions .....	77
Bibliography .....	78
<b>CHAPTER 5:</b> .....	<b>80</b>
<b>SORTING PROTOCOL TO EXTRACT SiNWs</b> .....	<b>80</b>
5.1. Purification process performed by centrifugation .....	81
5.2. Photoluminescence tuning by size selection.....	83
5.3. Evaluation of the purification efficacy by SEM .....	85
5.4. Conclusions .....	87
Bibliography .....	88
<b>CHAPTER 6:</b> .....	<b>89</b>
<b>THERMAL TREATMENT TO FORM Si NANOCOMPOSITES VIA RAYLEIGH INSTABILITY</b> .....	<b>89</b>
6.1. Study of the thermal stability of SiNWs .....	90
6.1.a In situ TEM analyses.....	90
6.1.b Ex-situ analyses.....	92
6.2. Rayleigh instability.....	95
6.3. Conclusions .....	97
Bibliography .....	98
<b>CHAPTER 7:</b> .....	<b>100</b>
<b>Conclusions and perspectives</b> .....	<b>100</b>
7.1. Conclusions .....	100
7.2. Perspectives: exploitation of a novel ICP process.....	102





# **CHAPTER 1: RELEVANCE OF LOW DIMENSIONAL SILICON FOR NANOTECHNOLOGY**

## **1.1. Market trend in the Si-based nanotechnology**

After several decades of scientific research, the ongoing implementation of nanotechnology into the global market signs a crucial step in the research & development of new and highly performing nanomaterials, and this new trend has often been described as a novel industrial revolution. As an estimation of the assimilation of nanotechnology into the every-day life, the number of products incorporating nanomaterials has been evaluated to grow from 54 in 2005 to 1200 in 2015, with an average annual growth rate of ~110% (Fig. 1). A recent report states that the annual global market for nanotechnology based goods will reach US \$3.3 trillion by 2018 [GlobalInfoInc14]. Moreover, the Compound Annual Growth Rate in nanotechnology market has been expected to reach the ~17.5% during the 2016-2022 period [MarketOutlook15].

In this framework, silicon (Si) has been defined the cornerstone for the development of microelectronics in the past few decades. In 1947 Walter Brattain and John Bardeen, members of Solid State Physics Group headed by William B. Shockley, created the first transistor prototype, marking the beginning of the new era based on computer technology. For several decades, since its initial development, the performances of microelectronics devices were intuitively predicted by Moore, one of the founders of the Intel Corporation. Indeed, in the 1960s, he predicted that the number of transistors in an integrated chip would double every two years, implying the exponential increment of chips' power as well as the scaling down of Si-based devices [Moore65]. Device's miniaturization predicted by Moore's law inspired for decades the philosophy of the Silicon Valley and has been the bedrock for the computer companies as well as for the pioneers of computer science.

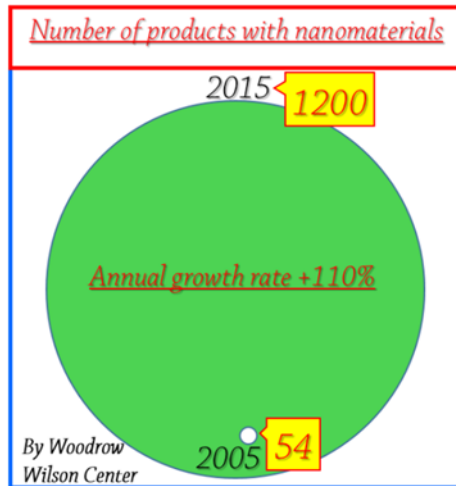


**Figure 1.1.** Number of products in the nanotechnology market containing nanomaterials.

Nevertheless, in the 1990s an inflection point in Moore’s law (see Fig. 2) has been remarked and nowadays it seems that this trend is not still valid because of the occurrence of serious obstacles which technology has to be faced with. The main limitations are related to: (i) lowered *device performances* (short channel effect becomes more important in miniaturized devices), (ii) *more complex fabrication processes* (extreme miniaturization causes an increase of production costs since more complex lithography and etching systems are required), (iii) *system performances* (related to interconnection length that becomes longer and longer, introducing increasing delay in the transmitted signals) [Xu12]. Nonetheless, at the beginning of this century innovative different approaches have been considered to overcome these limitations. The strategy developed within the so-called “More than Moore” approach consists into envisaging new functionalities of electronic devices that do not necessarily scale according to Moore's Law [ENIAC07]. This approach refers to a set of technologies enabling not necessarily digital micro- or nano-electronic functions; indeed, this trend tries to convert non-digital and non-electronic data, such as mechanical, thermal, acoustic, chemical, optical and biomedical functions, into digital ones and vice versa.

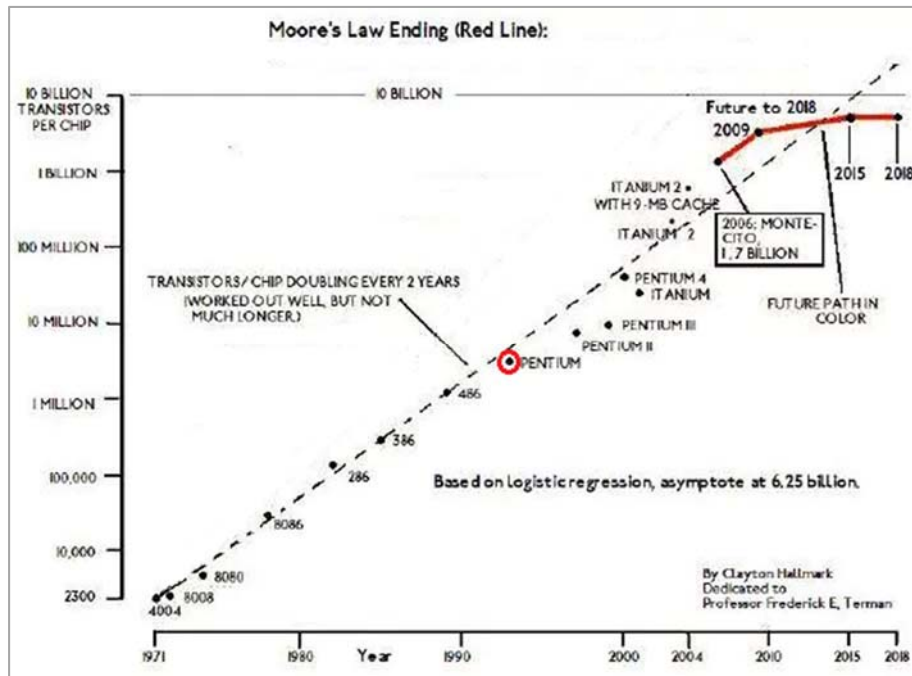


**Figure 1.2.** Illustration of Moore's law: the dashed line shows the doubling of transistors in a chip every two years. We can see that between 1990 and 2000 Moore's law had an inflection point. In general, Moore's trend is forecasted to slow down in the next years [webinfo].

In this contest, most likely Si will remain the material of choice for a wide range of applications in the future. Indeed, its natural abundance and its non-toxic nature contribute to preserve the role of Si as the material of choice to design future-generation applications. In addition, the existence of the well-established infrastructures and technologies of Si-based microelectronics, which bears a significant know-how on the material as well as the whole apparatus of processes and facilities, will favor the employ of Si for future applications. The most important contribute in the recent years has been given by the use of Si in solar panels, predominantly via the fabrication of polycrystalline Si-solar cells. Indeed, 90% of solar panels customized nowadays is made of Si-based materials [Priolo14]. Si-based photovoltaics has also reached a record in terms of the maximum attainable performance for single junction solar cells, for which it has been reported an efficiency of 25% [Zhao98], approaching the theoretical Shockley-Queisser limit of 33%.

In this context, a growing part of the scientific research has been devoted to the study of Si nanostructures in recent years, both from a fundamental and a technological viewpoints. The reason of the interest in low dimensional structures is due to their remarkable optical, electronic and chemical properties with respect to the bulk counterparts, because of the occurrence of both

quantum confinement (QC) phenomena and surface effects, the latter being related to their increased aspect-ratio. It is well known that bulk Si is an indirect band-gap material, thus preventing efficient optical emission and absorption. QC effects in Si nanostructures (which will be better discussed in the following paragraph) have been demonstrated to lead to an efficient optical emission, allowing the possibility to prospect nanophotonic devices as well as new generation photovoltaics. Si nanophotonic devices are easily integrable in the existent CMOS technology, while Si thin films or nanostructured solar cells can be cost effective in the long term and can potentially achieve higher efficiencies.

Silicon nanowires (SiNWs), in particular, have been targeted as a highly attractive component for optoelectronic or photovoltaic devices owing to the tunability of their optoelectronic properties through the control of their size via the QC effects [Lofaro15, Priolo14]. Moreover, following an approach inspired by the “more than Moore” philosophy, SiNWs have been successfully integrated into high-performance chemical sensing [McAlpine07] and bio-sensing devices [Li04] as a result of their surface-related sensitivity. Applications of SiNWs as high performance lithium battery anodes [Chan08] or thermoelectric devices [Hochbaum08] have been notably proposed as well.

## **1.2. Quantum confinement effects in Si nanostructures**

So far, the study of QC effects has brought a disruptive impact in the study of materials with ultra-low dimensionality, becoming important at the nanoscale, where at least one of the spatial coordinates of the system has dimensions of the order of the nanometer. In general, QC effects designate the occurrence of new phenomena, which are strictly related to the decrease of size and differentiate the nanomaterial with respect to its bulk counterpart. These include, to name but a few, QC Stark effect, Stokes shifts, non-linear optical properties [Pavesi10]. Nevertheless, a huge relevance has been given to the effects of QC in the optoelectronic properties of nanomaterials, in particular for semiconductors, where highly efficient light emission occurs since the overlap of the electrons and holes wavefunctions favors the radiative recombination channel [Barbagniovanni11, Priolo14]. The increasing of the radiative recombination probability results into a more efficient optical emission also from indirect-bandgap semiconductors as long as their dimensions are scaled down to the nanometer range. The Bohr radius, defined as the interdistance between an electron-hole pair in a semiconductor material, can be indicated as a reference length that settles the onset of QC phenomena [Koole14]. In Si, the Bohr radius has been calculated to be equal to 4.5 nm [Barbagniovanni12]. In

bulk indirect-bandgap materials, like Si, the lowest allowed optical transition is phonon-assisted, so that the radiative emission results to be inefficient. A scheme of the energy band diagram of bulk Si is represented in Fig. 3, where it can be observed that the optical transition in correspondence of the energy gap requires the assistance of a phonon. The overlap of the wavefunction induced by the spatial confinement is such that the uncertainty in momentum increases. In the k-space this implies that carriers can transit from different points of the Brillouine zone without the intermediation of phonons, necessary to preserve the momentum conservation, making the optical emission more efficient also for this otherwise indirect-bandgap semiconductor [Barbagiovanni11]. Thus, the ratio of no-phonon transitions respect to phonon-assisted processes increases, with the consequence that radiative transitions are governed by no-phonon quasi-direct events above confinement energies of about 0.7 eV [Kovalev98].

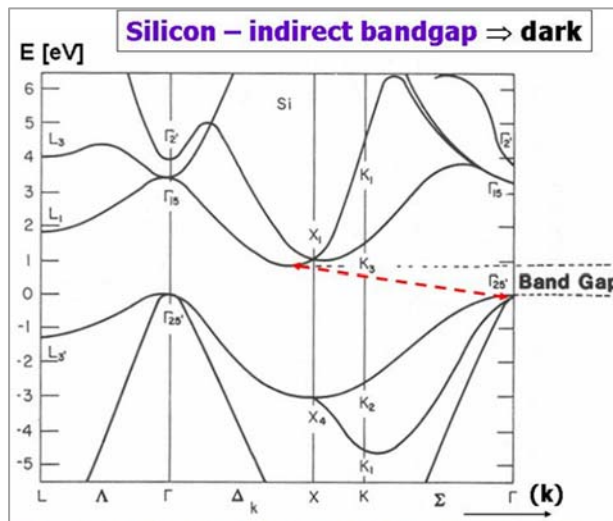


**Figure 1.3.** Energy band diagram of Si.

In the study of QC-related optical performances, an extraordinary interest has been devoted to Si nanostructures since these are considered well suited to constitute the optically active material in Si-based optoelectronic devices. Indeed, an enhancement of 5 orders of magnitude has been revealed for the radiative recombination rate of Si nanocrystals with respect the bulk counterpart [Priolo14], as an indication of the improvement of the optical efficiency in Si nanostructures.

## 1.2.a Bandgap engineering

The first experimental observation of QC effects in Si traces back to the discovery of light emission from porous Si done by L. Canham, which initiated the new era of Si-based photonics. Figures 4(a) and (b) depict two samples of porous Si with different porosity, while Fig. 4(c) shows the PL tuning as a function of the porosity changes. The detection of room temperature photoluminescence (PL) in the visible range as well as a color change with increasing the porosity have been assumed as an indication of the occurrence of QC [Canham90, Cullis97]. Since that moment, nanostructured Si has been extensively studied and its optical properties have been modeled.

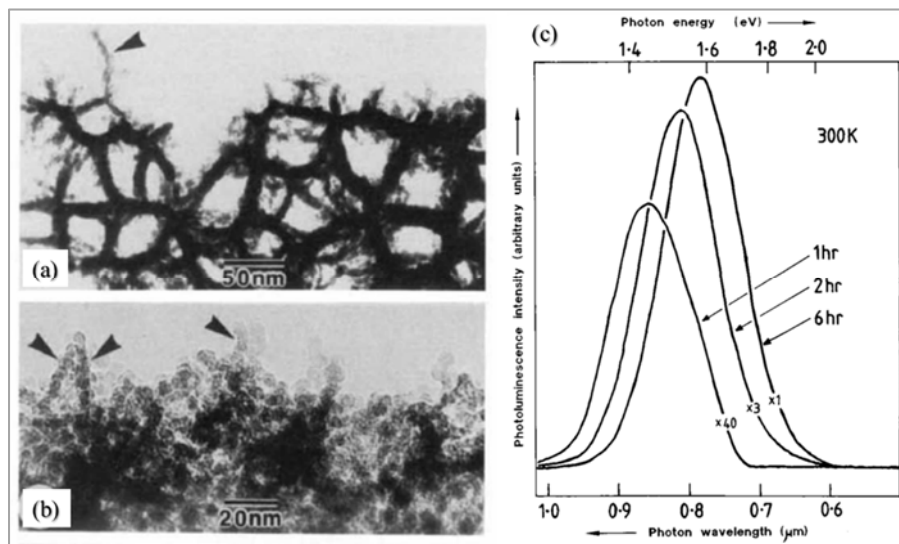


**Figure 1.4.** (a and b) Bright field TEM images of porous Si with decreasing porosity: (a) non-luminescent sample and (b) luminescent sample. (c) PL emission of porous Si synthesized by increasing the anodization time and, thus, the porosity [Cullis97].

Indeed, later on, further efforts have been devoted to the study of QC in Si nanocrystals (SiNCs). Several techniques were developed to produce colloidal SiNCs [Wen15], free-standing SiNCs [Dogan16] or SiNCs embedded in matrix [Zacharias02, Bonafos04, Iacona04]. The strong room temperature PL in the 650-1000 nm range as well as the redshift of the luminescence peak by increasing of the SiNC mean radius have been assumed as an indication of the occurrence of QC effects [Franzò08].

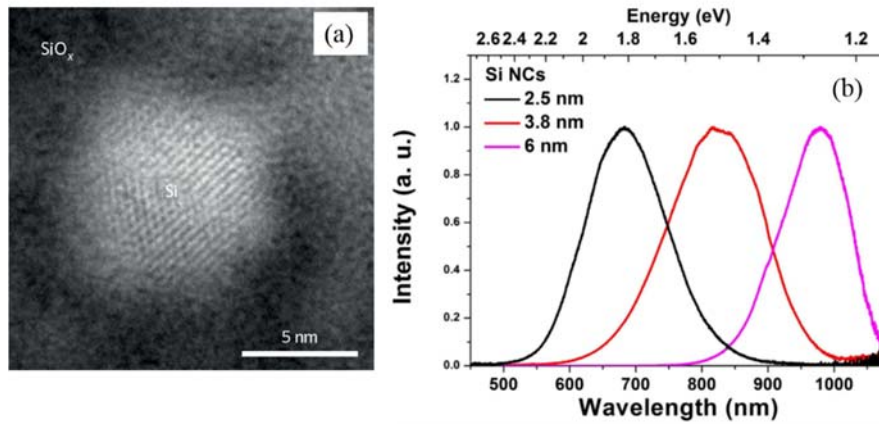


**Figure 1.5.** (a) Energy Filtered TEM image of a ~9 nm wide SiNC embedded into a SiO<sub>x</sub> matrix [Iacona04]. (b) Normalized PL intensity of SiNCs with different size. The wavelength shifts towards the blue while decreasing the SiNC diameter [Wen15].

Silicon nanocrystals, like that depicted in Fig. 5(a), are constituted by an ensemble of few atoms, being their typical sizes few nanometer wide. This implies that, as long as the dimensions are scaled down, the energy level distribution changes, becoming more similar to a discrete energy level distribution, which results into an enlargement of the energy band gap (Fig. 6). The size dependence of the energy gap is at the basis of the concept of bandgap engineering, which allows the tunability of the optical emission through the control of the size. Since bulk Si bandgap falls in the IR, being equal to 1.13 eV, the energy gap shifts towards the visible range.

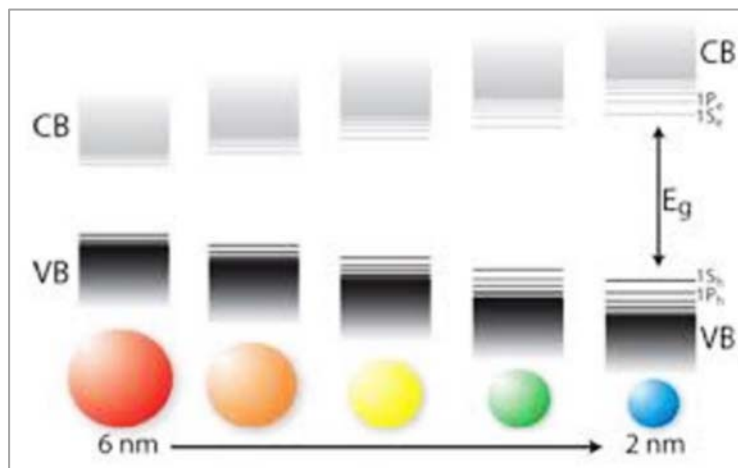


**Figure 1.6.** Illustration of bandgap enlargement and discretization of the energy levels induced by the decreasing of the size.

As a consequence, the occurrence of QC effects can be probed via the combined use of high resolution imaging techniques (such as Transmission Electron Microscopy) and photoluminescence measurements. The enlargement of the energy bandgap induces the shift of PL peak towards lower wavelengths with reducing the size, while the increasing of the radiative recombination probability leads to an enhancement of the intensity yield [Barbagiovanni11, Priolo14]. The blueshift of the optical emission is shown in Fig. 5(b) in the case of decreasing SiNC mean diameter.

More recently, SiNWs [Fig. 7(a)] have been targeted as a highly attractive component for optoelectronic devices owing to the tunability of their optoelectronic properties through the control of their size. Indeed, a blueshift of the PL peak with decreasing the diameter, as shown in Fig. 7(b), was ascribed to the QC of electrical carriers in two dimensions [Zhao04, Irrera12]. In literature, further studies of the electronic energy gap of very thin semiconducting nanowires confirmed the occurrence of QC effects in SiNWs [Ma03].

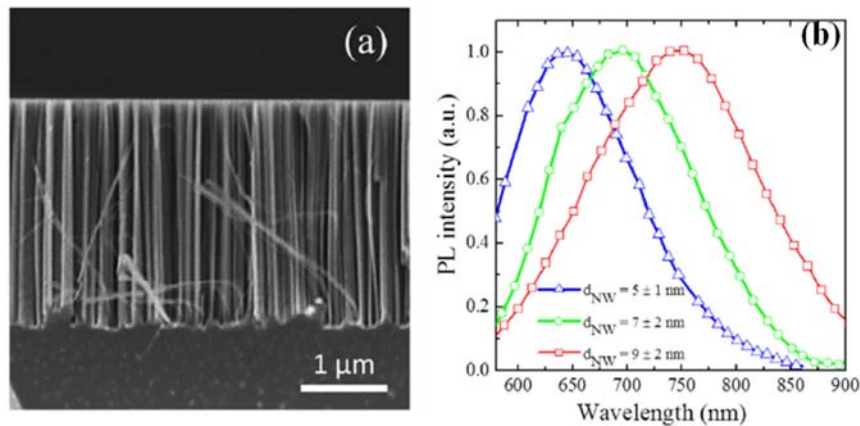


**Figure 1.7.** (a) SEM image of SiNWs synthesized via metal assisted chemical etching; (b) PL emission of SiNWs with different size [Irrera12].

### 1.2.b Correlation between theoretical models and experimental results

In literature, to calculate the electronic structure in Si nanostructures, the density functional theory has been applied. This approach requires the determination of the electronic density of states and the knowledge of the electronic wave states. In perturbative effective mass approximation (EMA) the reduction of the dimensions is introduced as a perturbation to the bulk

energy [Barbagiovanni12]. In practice, both electrons and holes are considered like particles in a box, where the amplitude  $a$  of the box is given by:

$$a_{e(h)} = \frac{4\pi\epsilon\hbar^2}{m_{e(h)}^*e^2} \quad (1)$$

which represents the Bohr radius. Here  $m_{e(h)}^*$  is the effective mass of the electron (hole),  $e$  is the electric charge,  $\epsilon$  is the dielectric constant. It is possible to individuate three regimes [Barbagiovanni12]:

- weak confinement, if the dimension of the system is much larger than both  $a_e$  and  $a_h$ ;
- medium confinement, if the dimension of the system is much smaller than  $a_e$  but larger than  $a_h$ , so that only the electrons experience QC;
- strong confinement, if the dimension of the system is much smaller than both  $a_e$  and  $a_h$ .

In EMA approach the energy levels are calculated starting from the Hamiltonian of a system of Coulombic interacting particles. The main characteristics of EMA relies in the choice of the basis set, which is expanded to reflect the use of an infinite confinement potential with a Bloch basis. Assuming the effective masses of the electrons and holes calculated using the DOS ( $m_e=1.08$  and  $m_h=0.57$ ) and  $\epsilon = 11.8$ , the calculation of the energy states leads to a quadratic dependence of the energy gap  $E_{gap}$  with respect to the diameter of SiNCs:

$$E_{gap} = E(\infty) + \frac{A}{D^2} eV \cdot nm^2 \quad (2)$$

where  $E(\infty)$  is the bulk energy bandgap, while the values of the parameter  $A$  take into account the effect of strong, medium or weak confinement and can be found in ref. [Barbagiovanni12]. Hence, the main result of EMA approach relies in the dependence of the  $E_{gap}$  on the inverse of the square of SiNC diameter. This model has been applied to describe the QC in SiNCs embedded in  $SiO_2$  synthesized via ion-implantation and microwave-plasma-decomposition as well as in SiNCs embedded in SiN [see Fig. 8, extracted from ref. Barbagiovanni12]. EMA provides an enough-simple approach to solve the energy level distribution in Si nanostructures.

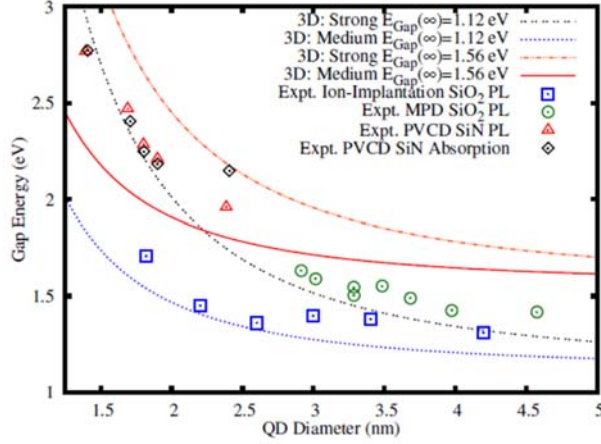


**Figure 1.8.** Crystalline and amorphous Si-Quantum Dots data and theoretical behavior predicted with EMA approach. ‘Expt. Ion-Implantation SiO<sub>2</sub>’ refers to crystalline Si QDs embedded in SiO<sub>2</sub> [Mokry09]. ‘Expt. microwave plasma decomposition (MPD) SiO<sub>2</sub>’ refers to crystalline Si QDs embedded in SiO<sub>2</sub> [Takagi90]. ‘Expt. plasma enhanced chemical vapor deposition (PCVD) SiN’ refers to amorphous Si QDs embedded in SiN [Park01]. Theoretical fits for strong and medium confinement are also shown considering  $E_{gap(\infty)} = 1.12$  or  $1.56$  eV (as labeled) in Eq. (2) [Barbagiovanni12].

A slightly more sophisticated approach considers the calculation of the electronic structure of Si crystallites using the linear combination of atomic orbitals (LCAO) methods [Delerue93]. In this case, the dimensional dependence of the bandgap energy exhibits an exponent equal to 1.39

$$E_{gap} = E(\infty) + \frac{3.73}{D^{1.39}} + \frac{0.881}{D} - 0.245 \quad (3)$$

where  $E_{gap}$  is eV and  $D$  is expressed in nm; the last two terms take into account a correction due to the change of the lattice parameter as a function of the size [Ledoux00]. This law accounts quite well for the experimental behavior of SiNCs with very narrow size distribution [Ledoux00], so that a strict correlation between the size and the optical emission of SiNCs can be attained. This constitutes the basis to understand the optical response of an ensembles of SiNCs with different sizes, typically given by a broad PL spectrum. Indeed, after the deconvolution of the PL peak into given spectral components, each component can be correlated with a given SiNC size through the Eq. (4).

Concerning QC in SiNWs, experiments and ab-initio studies have been performed on hydrogen-passivated SiNWs. Zhao et al. [Zhao04] employed the density functional theory with

the local density approximation and the many-body perturbation method based on the Green's function (GW) approximation to calculate the energy bandgap of hydrogen-passivated SiNWs oriented along both [110] and [111] directions. Since the effective mass in the confinement plane for the [111] wires is smaller than for the [110] wires, the energy upshift is expected to be larger for the [111] wires. Hence, in addition to a size dependence, the energy gap also depends on the NW growth direction. Moreover, calculations performed on SiNWs oriented along the [110] direction were corrected by evaluating the self-energy operator in the GW approximation (filled squares in Fig. 9). By fitting these data points with the function:

$$E_{gap} = E_{g,bulk} + \frac{const}{D^{1.7}} \quad (4)$$

where  $E_{g,bulk}$  is the bulk gap value and D is the NW diameter, the fit is compatible with the experimental point measured by Ma et al. [Ma03] (symbol \* in Fig. 9). Ma et al. [Ma03] performed also a study of the electronic properties of H-terminated SiNWs oriented along the [112] direction by using scanning tunneling spectroscopy (STS) measurements to evaluate their electronic bandgap (symbols + in Fig. 9). It can be seen from Fig. 9 that the bandgap for the SiNW having diameter equal to 7 nm is close to Si bulk value at 1.1 eV, and it increases first gradually and then steeply to a much larger value of 3.5 eV as the diameter decreases to 1.3 nm.

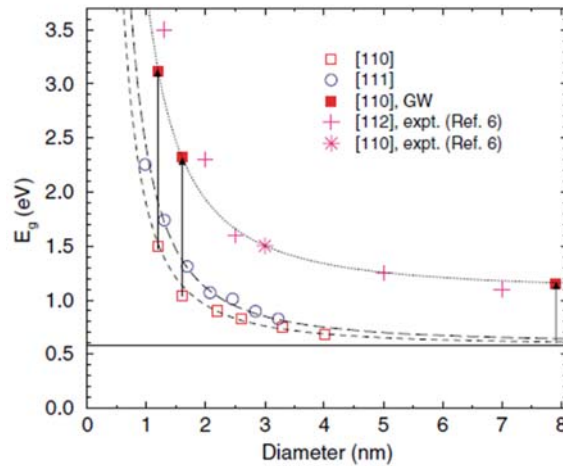


**Figure 1.9.** Local density approximation based calculations of the band gaps for [110] (empty squares) and [111] (empty circles) wires, and the GW-corrected gaps (filled squares) for the two thinnest [110] wires, compared with the measured gaps for [112] wires (+) and a [110] wire (\*). The dotted, dashed, and continuous lines are fitted to the data points [Zhao04].

Finally, a comparison between the optoelectronic properties shown by SiNCs and SiNWs can be drawn. It can be noted that the onset of QC effects is restricted to ultra-thin SiNW diameters, while it is slightly relaxed for SiNCs. This effect can be explained if one considers that in wire systems the confinement is limited only to two dimensions whereas clusters are 0D systems confined in all the three dimensions.

### **1.3. Context and objectives of the PhD Thesis**

This PhD project has been conducted in the framework of a co-tutelle agreement between the Physics and Astronomy Department of the University of Catania (Italy) and the Institut National de la Recherche Scientifique-Centre Énergie, Matériaux et Télécommunications (INRS-EMT, Varennes, Canada). A significant part of the research was conducted within the Institute for Microelectronics and Microsystems of the National Research Council (IMM-CNR, Catania). Moreover, this collaborative program involved also the University of Rome “Tor Vergata” and Tekna Plasma Systems Inc. (Sherbrooke, Canada).

The aim of the work was devoted to the investigation of the properties of Si based nanopowders found as a by-product during the inductively coupled plasma (ICP) process, usually performed by Tekna for the production of silicon microspheres. To this purpose, three classes of Si nanostructures have been extensively studied, namely SiNWs, chapelet-like Si nanostructures and SiNC chains, produced by the novel technique of ICP. Focus has been put on the correlation between the structural characterization of the Si nanostructures and their optical properties, in order to understand the occurrence of QC effects related to their nanosize. In this field, the knowledge of the state of the art in Si nanostructures synthesis approaches as well as the theoretical basis and the practical use of TEM-related techniques have been paramount.

In summary, an overview of the growth mechanisms at the basis of SiNW formation will be discussed in the second chapter, where also an extensive panorama of synthesis techniques currently employed for SiNW production is presented. More importantly, the difference between the experimental characteristics of the techniques and the physical/chemical mechanisms underpinning the SiNW assembly is pointed out. In the third chapter, the experimental equipment used for the synthesis of ICP-nanostructures and their structural, chemical and optical analyses are presented. The main results concerning the investigation of ICP-SiNWs will be illustrated in the fourth chapter, where the two competitive growth mechanisms driving the

growth of SiNWs are detailed. Finally, the visible to near-infrared broad photoluminescence of these ICP-SiNWs is shown and correlated with their TEM revealed nanostructural characteristics. In the fifth chapter, the optimized purification process that has been developed for the extraction of SiNWs from the by-product powder is described. In the sixth chapter, the effects of post-thermal annealing treatments on the nanostructural changes of SiNWs have been studied. In this way, we were able to reach the Rayleigh instability conditions and structurally transform the SiNWs into a more intriguing Si nanocomposite, made by SiNCs wrapped in a silica wire. Finally, the novel procedure developed by Tekna for the intentional synthesis of SiNWs via ICP is outlined as a new perspective which opens the route for the high-throughput production of ICP-SiNWs.

## Bibliography

[Barbagiovanni11] E. G. Barbagiovanni, L. V. Goncharova, and P. J. Simpson, Phys. Rev. B 83, 035112 (2011).

[Barbagiovanni12] E. G. Barbagiovanni, D. J. Lockwood, P. J. Simpson and L. V. Goncharova, J. Appl. Phys. 111, 3 (2012).

[Bonafos04] C. Bonafos, M. Carrada, N. Cherkashin, H. Coffin, D. Chassaing, G. B. Assayag, A. Claverie, T. Müller, K. H. Heinig, M. Perego, M. Fanciulli, P. Dimitrakis and P. Normand, J. Appl. Phys. 95, 10 (2004).

[Canham90] L. Canham, Appl. Phys. Lett. 57, 10 (1990).

[Chan08] C. K. Chan, H. Peng, G. Liu, K. McIlwrath, X. F. Zhang, R. A. Huggins and Y. Cui, Nat. Nanotech. 3, 1 (2008).

[Cullis97] A. G. Cullis, L. T. Canham, and P. D. J. Calcott, J. Appl. Phys. 82, 3 (1997).

[Delerue93] C Delerue, G Allan, M Lannoo, Phys. Rev. B 48, 15 (1993).

[Dogan16] I. Dogan and M. C. M. van de Sanden, Plasma Process. Polym. 13, 1 (2016).

[ENIAC07] European Nanoelectronics Initiative Advisory Council (ENIAC), Strategic Research Agenda, 2007 Edition.

[Franzò08] G. Franzò, M. Miritello, S. Boninelli, R. Lo Savio, M. G. Grimaldi, F. Priolo, F. Iacona, G. Nicotra, C. Spinella, and S. Coffa, J. Appl. Phys. 104, 9 (2008).

[GlobalInfoInc14] Global Information Inc. (2014), Nanotechnology, Freedonia Group, CT, USA.

[Hochbaum08] A. I. Hochbaum, R. Chen, R. D. Delgado, W. Liang, E. C. Garnett, M. Najarian, A. Majumdar and P. Yang, *Nature* 451, 7175 (2008).

[Iacona04] F. Iacona, C. Bongiorno, C. Spinella, S. Boninelli, and F. Priolo, *J. Appl. Phys.* 95, 7 (2004).

[Irrera12] A. Irrera, P. Artoni, F. Iacona, E. F. Pecora, G. Franzo, M. Galli, B. Fazio, S. Boninelli and F. Priolo, *Nanotechnology* 23, 7 (2012).

[Koole14] R. Koole, E. Groeneveld, D. Vanmaekelbergh, A. Meijerink and C. Donegá, Chapter 2 in *Nanoparticles – Workhorses in Nanoscience*, Springer-Verlag Berlin Heidelberg (2014).

[Kovalev98] D. Kovalev, H. Heckler, M. Ben-Chorin, G. Polisski, M. Schwartzkopff and F. Koch, *Phys. Rev. Lett.* 81, 13 (1998).

[Ledoux00] G. Ledoux, O. Guillois, D. Porterat, C., Reynaud, F. Huisken, B. Kohn and V. Paillard, *Phys. Rev. B* 62, 23 (2000).

[Li04] Z. Li, Y. Chen, X. Li, T. I. Kamins, K. Nauka and R. S. Williams, *Nano Lett.* 4, 2 (2004).

[Lofaro15] M. J. Lo Faro, C. D’Andrea, E. Messina, B. Fazio, P. Musumeci, R. Reitano, G. Franzò, P. G. Gucciardi, C. Vasi, F. Priolo, F. Iacona and A. Irrera, *Sci Rep.* 5, (2015).

[Ma03] D. D. D. Ma, C. S. Lee, F. C. K. Au, S. Y. Tong, S. T. Lee, *Science* 299, 5614 (2003).

[MarketOutlook15] RNCOS E-Services Pvt. Ltd. 2015, *Global Nanotechnology Market Outlook 2022*. Research Report, Can-Biotech Inc., Canada.

[McAlpine07] M. C. McAlpine, H. Ahmad, D. Wang and J. R. Heath, *Nat. Mater.* 6, 5 (2007).

[Moore65] G. E. Moore, *Electronics* 38, 8 (1965).

[Mokry09] C. R. Mokry, P. J. Simpson, and A. P. Knights, *J. Appl. Phys.* 105, 11 (2009).

[Park01] N. M. Park, C. J. Choi, T. Y. Seong, and S. J. Park, *Phys. Rev. Lett.* 86, 13 (2001).

[Pavesi10] L. Pavesi and R. Turan, *Silicon nanocrystals: fundamentals, synthesis and applications*. John Wiley & Sons (2010).

[Priolo14] F. Priolo, T. Gregorkiewicz, M. Galli and T. F. Krauss, *Nat. Nanotech.* 9, 1 (2014).

[Takagi90] H. Takagi, H. Ogawa, Y. Yamazaki, A. Ishizaki, and T. Nakagiri, *Appl. Phys. Lett.* 56, 2379 (1990).

[webinfo] <http://www.telegraph.co.uk/technology/2016/02/25/end-of-moores-law-whats-next-could-be-more-exciting/>.

[Wen15] X. Wen, P. Zhang, T. A. Smith, R. J. Anthony, U. R. Kortshagen, P. Yu, Y. Feng, S. Shrestha, G. Coniber and S. Huang, *Sci. Rep.* 5 (2015).

[Xu12] C. Xu, Process optimization for the 3D sequential integration of FDSOI CMOS transistors, PhD thesis, Grenoble University (2012).

[Zacharias02] M. Zacharias, J. Heitmann, R. Scholz, U. Kahler, M. Schmidt, and J. Bläsing, *Appl. Phys. Lett.* 80, 4 (2002).

[Zhao98] J. Zhao, A. Wang, M. A. Green and F. Ferrazza, *Appl. Phys. Lett.* 73, 14 (1998).

[Zhao04] X. Zhao, C. M. Wei, L. Yang and M. Y. Chou, *Phys. Rev. Lett.* 92, 23 (2004).

## **CHAPTER 2: GROWTH MECHANISMS OF SI NANOWIRES AND THEIR ASSOCIATED SYNTHESIS TECHNIQUES**

In this chapter the fundamental concepts and the state of the art on the Si nanowire (SiNW)-related research, that is at the basis of the present work, will be presented. It will address the treatment of SiNWs by doing the distinction between the growth mechanisms and the experimental techniques for their synthesis. Indeed, the structural and the optical investigation of SiNWs produced via the innovative Inductively Coupled plasma (ICP) technique has been pursued to understand their growth mechanism, in order to better control the SiNW production by means ICP. In this perspective, it could be advantageous to preliminary give an overview of the most well-established growth mechanisms of Si nanostructures and their associated synthesis techniques. These aspects will be treated in the first and second paragraphs, respectively.

### **2.1. Growth Mechanisms for SiNW formation**

The description of the mechanisms ruling the growth of nanostructures, and in particular of SiNWs, relies on the fact that their formation is induced by physical and chemical driving forces. The investigation of the mechanisms that lead to their assembly is the object of this paragraph, where the distinctions between the so-called Vapor-Liquid-Solid (VLS) growth mechanism and the Oxide Assisted Growth (OAG) of one-dimensional (1D) Si nanostructures are elucidated.

#### **2.1.a Vapor-Liquid-Solid mechanism**

Although the first report on filamentary Si structures traces back to the publication of Treuting and Arnold [Treuting57], the pioneering work of Wagner and Ellis [Wagner64] sets the basis for the research on 1D Si nanostructures growth. Even though the dimensions of the 1D Si whiskers they investigated were quite large [Fig. 1(a)], being of the order of 100 nm or even more, they opened the route towards the synthesis of innovative 1D nanostructures, since they clarified the growth mechanism responsible for the formation of these nanostructures. Indeed, the observation of no screw dislocations along the axial direction of the Si whiskers led them to

conclude that the anisotropic growth was attributable to the catalytic action of metallic impurities, previously deposited on a Si substrate, and not driven by the possible presence of dislocations [Wagner64].

Their claim relies on two main facts:

- a) no growth occurs in absence of the metallic particles;
- b) the Si whiskers present a metallic particle at their tip.

Hence, they explained the growth of the Si structures in terms of the so-called VLS mechanism. Since then, VLS mechanisms has represented the most common way to synthesize 1D Si structures and further efforts have been devoted to produce thinner and thinner Si whiskers, so the term of “Si nanowires” has been adopted [Wang08, Schmidt09, Schmidt10].

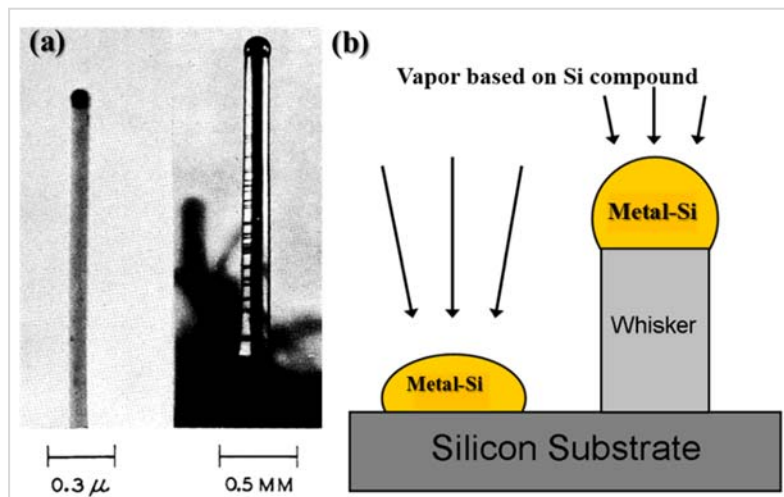


**Figure 2.1.** (a) Si whiskers synthesized via VLS mechanisms, firstly reported by Wagner and Ellis. [Wagner64]. It can be noted that the lateral dimensions were quite big, up to 0.2 mm. (b) Schematic of the 1D Si nanostructures growth via VLS.

A schematic of the VLS mechanisms is illustrated in Fig. 1(b). In the VLS mechanism, a Si compound in the vapor phase represents the precursor that supplies the Si material and is provided in the reaction chamber during the growth. A solid Si substrate is previously introduced into the chamber, whereas some metallic particles are present on the substrate surface. The metallic particles can be formed either in a previous step before the introduction of the substrate into the chamber [Schmidt09], or in situ prior to SiNW growth [Wang06]. The gaseous precursor impinges on the solid Si substrate, but is preferentially decomposed in correspondence of the metallic particles, because of their catalytic action. In this way, Si atoms are incorporated into the metallic particles, which are liquid at the experimental conditions set for the growth. More precisely, Si incorporation in the metal leads to the formation of a metal-Si alloy. At the eutectic

point, which corresponds to the experimental conditions set for the growth, the alloy is in liquid phase. Further absorption of Si atoms led to the supersaturation of Si in the alloy, thus precipitation of Si atoms occurs, then the Si atoms deposit layer-by-layer right under the droplet in a crystalline arrangement. In this way, 1D structures form only below the metallic particles, as sketched in Fig. 1(b). whereas negligible crystal growth takes place in correspondence of the other regions of substrate.

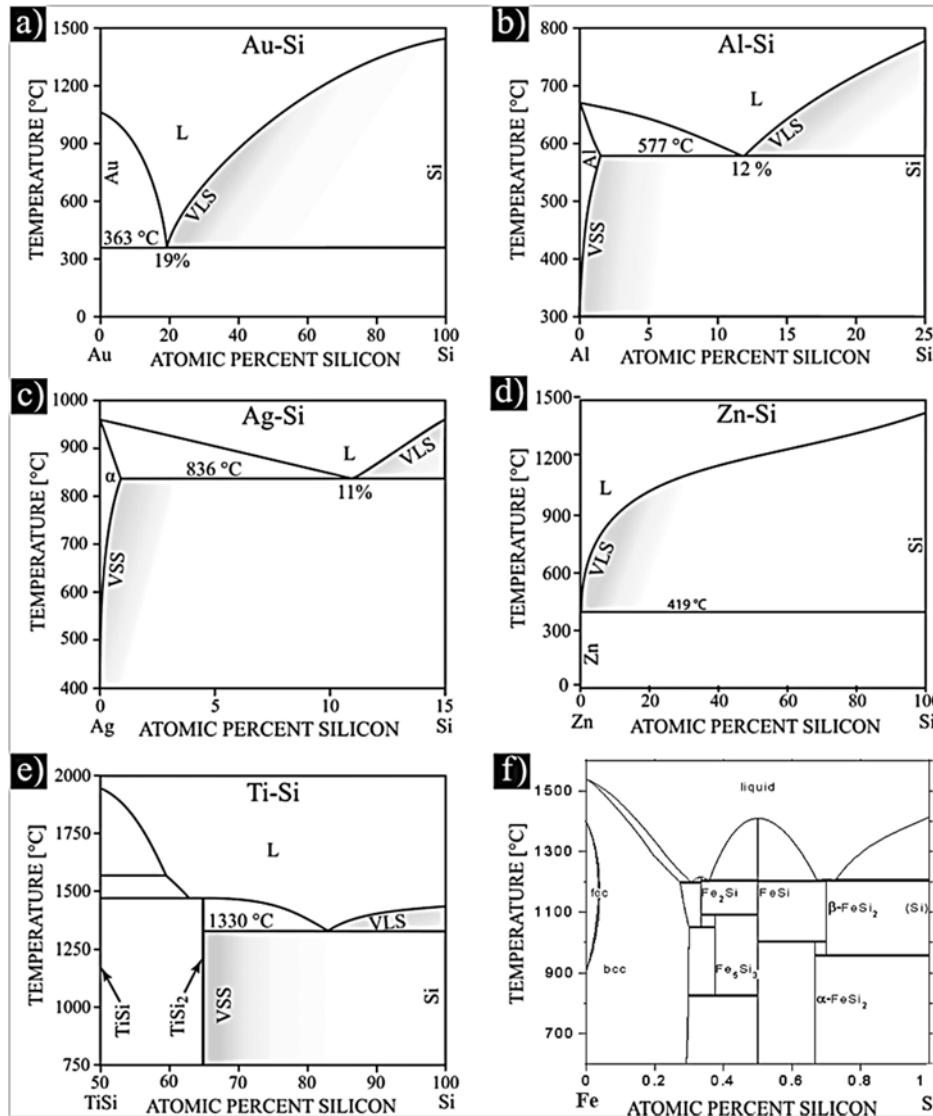


**Figure 2.2.** Phase-diagrams of some metal-Si alloys exploited for the synthesis of SiNWs: (a) Au, (b) Al, (c) Ag, (d) Zn, (e) Ti [Schmidt10] and (f) Fe [PDDatabase].

More general theoretical models have been developed to describe the anisotropic growth of a Si crystal based on the presence of a catalytic mediator [Wacaser09]. Indeed, it has been

observed that, similarly to a VLS mechanism, 1D growth can occur even if the metallic particle is solid during the growth [Wang06], or also in liquid and superfluid media [Davidson07, Tuan05]. These mechanisms are denoted as Vapor-Solid-Solid (VSS) and solution-liquid-solid (SLS) or supercritical-fluid-liquid-solid (SFLS) respectively [Wacaser09]. Moreover, vapor-adsorption-layer-solid [Bootsma71] and solid-liquid-solid mechanisms [Yu01] have been reported as well. In all these cases, the main driving force inducing SiNW formation can be described within the frame of a more general three-phase mechanism [Wacaser09]. The knowledge of binary metal-Si phase-diagrams (PD) is a fundamental prerequisite for the understanding of all these mechanisms, in particular to fix the temperature and the Si concentration corresponding to the eutectic point. The phase diagram also establishes whether the particle is liquid or solid at the experimental conditions set for the growth. The PDs of some of the most exploited metal catalysts for SiNW synthesis are shown in Fig. 2. It should be noted that, in general, for the eutectic alloys the lowering of the melting point with respect to the melting point of the single elements occurs. The theoretical description of the growth process can be developed fixing the three phases as for the VLS [Wang08]. So, if we indicate  $\sigma_L$ ,  $\sigma_S$ ,  $\sigma_{LS}$  as the surface tensions of the liquid, the solid and the liquid-solid interface respectively (Fig.3), we can set the following balance equation:

$$\sigma_L \cos\beta = \sigma_S - \sigma_{LS} \quad t = 0 \quad (1)$$

the time  $t=0$  indicates that this equation holds prior to the SiNW growth.  $\beta$  is the angle defined by the substrate surface and the perpendicular to the droplet at its contact point, so it is also called contact-angle and it is such that:

$$R = r_0 / \sin\beta \quad (2)$$

where  $r_0$  is the radius of the contact area and  $R$  is the radius of the droplet. A more clear vision of these physical quantities can be provided by the Fig. 3(a). An approach that takes into account the nanosize of the materials has been demonstrated to lead to an additional term to Eq. (1) [Rowlinson03]:

$$\sigma_L \cos\beta = \sigma_S - \sigma_{LS} - \tau / r_0 \quad t = 0 \quad (3)$$

where  $\tau$  is the line tension, defined as the excess of free energy per unit length calculated along the contact line of the three phases [Widom95]. Such a contact line is a circle of radius  $r_0$ , as it is

clarified by Fig. 3(a). After the transient time, when the first Si crystalline monolayer is formed [Fig. 3(b)], the SiNW grows. During the growth, it can be observed that the radius of the contact area diminishes, while the droplet approaches a spherical shape and nanowire flanks enlarge, in such a way that an angle  $\alpha$  is formed, as it can be seen in Fig. 3(c). So, at  $t \neq 0$  the Eq. (3) becomes:

$$\sigma_L \cos \beta = \sigma_S \cos \alpha - \sigma_{LS} - \tau / r_0 \quad t \neq 0 \quad (4)$$

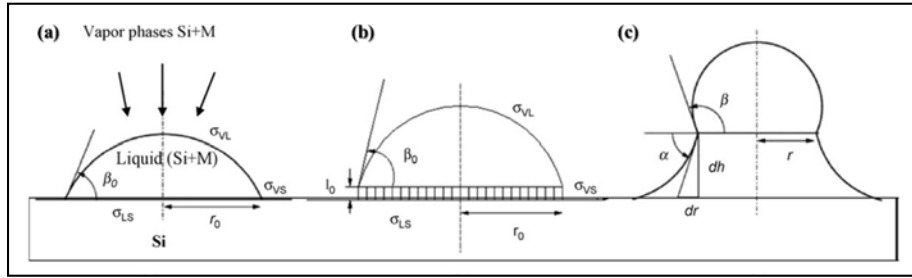


**Figure 2.3.** (a) Condition at  $t=0$ ; (b) early stage of SiNW growth, where the first Si crystalline monolayer is formed; (c) equilibrium condition for SiNW growth [Wang08].

The kinetics of NW growth is controlled by the so-called Gibbs-Thomson effect [Givargizov75], for which the growth rate is faster for larger-diameter NWs. Indeed, since the Gibbs-Thomson effect, the growth rate  $V$  is expressed as:

$$V = V_0 \exp\left(-\frac{\pi\Omega\eta^2}{3kT h \Delta\mu}\right) \quad (5)$$

being  $\Delta\mu$  the difference between the chemical potential of Si in the vapor phase and in the 1D crystal, while  $\Omega$  is the atomic volume of Si,  $\eta$  is the island edge energy,  $K$  is the Boltzmann constant,  $T$  the temperature and  $h$  is the layer thickness.  $\Delta\mu$  is related to the diameter of the wire by the relation [Wang08]:

$$\Delta\mu = \Delta\mu_0 - \frac{4\alpha\Omega}{d} \quad (6)$$

where  $\Delta\mu_0$  corresponds to the chemical potential when  $d \rightarrow \infty$ .  $\Delta\mu$  represents the driving force for the SiNW growth. We can note that, since  $\Delta\mu$  is given by the Eq. (6),  $V$  is enhanced for larger values of  $d$ .

Nevertheless, it should be remarked that for ultra-thin SiNWs, when the growth is limited by the Gibbs-Thomson effect, diffusion phenomena become important. Hence, not only Si atoms are incorporated and precipitate in the metallic droplet [Fig. 4(a)], but Si adatoms coming from the source can also diffuse on the substrate and be incorporated in the SiNW [Fig. 4(b)]. This type of SiNWs shows typically an enlargement at the NW basis, which is called “tapering” and is due to the uncatalysed deposition of Si on the sides of the nanowires at higher  $T$  [Wang06]. It should be added that, especially at low  $T$ , Si adatoms can diffuse on the metallic particle surface [Fig. 4(c)], which is solid because of the low  $T$  condition. In this last condition the growth rate  $V'_S$  results [Cai07, Neumann72, Wang57]:

$$V'_S = 4 A'_S \nabla'_S / d \quad (7)$$

where  $\nabla'_S$  represents the surface concentration gradient of Si in the metal and  $A'_S$  is the surface diffusion coefficient.

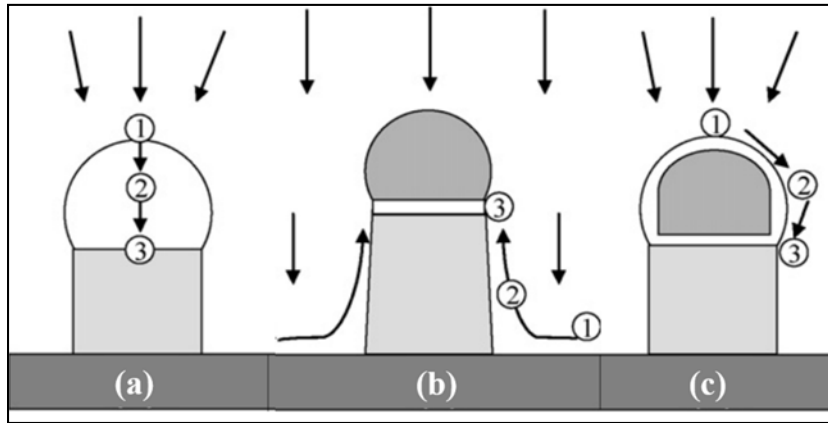
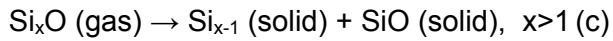
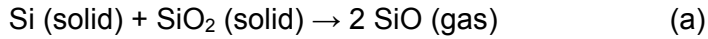


**Figure 2.4.** (a) Adsorption of Si atoms in the droplet; (b) diffusion of Si atoms on the metallic particle and incorporation of Si at the liquid-solid interface; (c) diffusion of the Si atoms on the substrate and incorporation at the SiNW flanks [Wang08].

It will be demonstrated in the fourth chapter that a small percentage of ICP-SiNWs form according to the VLS model, whereas Fe particles act as the catalyst that induced their growth.

### 2.1.b Oxide Assisted Growth mechanism

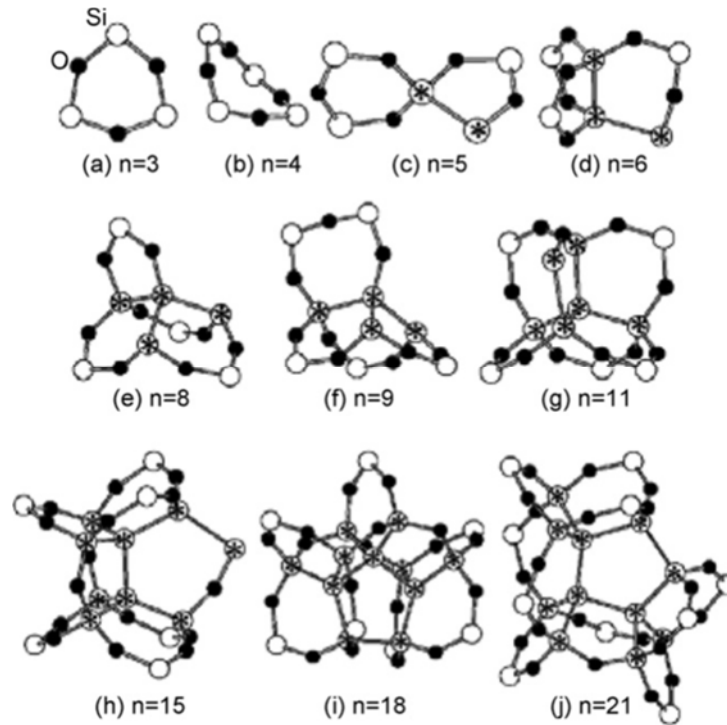
Oxide Assisted Growth mechanism was also identified as a valid alternative to synthesize SiNWs without resorting to any metal catalysts [Zhang03]. Indeed, in the OAG mechanism, instead of the metal catalyst, silicon suboxide clusters have the main role in inducing the growth of the SiNWs. These Si suboxide clusters constitute the vapor of an ablated or evaporated SiO<sub>2</sub>-containing Si target. The main reactions at the basis of the OAG are the following [Wang08]:



Reaction (a) occurs at temperatures higher than a thousands of °C, in order to achieve the complete evaporation of the SiO<sub>2</sub> containing target [Lamoreaux86]), while reactions (b) and (c) occur at lower temperatures (850°-1100°C) [Lee00, Peng01,Zhang03]. Zhang and co-workers conducted an intriguing OAG experiment in two steps to demonstrate the role of the silicon oxide, [Zhang03]: previously a SiO<sub>2</sub>-containing Si target was ablated to induce the nucleation of the SiNWs, then a Si target (without any SiO<sub>2</sub> source) was ablated to continue the growth. Nevertheless, no further growth occurred in the second step. So, unlike the VLS growth, where the growth is sustained as long as the Si vapor is supplied, no OAG occurs when only a Si target is used. Furthermore, observations report that VLS and OAG can also coexist in the same process as long as metal catalyst and SiO<sub>2</sub> are provided in the target [Peng01, Zhang03].

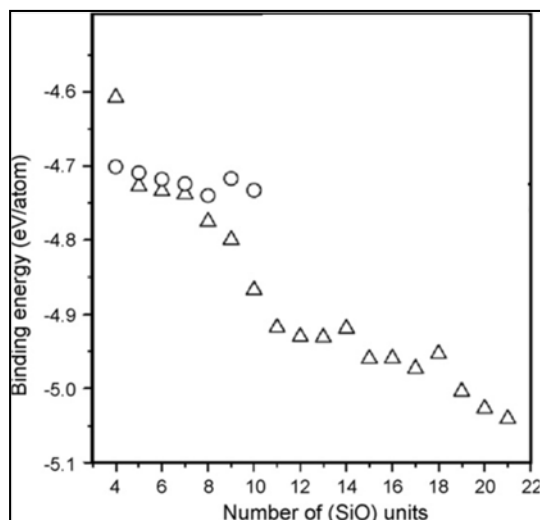
In literature, the composition of the gas phase formed by reaction (a) has been investigated theoretically [Zhang01, Zhang04]. Si suboxide clusters are highly reactive and tend to bond with other clusters preferentially forming a Si-Si bond. Nevertheless, the richest of Si is a Si-suboxide cluster, the highest is the cohesion energy per atom; hence, Si-rich Si-suboxide clusters are not favored in the gas phase. Indeed, it has been calculated that the formation of SiNWs is favored at the ratio of Si to O close to one [Zhang01]. Experimental and theoretical works revealed that silicon monoxide clusters adopt buckled-ring or planar configurations [Wang08]. An example of the earliest stages of nucleation in OAG is shown in Fig. 5. In Fig. 5(a) a SiO cluster is illustrated with a buckled-ring configuration having a number n=3 of Si atoms (and hence three O atoms). Thus, the nucleation proceeds by further aggregation of the SiO units [Fig. 5(b)]. It has been calculated that starting from n = 5 the most stable configuration contains a Si core surrounded by a silicon oxide shell, indeed the open circles containing stars in

(c) represent the Si atoms constituting the Si core. In Fig. 5 it is also easily demonstrated that the formation of an inner Si core involves Si atoms with three and four coordinates as  $n$  increases, leading to a more stable cluster.



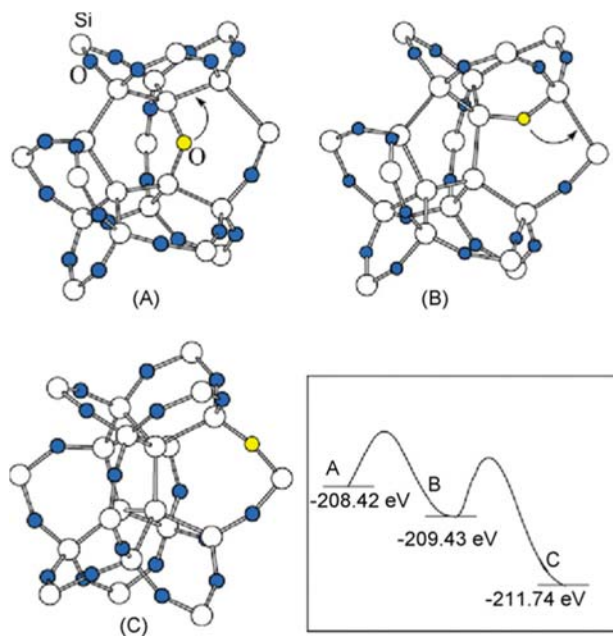
**Figure 2.5.** Early stages of SiO-like clusters aggregation, which evolves from the buckled-ring configuration (a and b) to the formation of a Si core surrounded by a silicon oxide shell (c-j). The open circles containing stars in (c) represent the Si core surrounded by a silicon oxide shell. The crystalline arrangement is most favored after  $n=18$  (i) [Wang08].

Indeed, at  $n = 18$  [Fig. 5(f)] all of the Si atoms belonging to the Si cores are four-coordinated in the  $sp^3$  configuration of crystalline Si. In the graph reported in Fig. 6 it is depicted the most favorable structure in which the Si-suboxide clusters aggregate, while the number  $n$  of SiO units increases [Wang08]: the circles represent the buckled-ring configuration while the triangles represent the Si-Si oxide core-shell structure. It can be seen that the buckled-ring configuration becomes less favorable at  $n=5$ , while the core-shell structure is the most stable configuration at higher number of SiO units.



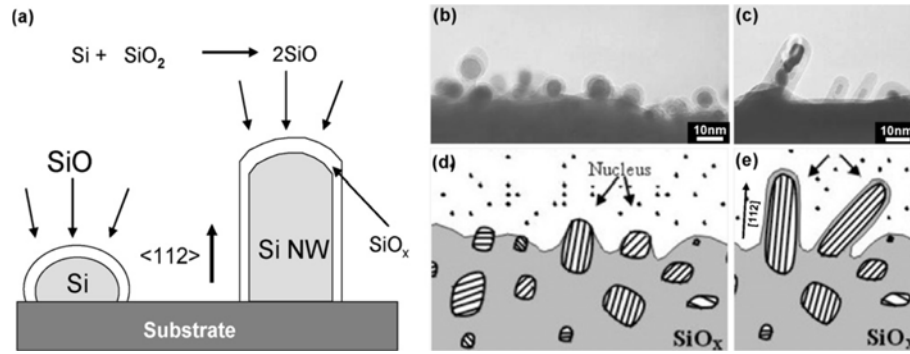
**Figure 2.6.** Binding energy (eV/atom) of  $(\text{SiO})_n$  clusters vs. the number  $n$  of SiO units. The triangles are  $(\text{SiO})_n$  with the Si-core structure surrounded by a silicon oxide sheath and open circles are those with buckled-ring structure [Wang08].

Figure 7 illustrates the isomers of the SiO clusters with the O atom in different locations, from the center [Fig. 7(a)] to the surface [Fig. 7(c)] as well as the corresponding binding energy [Wang08]. It can be noted that the configuration with the O at the surface corresponds to the most stable configuration. This is in agreement with the observation that OAG-SiNWs possess a core-shell Si-silicon oxide configuration. O atoms could simply diffuse from the center to the surface via bond switching [Fig. 7(b)].



**Figure 2.7.** Isomers of the SiO clusters with the O atom (in yellow) in different locations: (a) at the center of the cluster, (b) at intermediate position, (c) at the cluster surface. The associated binding energies for each configuration is also displayed [Wang08].

This results in the formation of an outer silicon oxide shell during the Si-suboxide cluster aggregation, i.e. the nucleation of the SiNWs. Let us notice that for SiNW nucleation, the temperature should be lower than the initial temperature needed for the formation of the Si-suboxide cluster based vapor, as also remarked in the reactions (b and c). Hence, the temperature gradient represents the external driving force for OAG-SiNW formation. Generally, the OAG mechanism has been reported for synthesis temperatures between 850°-1100°C [Lee00, Peng01, Zhang03].



**Figure 2.8.** (a) Sketch of the OAG mechanism. (b) TEM image of Si nanoparticles precipitate from the decomposition of SiO matrix. (c) The nanoparticles in a preferred orientation grow fast and form nanowires. (d, e) OAG model for the nucleation and early stages of the growth of SiNWs [Lee00].

Once the mechanism of Si-suboxide cluster aggregation has been elucidated, the growth of SiNWs via OAG mechanism can be described as follows [see Fig. 8(a)]. A SiO<sub>2</sub>-containing Si target is used to produce a vapor constituted of Si and O, which is most likely composed of Si-suboxide clusters that tend to form preferentially bonds with Si. Thus, a Si-suboxide cluster can form a Si-Si bond with a silicon based substrate [Fig. 8(b and d)], becoming thereby a nucleation site for the subsequent growth of nanowires [Fig. 8(c and e)]. Such a nucleated Si-suboxide cluster is fed by the adsorption of additional reactive Si suboxide clusters from the vapor, through the formation of Si-Si bonds. On the other hand, the oxygen atoms in these piled silicon suboxide clusters are laterally expelled by the silicon atoms to the edges where they form a chemically inert SiO<sub>2</sub> shell. Such a SiO<sub>2</sub> sheath around the SiNW prevents its lateral growth and leaves the only possibility of the perpendicular growth of the Si nanowires [Zhang03]. Remarkably, among the advantages of the OAG based growth, SiNWs were produced with diameters much thinner (i.e. minimum diameter 1.3 nm [Ma03]) than the VLS grown ones (minimum diameter 3 nm [Wu04]). Moreover, the diameter of OAG SiNWs is almost uniform because it is controlled by the self-decomposition of SiO [Wang08].

## 2.2. Conventional techniques for SiNW synthesis

The development of techniques for the synthesis of Si nanostructures aims to achieve a high level of control of the morphological properties and high yield, by suitable design of specific apparatus and methods. Although different techniques have been employed so far, basically it is

possible to classify them into two main paradigms: bottom-up and top-down approaches. While the top-down methodology is intended to create the desired nanostructure starting from the bulk material, bottom-up approach conceives the single atoms or molecules as building-blocks to assemble in order to realize suitable nanomaterials. Conventional manufacturing processes in Si-based microelectronics have been led by the top-down paradigms, which basically rely on lithography and etching procedures [Schmidt09]. From the other hand, bottom-up routes have been established as good strategies to fabricate ultra-small structures according to the ongoing trend in the scaling down of devices' dimensions.

As far as SiNWs are concerned, both top-down and bottom-up synthesis routes have been exploited. Bottom-up methods include chemical-physical approaches, like Chemical Vapor Deposition (CVD) [Hofmann03, Yao05], Molecular Beam Epitaxy (MBE) [Schubert04], laser ablation [Morales98, WangPRB98, WangCPL98, Zhang98] and thermal evaporation [WangPRB98, Wang99]. All these methods will be treated in more detail in this section. CVD and MBE basically rely on a three-phase mechanism, which exploits the presence of a metal acting as a catalyst in the process, according to the VLS process. On the other hand, during laser ablation and thermal evaporation both a metal-catalyzed and a metal-free process can occur, being the former induced by VLS and the latter by the OAG mechanism [Schmidt09, Schmidt10]. A schematic of the most common bottom-up techniques usually employed to produce SiNWs is shown in Fig. 9.

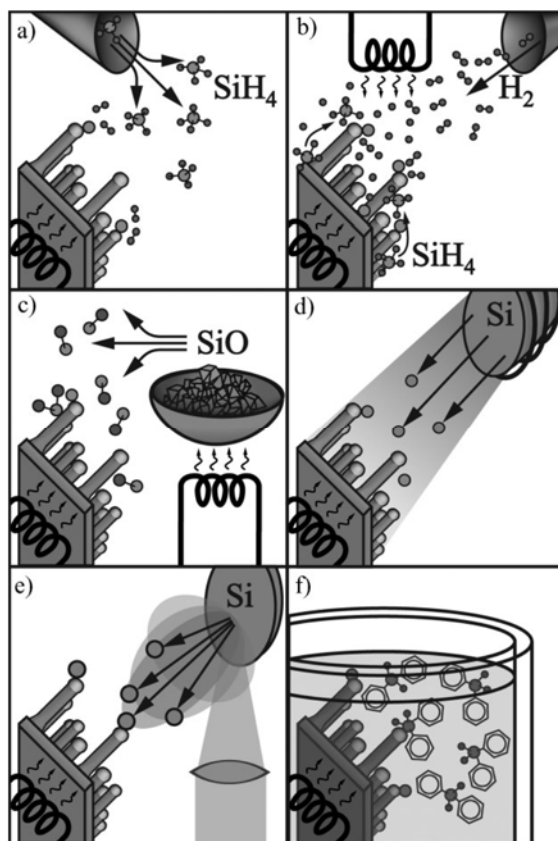


**Figure 2.9.** Schematic of the bottom-up techniques used for the synthesis of SiNWs: (a) Chemical Vapor Deposition, (b) Annealing in reactive atmosphere, (c) Thermal Evaporation of SiO, (d) Molecular Beam Epitaxy, (e) Laser Ablation, (f) Synthesis in solution [Schmidt09].

### 2.2.a Chemical Vapor Deposition

Chemical Vapor Deposition is usually performed in a tubular hot wall reactor, connected to an externally heated quartz tube where an inert gas, such as a hydrogen gas or a hydrogen/inert gas mixture, flows as a carrier gas [Schmidt09, Schmidt10]. Indeed, along the tube it is located a bubbler filled with a Si-based vapor precursor, which supplies the Si at usual flows rate of about 1500 sccm [Wang08]. Typical precursors are SiH<sub>4</sub> (silane), Si<sub>2</sub>H<sub>6</sub> disilane, SiH<sub>2</sub>Cl<sub>2</sub> (dichlorosilane) and SiCl<sub>4</sub> (tetrachlorosilane) [Schmidt10].

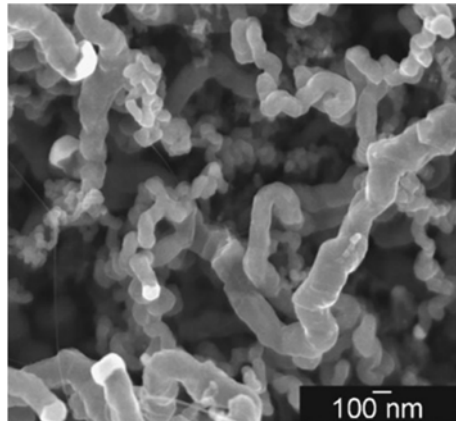


**Figure 2.10.** Typical Scanning Electron Microscopy (SEM) image of SiNWs synthesized via CVD [Hofmann03].

A Si substrate is located in the reactor and, as long as metallic particles are deposited on the substrate, SiNW growth occurs through the four different steps described by the VLS mechanism, i.e. by (i) breaking of the vapor molecules at the catalyst surface, (ii) Si atom incorporation in the catalyst, (iii) Si precipitation in the form of a crystalline anisotropic structure, and (iv) layer by layer growth below the catalytic particle. Metal particles are formed on the Si substrate because of a temperature-induced dewetting mechanism [Wang08]. More precisely, a metal thin film, deposited on the substrate via sputtering or thermal evaporation, is subject to an annealing treatment (typically at  $T \sim 500^\circ$  for Au thin films), which induces the rolling up of the film into small particles to minimize the surface energy. Thicker films dewet in larger nanoparticles. Film deposition via thermal evaporation as well as annealing-induced dewetting can be performed in-situ in the CVD chamber prior to SiNW growth [Wang06]. Metal nanoparticles can be also formed by lithography pattern, followed by annealing. Whatever procedure to obtain nanoparticles on the substrate is adopted, it is important that the particle totally wets the surface, otherwise the crystalline SiNW does not have orientation relationship with the substrate and grow randomly on it [Wang08]. Typical SiNWs grown by CVD are reported in Fig. 10. In literature, wire diameters from a few nanometers up to several micrometers have been reported [Schmidt10], whereas the minimum diameter for SiNWs grown via CVD process was observed to be  $\sim 3$  nm [Wu04]. Being this diameter dictated to some extent by the metal catalyst, it seems to be the lowest limit achievable for SiNW obtained via CVD.

## 2.2.b Molecular Beam Epitaxy

Similarly to CVD, MBE relies on the VLS mechanism [Schmidt09, Schmidt10]. The main difference is due to the fact that Si supply does not derive from the decomposition of a Si-based compound in the vapor phase, but Si vapors are provided by Si effusion cells. Therefore, Si atoms impinge on the substrate surface, being preferentially incorporated in the metallic droplets, which have been deposited on the Si substrate in a preparatory step as described above for CVD technique. In literature, an extensive debate has been stimulated on the role of the metallic droplet, being its catalytic role not required in presence of an atomic source which does not need to be decomposed [Schmidt10].

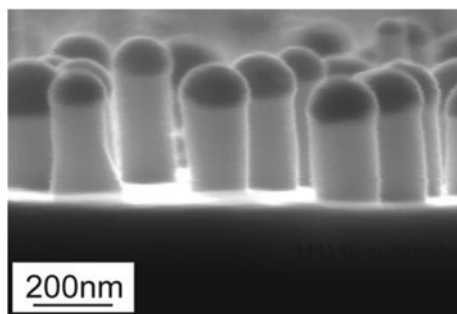


**Figure 2.11.** Typical SEM image of MBE-grown SiNWs [Schubert04].

As a matter of fact, the NW epitaxial growth is 2 orders of magnitude faster in correspondence of the metal particles than above the uncovered substrate because the metal has merely the role to favor the Si crystallization and lower the chemical potential of the source atoms [Schmidt10]. Moreover, typically the substrate is heated at temperatures of 500°C-700°C. In these conditions, the Si atoms impinging on the substrate are favored to diffuse towards the metallic nanoparticles, so not only the flux of Si atoms coming from the effusion cell, but also the flux of Si adatoms diffusing on the surface control the SiNW growth [Schmidt09]. Another feature of MBE technique is that it is an UHV-based process (pressure of the order of  $10^{-10}$  mbar), therefore the products synthesized by MBE show high purity in terms of contaminants and oxidation. Nonetheless, the growth rate is quite low for MBE, being of the order of 1-10 nm/min. As a consequence, due to the Gibbs-Thomson effect, larger diameter SiNWs are favored to form, as it can be inferred from the Fig. 11. Indeed, typical diameters larger than 40 nm have been observed [Schmidt09]. Another reason which explains the occurrence of large SiNWs concerns the fact that Ostwald ripening of metallic droplets can occur at the substrate, thus

influencing the SiNW diameter by increasing the metallic particle dimensions [Schmidt10]. A part from the slow growth rate, the limited aspect ratio of the SiNWs is affected also by the growth of the substrate induced by those Si atoms that are not able to diffuse toward the nanowires during the growth, but crystallize on the substrate surface [Schmidt10]. Among the advantages of MBE it should be mentioned the high-purity of MBE-grown SiNWs and the possibility to dope NWs in a controlled manner during the growth [Schmidt09].

### 2.2.c Laser ablation

Like MBE, laser ablation is a physical method which employs a high-power pulsed laser, such as Nd:YAG or KrF excimer laser, to ablate a target [Wang08]. Since the target contains the metal catalyst, the catalyst is coablated with the Si, inducing the Si vaporization as well as metal/metal silicide nanoparticles production in the vapor. Once the Si vapor is dissolved into the nanoparticle, SiNW growth can occur during the vaporization, according to the VLS mechanism. VLS-grown SiNWs by means of laser ablation have as typical feature the catalytic particle at their tip, as it can be seen in Fig. 12(a) [Wang08]. The presence of the substrate is not mandatory for laser ablation because the SiNWs can also deposit on the wall of the reaction chamber [Wang08].

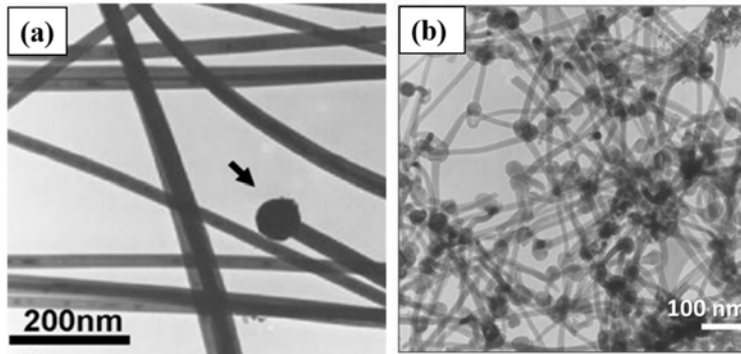


**Figure 2.12.** (a) SiNWs grown by means of laser ablation via the VLS mechanism, as indicated by the presence of particles at the top of the wires, as marked by the arrow [Wang08]. (b) SiNWs produced in bulk quantity via laser ablation technique [Morales98].

Since the temperatures reached at the target are extremely high, also high-temperature eutectic alloys can be exploited as catalysts for SiNW growth. As an example, Fe has been used for laser ablation VLS-based synthesis [Morales98]. Hence, laser ablation allows high versatility in

the choice of the materials, including the ones with higher eutectic temperature, and also doped SiNWs can be realized [Schmidt10].

Furthermore, by mixing SiO<sub>2</sub> and Si in the target, an OAG growth driven SiNW synthesis has also been demonstrated via laser ablation [Zhang03]. These nanostructures exhibit an elevated aspect-ratio thanks also to the high growth rates, which has been reported to range from 0.1-1 μm/min up to several μm/min [Schmidt09]. The growth rate depends on different parameters, such as the power of the laser, the vacuum conditions, the gas employed and the temperature [Wang08]. Finally, it is worthy to mention that laser ablation process is conducted inside a furnace as reaction chamber, filled with an inert gas, such as Ar, He, H<sub>2</sub>, or N<sub>2</sub>. It has been observed that different choice of the gas influences the final diameter of the SiNWs and thus their optoelectronic properties [Zhang99].

In general, bulk quantity production [Morales98, Zhang98] has been achieved via laser ablation [see Fig. 12(b)], which is one of the main advantages of the exploitation of laser ablation together with the above-mentioned great versatility of this technique. The condition of high temperature generated by the plasma makes laser ablation very similar to the ICP technique used in the present work. Hence, the knowledge of laser ablation is an important requirement for the understanding of SiNWs synthesis via ICP. We will see in the following part that also thermal evaporation possesses similar characteristics to the ICP process.

#### **2.2.d Thermal evaporation**

Thermal evaporation is accomplished in a tube furnace connected with an inert gas supply. The experimental conditions are chosen in such a way that a temperature gradient exists, allowing the inert gas to flow from the hotter to the colder part of the tubular furnace [Wang08]. The source is located in the hot zone of the furnace, so that it evaporates and the vapor is carried by the inert gas towards the colder region of the tube, where both a VLS reaction (in case the source contains some metallic components) and a disproportionation reaction (in case the source has a SiO-based composition) can occur [Wang08]. In the first case, VLS-based mechanism drives the growth of the SiNWs, while in the other case the OAG mechanism is at the basis of the growth of the SiNW, like the ones shown in Fig. 13. Typical growth parameters are pressures of the order of 100 Torr, flow rates of inert gas or inert gas/hydrogen mixture of ~50 sccm, temperatures in the range of 1100-1350 °C for the hot part of the reactor and temperatures of 900-1000°C for the colder part of the reactor where Si nanowire growth.

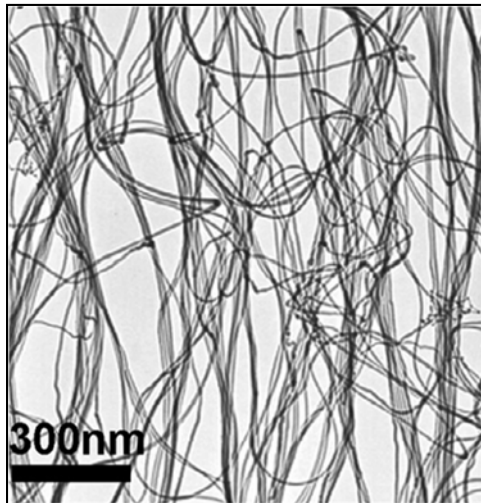


**Figure 2.13.** Typical SEM image of SiNWs grown via thermal evaporation [Zhang03].

Thermal evaporation has the important advantage to enable the production of bulk-quantity of SiNWs [Zhang00] with ultra-thin diameter up to  $\sim 1.3$  nm [Ma03]. From the other hand, the main drawback [Schmidt10] is the lack of controllability in terms of SiNW diameters and lengths. Also, a controlled doping of the nanowires is difficult. As mentioned above, thermal evaporation technique has similar features to the ICP process: indeed, like in thermal evaporation, ICP technique requires the evaporation of the target as a fundamental step, which is accomplished by means of high-temperature plasma.

## 2.3. Conclusions

An overview of the in-lab techniques currently employed for SiNW synthesis has been presented in this chapter, as well as the physical and chemical mechanisms at the basis of SiNW formation. These mechanisms can be essentially based on the catalytic action of a metal particle in a three phase mechanism [Wacaser09] or on the OAG mechanism [Zhao03], where the main role is performed by Si suboxide clusters. The techniques illustrated here basically rely on the bottom-up approach, which has been demonstrated to be more suitable than top-down methods for the synthesis of ultra-thin SiNWs.

Nevertheless, it deserves to be noted that the growth of these ultra-thin structures is challenging, in particular when the SiNW growth occurs via the VLS mechanism, for which the minimum diameter is dictated by the minimum size of the metallic particle. A further issue

concerns the yield of SiNW that is provided by the well-established synthesis techniques described above, for which a bulk production is highly desirable.

In this panorama, Inductively Coupled Plasma (ICP) technique, which will be described in the next chapter, appears as a promising technique for the high throughput production of SiNWs.

## Bibliography

[Bootsma71] G. A. Bootsma and H. J. Gassen, *J. Cryst. Growth* 10, 223 (1971).

[Cai07] Y. Cai, Characterization of ultrathin II–VI semiconductor nanowires by transmission electron microscopy, PhD Dissertation, Physics Department, the HongKong University of Science and Technology, HongKong, September 2007.

[Davidson07] F. M. Davidson, D. C. Lee, D. D. Fanfair and B. A. Korgel, *J. Phys. Chem. C* 111 (2007).

[Givargizov75] E. I. Givargizov, *J. Cryst. Growth* 31 (1975).

[Hofmann03] S. Hofmann, C. Ducati, R. J. Neill, S. Piscanec, A. C. Ferrari, J. Geng, R. E. Dunin-Borkowski and J. Robertson, *J. Appl. Phys.* 94, 9 (2003).

[Lamoreaux86] R. H. Lamoreaux, D. L. Hildenbrand and L. Brewer, *J. Phys. Chem. Ref. data* 16, 3 (1987).

[Lee00] S. T. Lee, N. Wang and C. S. Lee, *Mater. Sci. Eng. A* 286, 1 (2000).

[Ma03] D. D. D. Ma, C. S. Lee, F. C. K. Au, S. Y. Tong and S. T. Lee, *Science* 299, 5614 (2003).

[Morales98] A. M. Morales and C. M. Lieber, *Science* 279, 5348 (1998).

[Neumann72] G. Neumann, G.M. Neumann, *Surface Self-diffusion of Metals*, Diffusion Monograph Series, vol. 1, Diffusion Information Center, 1972, p.105.

[PDDatabase] <http://steel.kisti.re.kr/html/Fe-Si.htm>.

[Peng01] H. Y. Peng, Z. W. Pan, L. Xu, X. H. Fan, N. Wang, C. S. Lee and S. T. Lee, *Adv. Mater.* 13, 5 (2001).

[Rowlinson03] J.S. Rowlinson, B. Windom, *Molecular Theory of Capillarity*, Dover, 2003.

[Schmidt09] V. Schmidt, J. V. Wittemann, S. Senz and U. Gösele, *Adv. Mater.* 21, 25-26 (2009).

[Schmidt10] V. Schmidt, J. V. Wittemann and U. Gösele, *Chem. Rev.* 110, 1 (2010).

- [Schubert04] L. Schubert, P. Werner, N. D. Zakharov, G. Gerth, F. M. Kolb, L. Long, U. Gösele and T. Y. Tan, *Appl. Phys. Lett.* 84, 24 (2004).
- [Treuting57] R. G. Treuting and S. M. Arnold, *Acta Met.* 5, 598 (1957).
- [Tuan05] H. Y. Tuan, D. C. Lee, T. Hanrath, B. A. Korgel, *Nano Lett.* 5, 681 (2005).
- [Wacaser09] B. A. Wacaser, K. A. Dick, J. Johansson, M. T. Borgström, K. Deppert and L. Samuelson, *Adv. Mater.* 21, 2 (2009).
- [Wagner64] R. S. Wagner and W. C. Ellis, *Appl. Phys. Lett.* 4, 5 (1964).
- [Wang57] H. Wang, G.S. Fischman, *J. Appl. Phys.* 76 (1994) 1557.
- [WangPRB98] N.Wang, Y. H. Tang, Y. F. Zhang, C. S. Lee and S. T. Lee, *Phys. Rev. B* 58, 24 (1998).
- [WangCPL98] N. Wang, Y. H. Tang, Y. F. Zhang, D. P. Yu, C. S. Lee, I. Bello and S. T. Lee, *Chem. Phys. Lett.* 283, 5 (1998).
- [Wang99] N. Wang, N., Y. H. Tang, Y. F. Zhang, C. S. Lee, I. Bello and S. T. Lee, *Chem. Phys. Lett.* 299, 2 (1999).
- [Wang06] Y. Wang, V. Schmidt, S. Senz, U. Gösele, *Nat. Nanotechnol.* 1, 186 (2006).
- [Wang08] N. Wang, Y. Cai, and R. Q. Zhang, *Mater. Sci. Eng. R-60*, 1 (2008).
- [Widom95] B. Widom, *J. Phys. Chem.* 99, (1995).
- [Wu04] Y. Wu, Y. Cui, L. Huynh, C. J. Barrelet, D. C. Bell and C. M. Lieber, *Nano Lett.* 4, 3 (2004).
- [Yao05] Y. Yao, F. Li and S. T. Lee, *Chem. Phys. Lett.* 406, 4 (2005).
- [Yu01] D. P. Yu, Y. J. Xing, Q. L. Hang, H. F. Yan, J. Xu, Z. H. Xi and S. Q. Feng, *Phys. E* 9, 305 (2001).
- [Zhang98] Y. F. Zhang, Y. H. Tang, N. Wang, D. P. Yu, C. S. Lee, I. Bello and S. T. Lee, *Appl. Phys. Lett.* 72, 15 (1998).
- [Zhang99] Y. F. Zhang, Y. H. Tang, H. Y. Peng, N. Wang, C. S. Lee, I. Bello, and S. T. Lee, *Appl. Phys. Lett.* 75, 1842 (1999).
- [Zhang00] Y.F. Zhang, Y.H. Tang, C. Lam, N. Wang, C.S. Lee, I. Bello, S.T. Lee, *J. Cryst. Growth* 212, 1 (2000).

[Zhang01] R.Q. Zhang, T.S. Chu, H.F. Cheung, N.Wang, S.T. Lee, Phys. Rev. B 64, 11 (2001).

[Zhang03] R-Q. Zhang, Y. Lifshitz and S-T. Lee, Adv. Mater. 15, 7-8 (2003).

[Zhang04] R.Q. Zhang, M.W. Zhao, S.T. Lee, Phys. Rev. Lett. 93, 9 (2004).

## **CHAPTER 3: EXPERIMENTAL DETAILS**

In this chapter the details of the industrial process employed for the SiNW synthesis and the techniques exploited for their characterization will be introduced. The former consists in the use of an Inductively Coupled Plasma (ICP) based system, while the latter include Transmission Electron Microscopy (TEM) based techniques and Photoluminescence (PL) spectroscopy. It is noteworthy that the ICP-based apparatus is commonly used for the synthesis of Si micropowders, of which the SiNWs studied here represents the by-product. Once understood the physical mechanisms that induces the growth of these ICP-SiNWs, their synthesis has been then pursued intentionally by designing a more suitable procedure and exploiting a more appropriate ICP-based apparatus (which is usually employed for the synthesis of nanopowders).

TEM played a primary role in the study of ICP-SiNWs, gathering all the information about the most characteristic structural features of ICP-SiNWs. Both imaging and spectroscopy TEM-based techniques as well as electron tomography have been employed to achieve the most accurate characterization of the ICP-SiNWs at the nanometric scale from a structural and a chemical point of view. Hence, once the TEM confirmed the nanosize of these ICP-structures, PL spectroscopy has been used to probe the occurrence of light emission.

In the first paragraph of the chapter, first of all, the basics of ICP mechanism will be explained, then the apparatus used for the synthesis of micro and nanopowders will be described. The second paragraph is dedicated to TEM, starting from preliminary concepts and from the description of the instrument. The TEM based techniques employed in this thesis are then focused in more detail; these consist in the Energy Filtered TEM (EFTEM), electron tomography, Scanning TEM-Energy Dispersive X-ray spectroscopy (STEM-EDX), STEM-Electron Energy Loss Spectroscopy (STEM-EELS) and cathodoluminescence (CL). The experimental setups used for the PL measurements will be finally illustrated in the last paragraph of this chapter.

### **3.1. Inductively Coupled Plasma for large scale production**

Plasma is classified as the fourth state of matter. It is a partially ionized gas which contains positive and negative ions, electrons, atoms and neutral species, so that the overall

plasma results to be neutral. Two main types of plasmas can be distinguished, according to their densities and the temperature of the electrons with respect to the other components of the plasma, i.e. cold plasma and thermal plasma [Guo10]. In cold plasma the temperature  $T$  of electrons can be very high ( $T > 10,000$  K) while the temperature of heavy particles (ions, atoms, molecules) is near room temperature. Cold plasma is far from the thermal equilibrium condition and its overall temperature is close to the room temperature. The cold plasma is generated under vacuum conditions typically by fluorescent lamps or glow discharges. On the other hand, in thermal plasma the temperature of heavy particles in the plasma is close to that of electrons and it is in a partially local thermodynamic equilibrium state. The temperature of thermal plasma is typically around 10,000 K or higher. Typical examples of thermal plasma include direct current arc discharge and high frequency inductive discharge [Guo10].

Inductively coupled plasma is generated by means of an inductive coupling mechanism. Basically, an alternative RF current ( $\sim 0.1$ -1 MHz) flowing through a spiral coil at high voltage (10-100 kV) produces an electromagnetic field within the coil, heating up a conductive gas in a tube enclosed by the spires and ionizing it into a plasma [Guo10]. A schematic of the system is reported in Fig. 1(a). Among the advantages of ICP, we can cite:

- (i) The clean nature of the plasma source,
- (ii) Any gas can be used as a plasma source (like  $H_2$ ,  $N_2$ ,  $O_2$ , Ar,  $NH_3$ ,  $CH_4$  and other gas mixtures) in such a way that plasma can be either inert or chemically reactive,
- (iii) the relatively high volume of the plasma region as well as the low velocity of the plasma gas make ICP suitable for the treatment of any kind of material, including high-melting point materials.

Enthalpy and thermal conductivity of the gases are the key parameters determining the thermodynamics and the transport properties of the plasma and thus the overall efficiency of the process [Guo10]. The ICP reactors used for the synthesis of the samples studied in this project have been routinely used by Tekna Plasma Systems Inc. for the successful spheroidization and/or purification of different types of micropowders, at the industrial production levels [www.tekna.com]. In the following, the ICP based spheroidization process used by Tekna to produce micropowders [Guo95] and nanopowders [Guo10] of silicon will be briefly described.

### 3.1.a Micropowder synthesis

An ICP based spheroidization process is usually used by Tekna for the transformation of rough and angular silicon powders [Fig. 1(b)] into high-quality, pure and regular silicon microspheres, of which diameters are equal to about a hundred of nm [Fig. 1(c)] [Guo95]. Concomitant to this Si spheroidization process, Si nanopowder was also found as a by-product. In this process, the pure Si powder feedstock (average particle size of 115  $\mu\text{m}$  and 99.5% purity) is introduced in the Ar/H<sub>2</sub> plasma torch tube [Fig. 1(d)] with Ar as carrier gas. Most of the feedstock powder is melted in-flight and minimizes its surface energy by forming Si spheres of equivalent mean diameter that are collected in the first collector of the ICP reactor [called "Cyclone Bottom (CB)" in Fig. 1(d)].

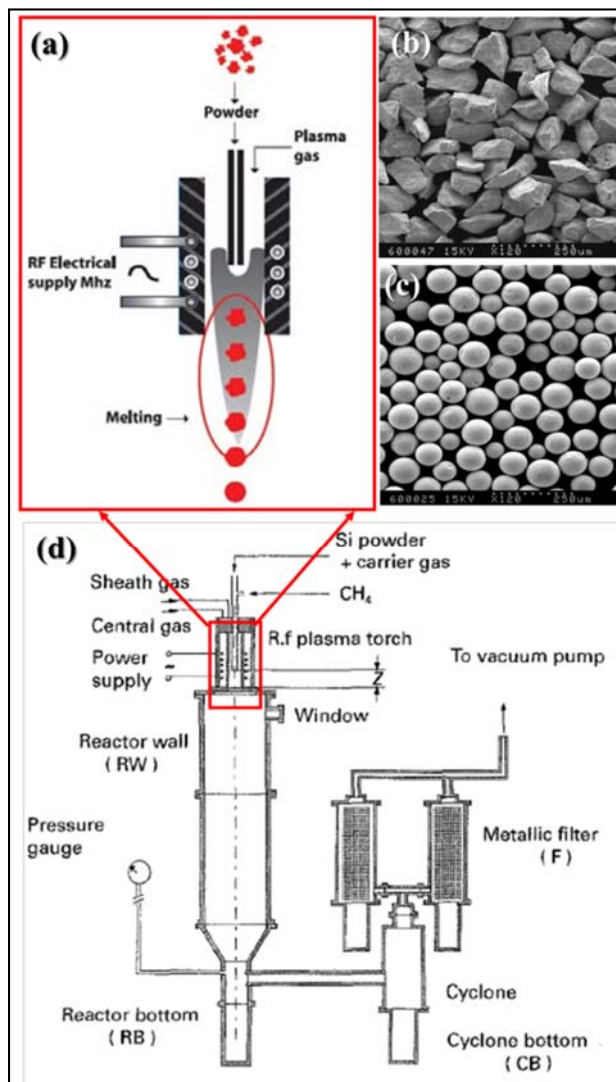


**Figure 3.1.** Illustration of the spheroidization system for spherical micropowder synthesis: a Si rough powder (a) is inserted in the plasma tube (c) as a feedstock for the production of high-quality spherical micropowders (b). The reactor for micropowder synthesis is sketched in (d). [www.tekna.com]

Concomitant to the in-flight melting of the Si particles in the hot zone of the ICP torch [red rectangle in Fig. 1(d)], a fraction of the Si powder sublimates and the resulting Si vapor condenses in the lower temperature zone of the reactor, leading to the formation of lighter Si nanostructures. These latter are carried downstream with the gases and are retained in the second collector [metallic filter F in Fig. 1(d)], where a significant amount of Si nanopowders is collected. These Si-nanopowders are our material under investigation and will be referred to hereafter with the name of “as-collected” powder.

### 3.1.b Si Nanopowder synthesis

Diverse types of nanomaterials have been synthesized via ICP Tekna systems, spanning from ceramics to metallic nanopowders [Guo10]. Nanopowder synthesis by means of ICP systems can be divided in the following steps: injection of the feedstock, evaporation in the plasma zone, quenching and powder collection. Power, nature and density of the feedstock, gas flow rates and quenching conditions are among the crucial parameters in nanopowder ICP-synthesis for the control of crystallinity and nanoparticle size. Numerical modeling has been employed for the design of the most suitable process for the desired nanopowder synthesis [Guo10]. The simulations concern the temperatures, gas flows and concentrations in the plasma systems and allow obtaining precious information about the plasma process. Figure 2 illustrates an example of numerical modeling of (a) the temperature distribution inside the plasma chamber, (b) the rate of temperature variation and (c) the distribution of the gaseous cold front having a quenching action (where the temperature field is: red=10.000 K and blue=350 K). The vapors or molecular clusters form in the high-temperature zone of plasma or close to it [red area of Fig. 2(a)]. Hence, the vapor crosses a quench section where gases injected through transpirational holes cool them down to nanoparticles, the cold gas distribution being represented by Fig. 2(c). As a result, the temperature changes abruptly from the plasma tube to the quenching zone [Fig. 2(b)]. It has been demonstrated that, with a gas flow fixed at 300 slpm, the temperature inside the reactor can be reduced from ~10.000 K to about room temperatures, thus leading to an effective quenching of the nanoparticles. [Guo10].

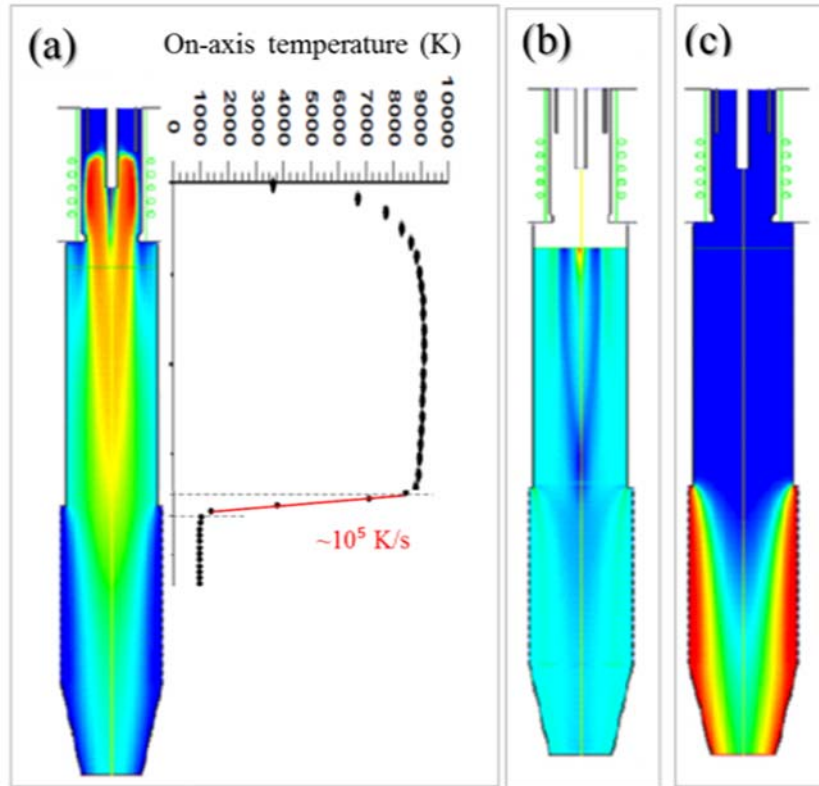


**Figure 3.2.** Numerical modeling regarding (a) the temperature distribution inside the plasma chamber, (b) the rate of temperature variation and (c) the distribution of the gaseous cold front having a quenching action [Guo10]. Temperature field (Red=10.000 K and Blue=350 K).

For the direct synthesis of SiNWs studied in the second step of this project, Tekna has recently optimized an ICP process for the reproducible synthesis of SiNWs. However, the specific process parameters used for the direct synthesis of SiNWs are still confidential and cannot be disclosed for the moment (patent filing is under evaluation).

## 3.2. Transmission Electron Microscopy

Transmission Electron Microscopy emerges as one of the most suitable characterization techniques for the study of nanomaterials, since it allows to conjugate both spatial and analytical resolution up to the sub-nanometric range [Williams09]. Going beyond the mere imaging of fine details of the material, the TEM is very appropriate to conduct diffraction and spectroscopy of nanodomains. We recall that the possibility to perform imaging by means of an electron beam, similarly to what happens with light microscopes, is basically due to the dual nature of electrons,

which can be regarded as both particles and waves for the De Broglie's principle. The spatial resolution depends on the wavelength  $\lambda$  of the radiation, through the Rayleigh relationship

$$\delta = \frac{0.61 \lambda}{n \sin \beta} \quad (1)$$

where  $\beta$  is the semi-angle of collection of the magnifying lens and  $n$  is their refractive index. Thus, it can be evaluated that for typical electron beam energy  $\sim 100$  keV, a spatial resolution of the order of several pm can be obtained, at least in principle. However, this theoretical limit cannot be reached with real electromagnetic lenses owing to the unavoidable presence of lens aberrations. In this regard, nowadays, the development of aberration correctors in TEM has been demonstrated to be fundamental to achieve extremely high spatial resolution values, as shown in Fig.3, which reports the increasing trend obtained in the last two centuries. It can be noted that, thanks to the introduction of aberration-correctors in electron microscopy, it is possible nowadays to reach sub-Å spatial resolution.

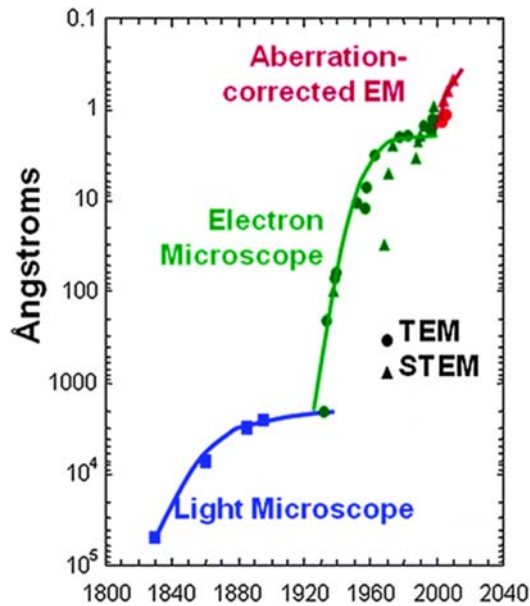


**Figure 3.3.** Trend of spatial resolution achieved in the last two centuries; thanks to the aberration-corrected TEM the sub-Å resolution is nowadays reachable. The resolution obtained via optical microscopy is also displayed for comparison [Pennycook14].

Moreover, the electron-matter interactions and the signals that this interaction generates are at the basis of the possibility to gather also analytical information with TEM analyses. A

sketch illustrating the signals generated by the electron-matter interactions is given in Fig. 4. The detection of these signals allows to perform not only spectroscopic analyses but also chemical mapping with very high spatial resolution, where the analytical information is combined with imaging.

For the sake of simplicity, a TEM can be sketched into three main parts, namely the illumination system, the objective lens/stage and the imaging system. Basically, the illumination system includes the electron gun, which generates the electron beam, and the system of condenser lens, while the imaging system is constituted of intermediate and diffraction lenses as well as projector lens [Williams09].

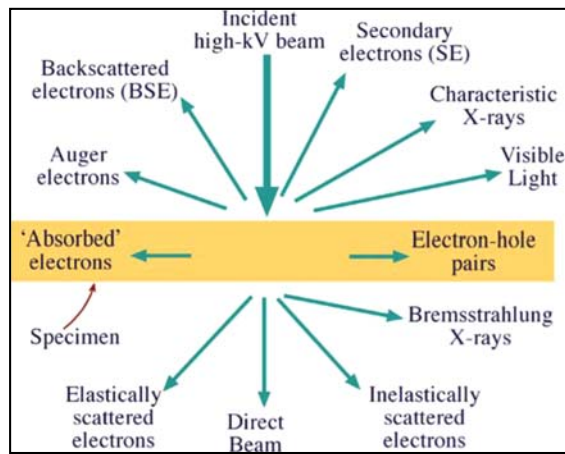


**Figure 3.4.** Signals generated by the electron-matter interaction [Williams09].

The electron beam is produced by thermoionic or field emission sources and directed into the illumination system. In particular, after being emitted by the gun, the electrons are accelerated by an electric field at a specific energy, which is defined by the operating voltage of the microscope. It is well-known that, among the different types of electron sources, field emission guns (FEGs) are more advantageous than the thermionic ones since they generate electron beams having a higher brightness as well as a better spatial and temporal coherence, providing higher spatial resolution for imaging and elevate energy resolution for spectroscopy. By comparing cold FEGs and Schottky FEGs, it emerges that cold FEG's performances are superior, even if their maintenance is more critical because the emission is less stable over time and requires ultra-high vacuum conditions to operate.

The illumination system can be used in parallel beam mode or in convergent beam mode, by scanning the convergent electron beam through the sample. The former configuration is used for TEM imaging and selected-area diffraction (SAD), while the latter is applied for STEM

imaging, STEM-EDX and convergent beam electron diffraction (CBED). As far as the acquisition modes are concerned, two basic modes are possible: the imaging mode and the diffraction mode, which allow to obtain the image of the sample or its diffraction pattern, respectively. The main feature of STEM mode relies in the fact that in this case the imaging system operates always in diffraction mode. Hence, STEM images are formed by detectors which integrate the intensity of diffraction plane over specific angles for each scan position on the sample. In STEM mode, thus, the image is not formed by means of lens and the aberrations of the lens in the imaging system do not affect the image resolution. Nonetheless, the formation of the electronic probe is crucial since it determines the final resolution, therefore the probe aberration correction is highly demanded when atomic resolution is required. The basic principle on which the probe corrector relies is linked to the action of multipoles that compensate the aberration of the beam [Houdellier14]. In aberration-corrected TEM, hexapole or octupole lenses are used in the aberration corrector. Such lenses lack rotational symmetry and thus do not have a positive spherical aberration like conventional, round magnetic lenses [Liao07]. Figure 5(a) shows a sketch of a hexapole lens for spherical aberration correction ( $C_s$ ). The optical axis, along which the electrons travel, is directed perpendicularly into the page, while the blue lines indicate the magnetic field lines and the red ones indicate the Lorentz force on the electrons. The overall effect consists in a triangular distortion of the beam, as it can be seen in Fig. 5(b). In Figure 5(c) it has been reported the effect of spherical aberration: electrons at different distances from the optical axis are focused at different points along the optical axis. The effect of the corrector is such that it compensates the aberration by squeezing that portion of the electron beam which has been focused before along the optical axis. Usually a sequence of multipoles is necessary to compensate the overall aberration.

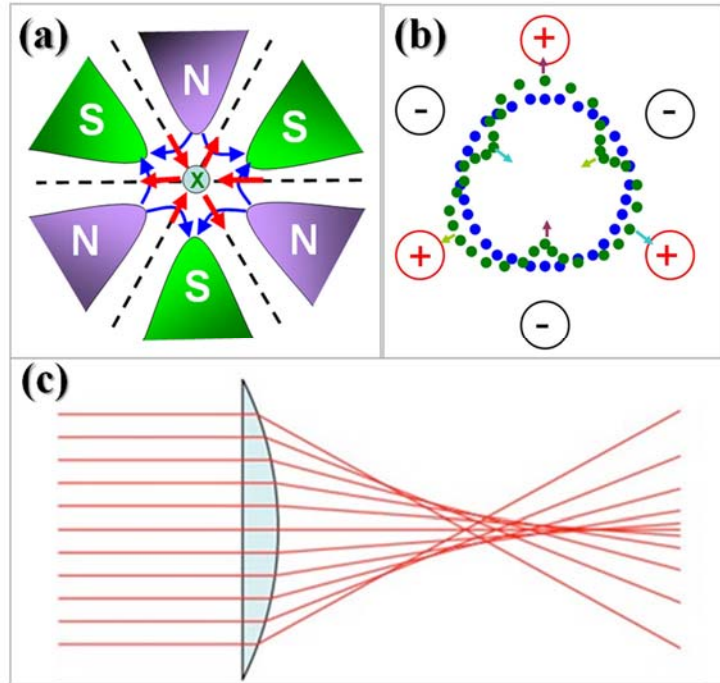


**Figure 3.5.** (a) Sketch of a hexapole magnetic lens; (b) deformation of the electron beam under the action of a hexapole; [Liao07] (c) Effect of the spherical aberration [Houdellier14].

Between the illumination system and the imaging system, the specimen is placed on the TEM sample-holder. In general, the sample stage allows both the positioning of the sample and the tilting around two axes. As it will better described below, for tomography the most important feature is the maximum tilt range available for the sample holder.

For this work, the TEM analyses have been realized in the IMM-CNR labs (Catania) which are equipped with the following state-of-the-art facilities:

- A JEOL JEM 2010F TEM with a Schottky FEG and operating at an acceleration voltage of 200 kV, with spatial resolution equal to 0.18 nm. The TEM is also equipped with a Gatan Image Filter (GIF) allowing EELS and EFTEM analyses.
- A spherical aberration probe corrected cold FEG (with an energy spread of 0.27 eV) Atomic Resolution Microscope (ARM) JEOL operating from 40 to 200 keV, equipped with both GIF and large area (100 mm<sup>2</sup>) EDX silicon drift detector (with an energy resolution of 127 eV). Here, the probe correction is operated by a Ceos hexapole Cs aberration corrector, allowing to reach a resolution of 0.68 Å at 200 keV and 1.36 Å at 40 keV.

The 2010F TEM was used to realize EFTEM and High Resolution TEM analyses on individual SiNWs. Moreover, in-situ EFTEM analyses have been performed by annealing the

sample via a smart heater control. The ARM was used to accomplish STEM-EDX analyses with sub-nanometer probe and Electron Tomography in STEM mode, by using a High Angular Annular Dark Field (HAADF) detector. In particular, Electron Tomography was conducted by using a single-tilt Fischione tomography sample holder, which can be tilted within a maximum angular range of  $\pm 60^\circ$ .

Moreover, CL experiments have been performed at the Laboratoire de Physique des Solides, Université Paris Sud (Orsay, France) by means of a VG-HB501 STEM equipped with a tungsten cold field-emission gun and a CL detector, operating at 60 and 100 kV. Finally, a Gemini Field Emission Scanning Electron Microscope (FE-SEM) Carl Zeiss SUPRA™ 25 equipped with a thermal FEG was used for large area observations of the as-collected ICP-powder. The principles of the above-mentioned TEM techniques will be treated in the following sections, by distinguishing the spectroscopic techniques (EELS, EDX, CL) as well as the imaging techniques (EFTEM) in the first section and electron tomography in the second one.

### **3.2.a Spectroscopic and imaging techniques**

As it has been mentioned above, the electron beam interacting with the sample generates a number of signals, which constitute the information available in TEM. It is possible, in fact, to detect the transmitted electron beam and analyse the amount of energy lost by the electrons while interacting with the sample (EELS), the X rays generated by the interaction between the electrons and the atoms of the sample (EDX) or the optical emission in the visible range generated by the electron-hole recombination (CL).

EELS allows the acquisition of the elastic and inelastic signals, so that two main regions can be identified in the EELS spectra: the low-loss region, extending from 0 to about 60 eV, and the high-loss region, which could extend up to some thousands of eV. Two typical low-loss spectra of the ICP-SiNWs acquired at 100 keV (red line) and at 60 keV (blue line) are reported in Fig. 6(a) and (b), respectively. The main peak (called “zero-loss”) is due to unscattered electrons, namely those electrons that are transmitted without any interaction with the medium, and to those electrons that have suffered no measurable energy loss (such as elastically scattered electrons). The second prominent feature in the EELS spectrum is the “plasmon peak”, due to the collective excitation of outer-shell electrons, which create a plasma resonance in the form of a longitudinal traveling wave [Egerton11]. These above mentioned plasmon losses are called “volume plasmons” because they arise from the collective interaction with the electrons in

the bulk of the specimen. It is possible to discern, in the low-loss spectra depicted in Fig. 6, the presence of two different electron energy plasmon losses located at 17 eV and 23 eV, i.e. the plasmon of Si and SiO<sub>2</sub> respectively. The incident electrons, however, can also originate a longitudinal wave of charge density which travels along the surface and is referred to as “surface plasmon” [as indicated by the arrows in Fig. 6 (a) and (b)]. In this thesis, STEM-EELS analyses have been performed on ICP-SiNWs at beam energy of 100 keV. The choice of this energy value allows to avoid the damage induced by the convergent beam at a higher energy value (i.e. 200 keV) and, at the same time, furnishes a good signal to noise ratio. Indeed, it can be seen in Fig. 6(b) that, when the electron energy is too low, the contribution of the plural scattering of the electrons becomes more important starting from about 40 eV and it is overlapped with the plasmon peak.

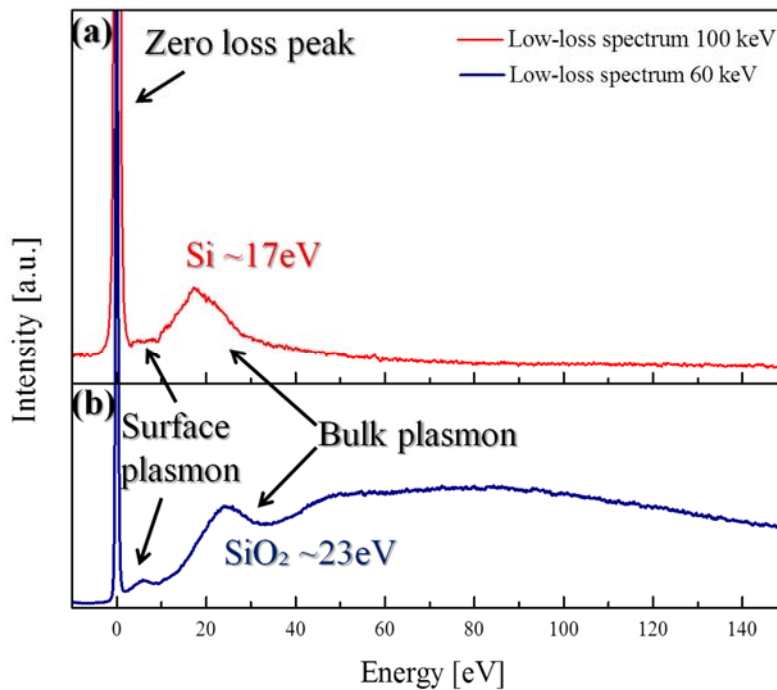


**Figure 3.6.** Low-loss EELS spectra of as collected ICP-SiNWs detected at 60 keV (blue line) and 100 keV (red line).

At higher energy loss, the intensity in the spectrum falls dramatically but, superposed on this decline, there are ionization edges, which represent the excitation of core electrons towards an unoccupied electronic state above the Fermi level. Because the edge threshold occurs at the binding energy  $E_k$  of each shell ( $k = K, L$  etc.), which is known for all elements, the chemical species responsible of the excitation can be identified. In Figure 7 it is illustrated the comparison

of the High-Loss EELS spectra produced by two different samples of ICP-SiNWs. The blue line refers to ICP-SiNWs as collected subsequently to the ICP synthesis process, while the red line represents ICP-SiNWs after being subjected to a post-synthesis thermal treatment in  $N_2$  at  $1200^\circ C$ . In Figure 7 the ionization edges of the chemical elements composing the sample have been indicated and can be discerned over the background. It can be noted the presence in both spectra, of the ionization energies of Si (edge L), carbon (C, edge K) and oxygen (O, edge K). In agreement with the low-loss, the high-loss spectra show that the ICP-SiNWs are composed of Si and O. The C belongs to the carbon lacey grid used as a support for the TEM studies of our free standing ICP-SiNWs. Nonetheless, in the high-loss spectrum of the annealed sample a further peak can be noted. This peak, which can be ascribed to nitrogen (N, edge K), reveals that a small amount of N was incorporated into the SiNWs during the annealing treatment performed in  $N_2$  ambient.

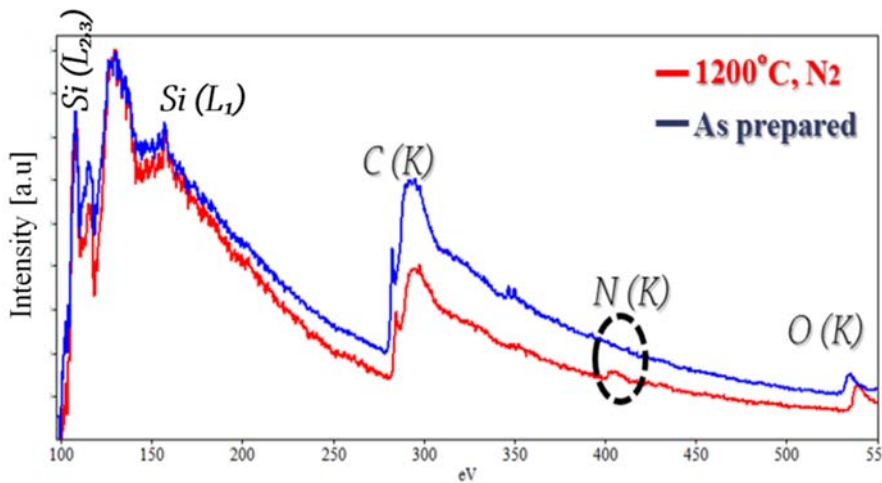


**Figure. 3.7.** High loss EELS spectra of ICP-SiNWs as-collected and annealed at  $1200^\circ C$  in  $N_2$ , showing nitrogen incorporation the SiNWs after annealing.

Spectrum Imaging (SI) technique is one of the most powerful TEM based technique since it allows the acquisition of STEM-EDX, STEM-EELS or STEM-CL spectra for each pixel of a digital image. The result of the SI process can be figured as a 3D data cube, where the electron image constitutes the x–y plane and the spectra are represented in the z direction [Williams09]. Hence, since every single pixel in the x–y (image) plane corresponds to a spectrum, it is possible to select an ensemble of pixels to have the spectrum of the corresponding region of the image. Additionally, it is possible to select a well-defined value of electron energy loss or X-ray energy to obtain a chemical map formed by these signals.

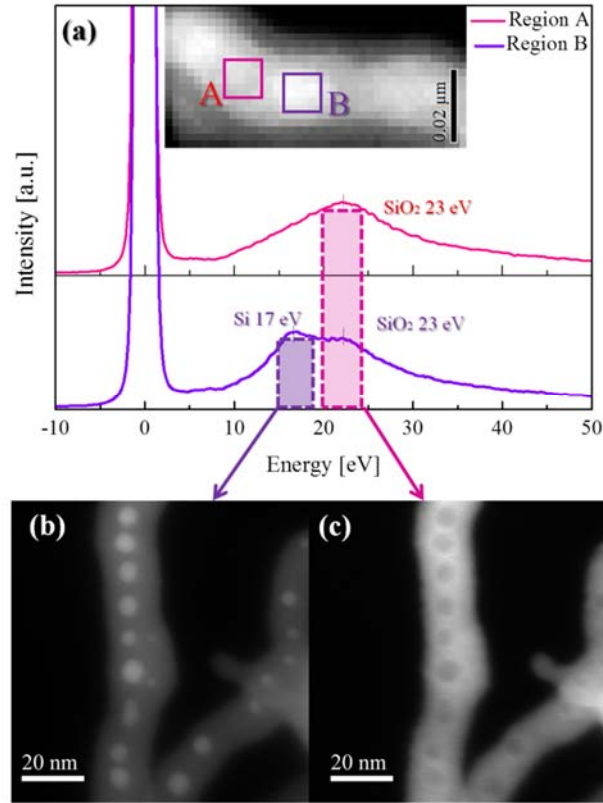


**Figure 3.8.** (a) Low-loss EELS spectra acquired in SI mode, corresponding to two different region of the nanostructure depicted in the HAADF image of the inset. (b) and (c) EFTEM images at the energy plasmon loss of Si and SiO<sub>2</sub>.

Figure 8(a) shows two low-loss spectra, acquired at 100 keV in SI mode. In the HAADF-STEM image reported in the inset, region A corresponds to the plasmon energy loss at 23 eV, while in B the superposition of two plasmon peaks at 17 eV and 23 eV are revealed. These plasmon peaks correspond to the plasmons of Si and SiO<sub>2</sub>, respectively. Thus, region B is associated to a SiNC, while region A is located in the silica wire between two adjacent SiNC. Indeed, it will be better described in the next chapter that the nanostructure represented by this HAADF image consists in a chain of SiNCs embedded in a silica NW.

Related to EELS spectroscopy, EFTEM technique allows to form the image by selecting energy loss electrons with an energy window centered in correspondence of a given feature of the EELS spectrum. Therefore, to map the presence of silicon, we put a 5 eV wide energy window in correspondence of the Si plasmon loss (17 eV); conversely, to obtain a chemical mapping of the oxide we fixed the energy window at 23 eV. The energy shift between the Si and SiO<sub>2</sub> plasmon peaks (about 6 eV) allows to neatly discriminate the Si contribution from the SiO<sub>2</sub> one and allows us to conduct energy filtered images by selecting plasmon loss electrons. As an example of the better contrast gained, we report in Fig. 8 (b) and (c) two EFTEM images of the

chain of SiNCs embedded in the silica wire, taken by selecting respectively the Si and SiO<sub>2</sub> plasmon loss electrons. This implies that in Fig. 8 (b) the bright spots are SiNCs while the grey regions correspond to the SiO<sub>2</sub> wire; in a complementary way, Fig. 8 (c) shows the bright background due to the presence of silica while the grey spots are the SiNCs.

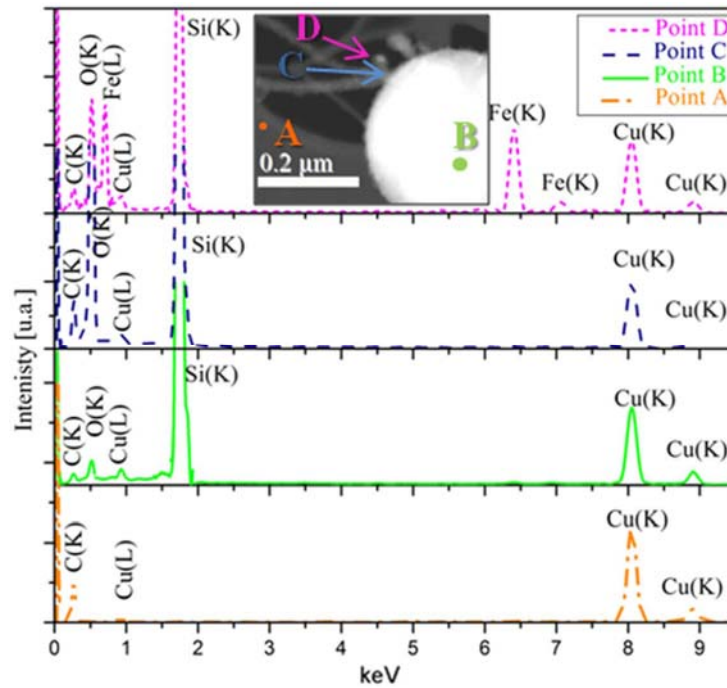


**Figure 3.8.** STEM-EDX spectra acquired at different points of ICP-SiNWs, as shown in the dark field image reported in the inset.

In addition, STEM-EDX analyses were carried out in order to corroborate the chemical investigations. Figure 9 shows typical STEM-EDX spectra of as-collected ICP-SiNWs. The correspondent points of the sample where the STEM-EDX were collected are illustrated in the dark field image reported in the insets. It emerges the presence of Fe in the point D, while only Si and O are present in points B and C of the sample, since the peak of C and Cu come from the underlying carbon lacey TEM grid used as a supporting substrate for the analysis (see point A).

Finally, during the PhD project also CL spectroscopy in SI mode has been performed. CL allows to study the optical properties of an ensemble of nanostructures, associated to electron-hole recombination in correspondence of their energy gap. Moreover, performing SI analysis in HAADF-STEM allows to localize, in the ensemble of nanostructures, those inducing luminescence [Dovrat07], with the typical spatial resolution lower than 100 nm [Williams09]. Until

now, optical properties on Si nanostructures have been measured on an ensemble of nanostructure by means of photoluminescence (PL) experiments, while the structural characterization on single nanostructure has been realised through TEM technique. Thanks to the expertise in nano-CL developed in Orsay, we managed to perform observations on SiNWs detecting CL spectra from small (some tens of nm<sup>2</sup>) portions of the samples. As it can be seen in Fig. 10 (b), it emerges a CL peak at about 320 nm, that is highly likely related to oxygen based defects present in the silica shell of the SiNW shown in Fig. 10 (a) [Shang06]. The CL spectrum due to the background was acquired in correspondence of the TEM grid (region B) and it is reported in red in Fig. 10 (b) as a reference. It is worth to notice that, in this case, the CL emission is associated to a very thin portion (less than 100 nm in length) of a single SiNW.

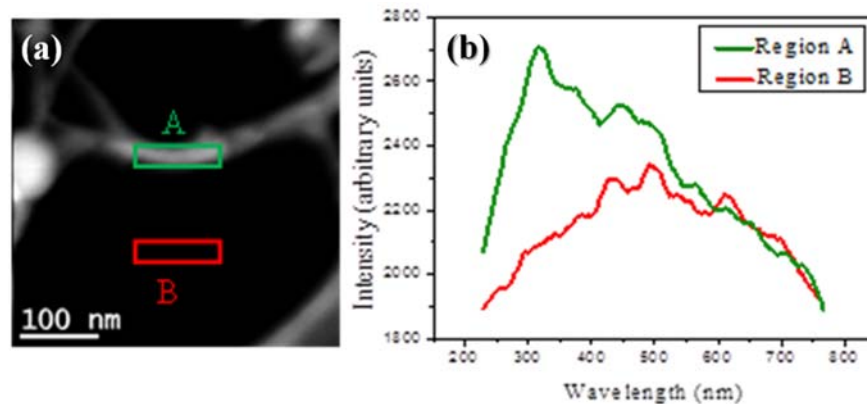


**Figure 3.9.** (a) Dark field TEM image of a single ICP-SiNWs, from which (b) optical emission has been detected via CL spectroscopy.

### 3.2.b Electron tomography

The main drawback of TEM is due to the fact that it essentially furnishes a 2D image of a 3D material. Basically, both the analytical and the spatial data are projected along the z-direction and hence the information along the z axis is lost. The possibility to have access to a more realistic tridimensional vision of nanomaterials' entities with the spatial and analytical resolution of a TEM is highly required. To this purpose, other 3D techniques are available, such us Atom Probe Tomography (APT) [Miller12] and X-Ray Tomography [Baruchel00]. Nevertheless, while X-Ray Tomography can attain a rather limited spatial resolution (of  $\sim 2 \mu\text{m}$ ), APT suffers a limited measurable volume (no more than 100 nm<sup>3</sup>) and sample destruction during analysis, even if better resolution (up to the single atom detection) can be achieved. In this context,

electron tomography (ET) accomplished with the use of the TEM arises as a remarkable technique to study a larger range of matter volumes, while still offering a spatial resolution that can go from  $\sim 1 \text{ nm}^3$  [Midgley03] down to atomic resolution in very recent microscopes [VanAert11, Scott12]. Electron tomography is accomplished through the reconstruction of a sequence of projection images, acquired by tilting the TEM sample holder. However, to achieve an accurate 3D reconstruction, all the images of the series should obey to the “projection requirement”, which states that the intensity of each micrograph must be a monotonic function of the physical property of the object [Hawkes06]. It is well known that conventional Bright Field (BF) and Dark Field (DF) imaging are dominated by diffraction contrast, thus in crystalline samples the contrast changes abruptly as long as the beam axis intercepts the different crystalline zone axes. More recently, this issue has been overcome whereas the improvement of HAADF in STEM associated with ET has been confirmed as the most appropriate mode to image crystals, since it meets the projection requirement, associating the contrast to the atomic number [Midgley03]. By combining HAADF and ET techniques along with EDX spectroscopy, it is possible to gather both imaging and analytical information at the same time. To perform ET analyses, the sample holder is tilted at regular angular sampling steps within a given angular range, as depicted schematically in Fig. 11. The maximum angular range is established not only by the specific sample holder used for the analysis, but also by the design of the objective lens, since the sample is located in a narrow region within the objective polepieces. Moreover, shadow effects are created by the TEM supporting grid at higher tilt angles.

Electron tomography was exploited for the study of tetrapod shaped [Arslan06] and octapods shaped particles [Brescia11], for the analysis of the distribution of metallic particles in carbon nanotubes or the location of carbon nanotubes inside cells [Porter07]. As far as 1D nanostructures like nanowires are concerned, tomography was employed, for example, to understand the shape of catalyst particles or distinguish embedded quantum dots from quantum dots just located at the nanowire surface [Inoue09, Wu08]. More specifically for SiNWs, ET was exploited to (i) depict the crystal facets in 3D, (ii) determine the spatial distribution of Au-catalyst residuals on Vapor Liquid Solid (VLS) grown SiNWs [Chen15, David13] and (iii) investigating the catalyst incorporation at the defect sites [Hemesath12]. It can be easily inferred that ET is paramount to get essential insight for the characterization of the above mentioned structures, since a 2D technique would give misleading information. It is also worth mentioning that in all these previous ET related studies, the SiNWs under analysis were relatively thick with diameters above 50 nm.

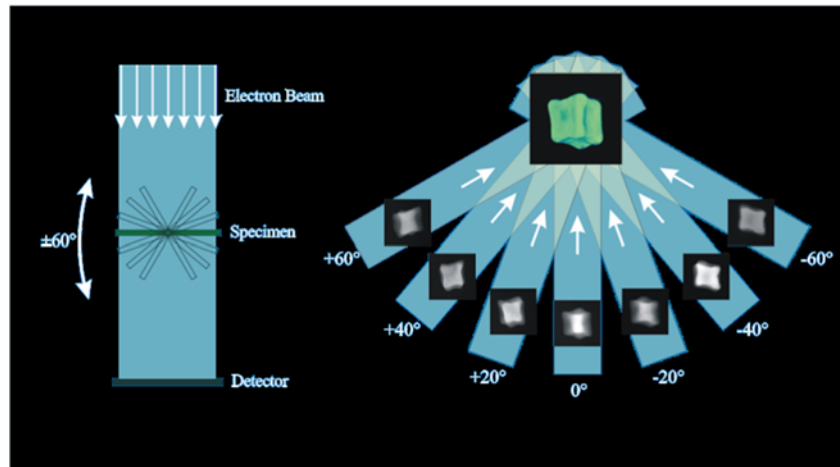


**Figure 3.11.** Sketch of the working principle of the electron tomography sample holder.

As we will see in the next chapter, ET was combined with STEM-EDX and energy filtered TEM (EFTEM) in order to definitely assert the mechanism of growth of ICP-SiNWs, thus emerging as a first attempt to study ultra-thin SiNWs via ET. The composer Kai software was used for the reconstruction, based on the filtered back projection (FBP) algorithm, while the Visualiser Kai software was used for visualization.

### 3.3. Photoluminescence spectroscopy

Similarly to CL spectroscopy, PL allows to study the energy band gap and thus the optical properties of materials. In fact, PL is suitable for the analysis of a large number of nanostructures and is complementary to CL since it gives information about the optical properties averaged on the sample. The main difference consists in the fact that CL uses electrons in TEM to excite the material, while lasers are used in PL.

The optoelectronic properties of the ICP-SiNWs were also characterized by means of PL measurements. The PL measurements were performed with the following experimental setups:

- An USB5000 Ocean optics CCD spectrometer employing a 405 nm (12 mW) solid state laser excitation line at room temperature with a 405 nm notch filter placed between the laser and the sample and a 475 nm long pass filter placed between the sample and the spectrometer. The emitted light was then collected through an optical fiber. These measurements were performed at the Institut National de la Recherche Scientifique - Centre Énergie Matériaux Télécommunications (INRS-EMT, Varennes, Canada).

- An AIST-NT OmegaScope 1000 equipped with a Nanofinder 30 Raman spectrometer and a cooled CCD detector, which provides for PL and Raman spectrometry as well as imaging. In order to carry out the optical spectrometry, we used the bright field configuration by exciting the sample with a green laser (solid-state cobalt 04-01 series,  $\lambda=532$  nm) focused through a 100 $\times$ , 0.7 numerical aperture (NA), with power on the samples equal to 5.4 mW and using the 150 lines/mm grating. Also these measurements were performed at the INRS-EMT.
- A Horiba-Jobin Yvon Xplora spectrometer, by using a grating with 300 groves/mm for light dispersion on a cooled CCD device. The excitation wavelength was 532 nm, focused on the sample though a 100x microscope objective (0.95 NA). Here, specific attention was paid to prevent any heating effect, and a very low laser power, less than 100  $\mu$ W was used (thus limited power density on the sample despite the high NA). The spot diameter is given by  $1.22 \lambda/\text{NA}$ . These measurements were conducted at the Centre d'Élaboration des Matériaux et d'Études Structurales - Centre National de la Recherche Scientifique (CEMES-CNRS, Toulouse, France).

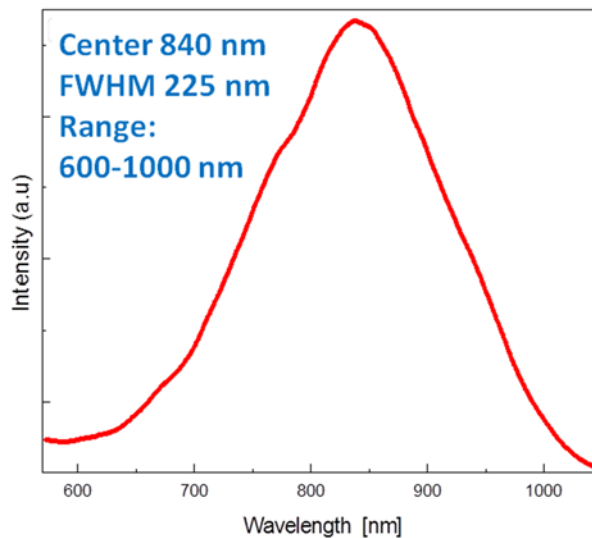


**Figure 3.12.** The typical PL spectrum acquired from the as collected SiNWs is centered in the visible-near IR range.

A typical PL spectrum of the ICP-SiNWs, shown in Fig. 12, presents the PL emission centered at about 830 nm. Similar PL spectra were already been observed in the case of Si nanocrystals, as reported previously in Refs. [Boninelli07, Ross08, DeBoer10].

### 3.4. Conclusions

In this chapter, the experimental details concerning both the synthesis process and the characterization techniques have been described. As it will be better described in the next chapters, the ICP-SiNWs have been found as a by-product after the synthesis of Si micropowders in an ICP machine usually exploited for the spheroidization process of rough powders. In order to intentionally reproduce SiNWs via ICP mechanism the reactor for nanopowder synthesis has been used. The main difference between these two systems mainly regards the presence of a quenching zone, where the cooling rate is typically very fast to obtain nanometric size [Guo10].

Since the ICP-SiNW characterization has been predominantly accomplished via TEM based techniques, TEM fundamentals have been recalled and a schematic of the instrument has been given, with particular attention to probe corrected STEM. In our case, STEM-EELS and STEM-EDX have been applied to study the local chemical composition of ICP-SiNWs. Both have been pursued at 100 keV to avoid beam damage at higher energies as well as the problem of plural scattering and of the low signal to noise ratio at reduced energies. Low-loss EELS spectra put in evidence the plasmon peaks of Si and SiO<sub>2</sub>, while EFTEM at 17 eV and 23 eV evidenced the structural composition of the ICP-SiNWs. High-loss EELS confirmed the presence of Si and O as well as an amount of nitrogen in the annealed sample, probably due to the incorporation of N<sub>2</sub> after the annealing. Moreover, as it will be described in more detail in the next chapter, ET allowed to achieve a 3D structural characterization of the ICP-SiNWs. Finally CL contributed to elucidate the optical properties of few SiNWs, while the optical properties of the overall sample have been probed via PL using different experimental setups. While CL spectra show the signal due to oxygen defects in the silica shells of the ICP-SiNWs, PL spectra exhibit in all the cases an emission in the near-IR range. Given the optical inability of Si to efficiently emit light, the origin of the near-IR emission deserves to be elucidated, as it will be shown in the next chapter.

### Bibliography

[Arslan06] I. Arslan, J. R. Tong and P. A. Midgley Ultramicroscopy 106, (2006).

[Baruchel00] J. Baruchel, J. Y. Buffiere, E. Maire, P. Merle, G. Peix,. X-ray tomography in material science, Hermes science publications: Paris, France, (2000).

- [Brescia11] R. Brescia, K. Miszta, D. Dorfs, L. Manna, and G. Bertoni, *J. Phys. Chem. C* 115, 41 (2011).
- [Chen15] W. Chen, P. Pareige, C. Castro, T. Xu, B. Grandidier, D. Stiévenard and P. R. i Cabarrocas, *Journal of Applied Physics* 118, (2015).
- [David13] T. David, L. Roussel, T. Neisius, M. Cabie, M. Gailhanou and C. Alfonso, *J. Cryst. Growth* 383, (2013).
- [Dovrat07] M. Dovrat, N. Arad, X. H. Zhang, S. T. Lee and A. Sa'ar, *Phys. Rev. B* 75, 20 (2007).
- [Egerton11] R. F. Egerton, *Electron energy-loss spectroscopy in the electron microscope*, Springer Science & Business Media (2011).
- [Guo95] J. Y. Guo, F. Gitzhofer and M. I. Boulos, *J. Mater. Sci.* 30, (1995).
- [Guo10] J. Y. Guo, F. Xiaobao, R. Dolbec, X. Siwen, J. Jurewicz and M. Boulos, *Plasma Sci. Tech.* 12, 2 (2010).
- [Hawkes06] Hawkes, P.W. The electron microscope as a structure projector. In: *Electron Tomography Methods Three-Dimensional Visualization of Structures in the Cell*, Joachim Frank Editor, Springer: New York, USA, (2006).
- [Hemesath12] E. R. Hemesath, D. K. Schreiber, E. B. Gulsoy, C. F. Kisielowski, A. K. Petford-Long, P. W. Voorhees and L. J. Lauhon, *Nano Lett.* 12, (2012).
- [Houdellier14] F. Houdellier, Aberration corrected electron microscopy, Presentation for the Beyond Nano Project, CNR-IMM of Catania, April 2014.
- [Inoue09] K. Inoue, F. Yano, A. Nishida, H. Takamizawa, T. Tsunomura, Y. Nagai and M. Hasegawa, *Ultramicroscopy* 109, 12 (2009).
- [Liao07] J. Liao, *Practical Electron Microscopy and Database - An Online Book* (2007), available at [www.globalsino.com/EM/](http://www.globalsino.com/EM/) (Accessed: 10/01/2017).
- [Midgley03] P. A. Midgley, M. Weyland, *Ultramicroscopy* 96, (2003).
- [Miller12] M. K. Miller, T. F. Kelly, K. Rajan, S. P. Ringer, *Mater. Today* 15, (2012).
- [Pennycook14] S. J. Pennycook, Fulfilling Feynman's dream: "Make the electron microscope 100 times better" - Are we there yet?, Presentation at the plenary session of the 1st Italian EELS school, Catania, May 2014.

[Porter07] A. E. Porter, M. Gass, K. Muller, J. N. Skepper, P. A. Midgley and M. Welland, *Nat. Nanotechnol.* 2, 11 (2007).

[Scott12] M. C. Scott, C.-C. Chen, M. Mecklenburg, C. Zhu, R. Xu, P. Ercius, U. Dahmen, B. C. Regan, J. Miao, *Nature* 483, (2012).

[Shang06] N. G. Shang, U. Vetter, I. Gerhards, H. Hofsäss, C. Ronning and M. Seibt, *Nanotechnology* 17, 13 (2006).

[VanAert11] S. Van Aert, K. J. Batenburg, M. D. Rossell, R. Erni, G. Van Tendeloo, *Nature* 470, (2011).

[Williams09] D. B. Williams and C. B. Carter, *Transmission electron microscopy: A Textbook for Material Science*, Springer US (2009).

[Wu08] Y. H. Wu, L. Chang, L. C. Chen, H. S. Chen and F. R. Chen, *Appl. Phys. Lett.* 93, 15 (2008).

[www.tekna.com] Info available at: [www.tekna.com](http://www.tekna.com), (Accessed: 01/12/2016).

## **CHAPTER 4:**

# **INVESTIGATION OF SINWS SYNTHESIZED BY ICP**

The results concerning the investigation of the novel and high throughput ICP-synthesized nanopowders will be presented and discussed in this chapter. To this purpose, in the first paragraph, the approach based on the use of Transmission Electron Microscopy (TEM) techniques to accomplish the investigation of the structural and chemical characteristics of nanostructures is explained. It will be demonstrated that these nanomaterials are composed of an ensemble of spherical Si nanospheres (SiNSs) as well as filamentary Si nanowires (SiNWs). However, it should be considered that the detection of SiNSs was expected since they derive from the spheroidization process that is at the basis of ICP micropowder synthesis. On the other hand, the discovery of ultra-thin SiNWs was highly surprising because, in principle, the ICP process was not intended for the SiNW production. Thus, being these SiNWs produced by the ICP process for the first time, their structural features have not yet been explained. The synergetic use of Energy Filtered TEM (EFTEM), High Resolution TEM (HRTEM), Scanning Transmission Electron Tomography, Scanning TEM-Energy Dispersive X-ray spectroscopy (STEM-EDX), and Electron Energy Loss Spectroscopy (EELS) allowed to shed light on their structural properties, which are described in the second paragraph of this chapter.

Moreover, these findings allowed to infer the physical mechanisms responsible for the SiNW growth, which are described in the third paragraph. Finally, the room temperature PL measurements and their interpretation in the light of Quantum Confinement (QC) theory will be the subject of the third paragraph.

### **4.1. Structural and chemical characterization**

The Si nanopowders investigated in the present work were formed as a by-product of a ICP spheroidization process exploited by Tekna Plasma Systems Inc. (Canada) to produce industrial quantities of micro spherical silicon [Guo95]. To perform this study, the as-collected powder depicted in Fig. 1(a) has been considered. Few amount of the powder has been dissolved in isopropilic alcohol and, after a sonication procedure of ~5 mins, an almost homogeneous and brown-colored solution is formed, as it can be seen in Fig. 1(b).

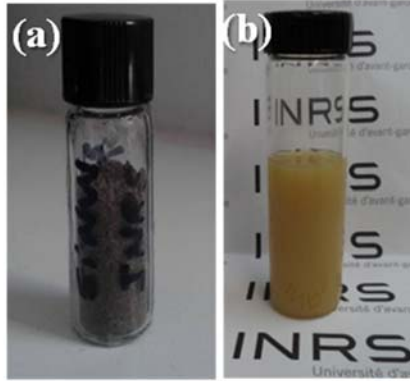


**Figure 4.1.** (a) Small amount of the “as-collected” Si powder found after the spheroidization process exploited in conventional ICP. (b) Solution prepared by dispersing the Si powder in isopropyl alcohol.

Few drops of such solution have been dropcasted onto a Si substrate for SEM analyses and onto carbon lacey Cu or Au grids for TEM analyses, in order to have a sparse array of nanostructures on the supporting substrate. A typical SEM image is reported in Fig. 2, depicting the as-collected nanomaterial as a mixture of entangled, thin and very long nanowires along with large nanospheres. Statistical SEM analyses assess that the sizes of the spheres range from 50 up to 500 nm, while the nanowires are 1-2  $\mu\text{m}$  long. In addition, higher magnification imaging achieved via conventional Bright Field TEM puts in evidence that the size of nanowires is  $\sim 10$  nm large, as can be seen in the inset of Fig. 2.

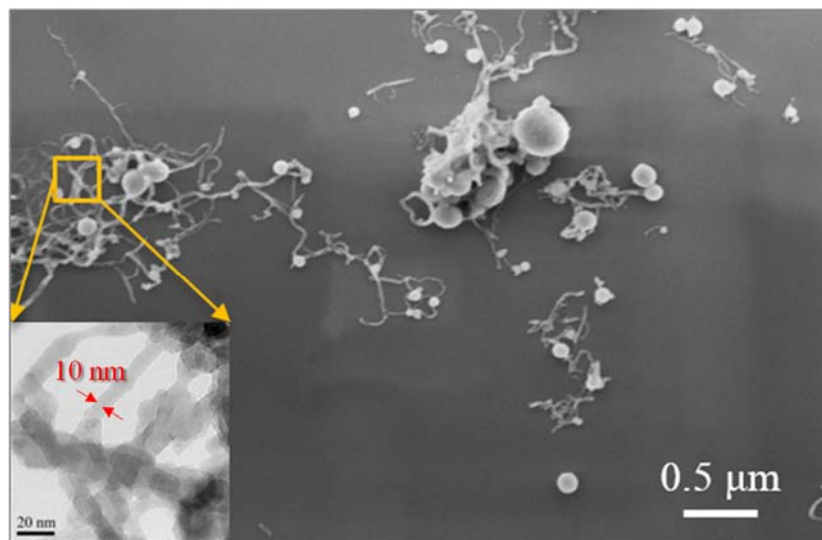


**Figure. 4.2.** Typical SEM image of the ICP-Si nanopowder based sample, showing an array of nanowires and nanospheres. A typical bright field TEM of the nanowires is depicted in the inset.

Furthermore, EFTEM analyses, taken at 99 and 531 eV, corresponding to the Si L<sub>2,3</sub> and O K edges, respectively, revealed that the ICP-synthesized nanostructures, i.e. both SiNSs and SiNWs, are composed of a Si core (red colored) covered by a silicon oxide shell (green colored), as illustrated in Figs. 3(a and b). Statistical analyses on several hundreds of nanostructures observed by EFTEM allowed to determine that the diameter of the SiNS core is in the 45-480 nm range and that they are surrounded by a  $\sim 8 \pm 2$  nm thick silicon oxide shell. Interestingly, the SiNWs present an ultra-thin Si core with diameters in the 2-15 nm range, covered by a silica shell of which thickness varies from 4 to 15 nm. Further EFTEM examinations, performed at 17 eV, i.e. the plasmon energy losses of Si, revealed that the SiNW core presents an intriguing structure. More precisely, three main configurations of the Si core can be recognized:

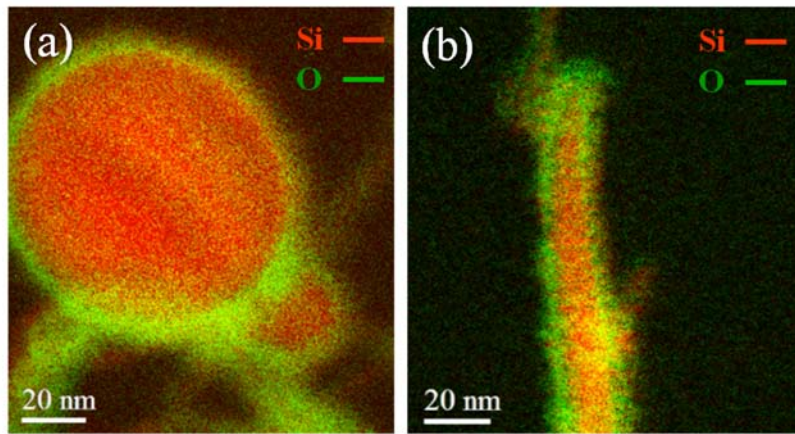


**Figure 4.3.** Energy Filtered TEM of (a) a SiNS and (b) a SiNW, demonstrating a structure of ICP-Si nanostructures made up of a Si core (in red) and a SiO<sub>2</sub> shell (in green).

- i) SiNWs presenting a cylindrical Si nanocore wrapped by a concentric silica shell, referred to as “cylindrical SiNWs” hereafter and depicted in Fig. 4(a).
- ii) NWs consisting of isolated spherical Si nanocrystals (SiNCs) encapsulated into a continuous silica cylinder, as shown in Fig. 4(b). This configuration will be referred to as “SiNC chains” hereafter. Their crystalline nature is ascertained by HRTEM analyses, as shown in the inset of Fig. 4(b).
- iii) An intermediate case between the above-described cylindrical SiNW and the chain-like configuration, where a modulated Si nanocore features a chain with almond-shaped SiNCs connected by a very thin Si wire (diameter of  $\sim 2$  nm). These configurations will be referred to as “chapelet-like” SiNWs hereafter and is illustrated in Fig. 4(c).

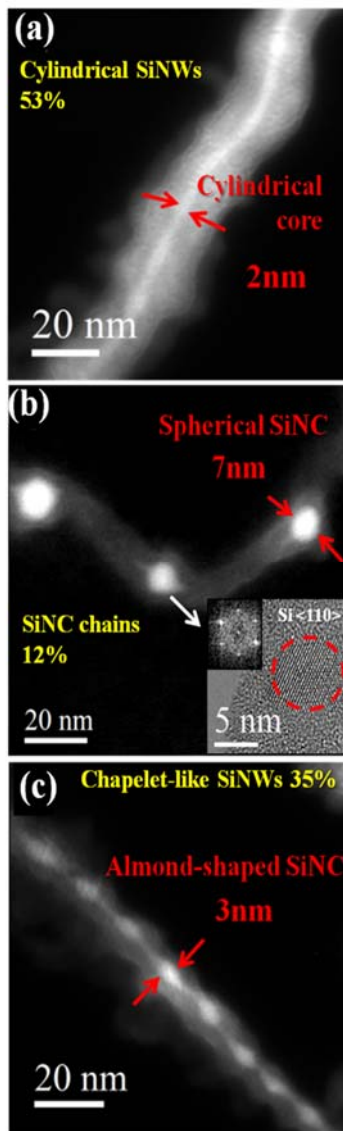


**Figure. 4.4.** Energy Filtered TEM acquired at 17 eV, showing the three internal configurations of ICP-SiNWs: (a) a cylindrical Si nanocore, (b) a chain composed of spherical SiNCs whose crystalline nature is clarified by the HRTEM in the inset and (c) chapelet-like wire composed by almond-shaped SiNCs connected by a very thin SiNW. Cylindrical SiNWs represent ~53% of the whole population, while the SiNC chains constitute ~12% and the "chapelet-like" are ~35%.

Statistical EFTEM analyses were also performed on hundreds of SiNWs, allowing to evaluate that the cylindrical SiNWs represent ~53% of the whole SiNW population in the samples, while the "chapelet-like" SiNWs count for ~35% and the SiNC chains constitute ~12%. Moreover, the size distributions relatively to the three different configurations have been evaluated, taking also into account the accuracy of the TEM. In this way, it has been estimated that the cylindrical

SiNW mean diameter is equal to  $2.7 \pm 1.0$  nm, while the mean diameter of the almond-shaped SiNCs composing the chapelet-like SiNWs is  $4.5 \pm 1.4$  nm and that of spherical SiNCs forming the chains is equal to  $7.0 \pm 2.7$  nm, as reported in Fig. 5(a, b and c), respectively. The physical mechanism behind the occurrence of these three morphologies of the Si core will be discussed in detail in the sixth chapter

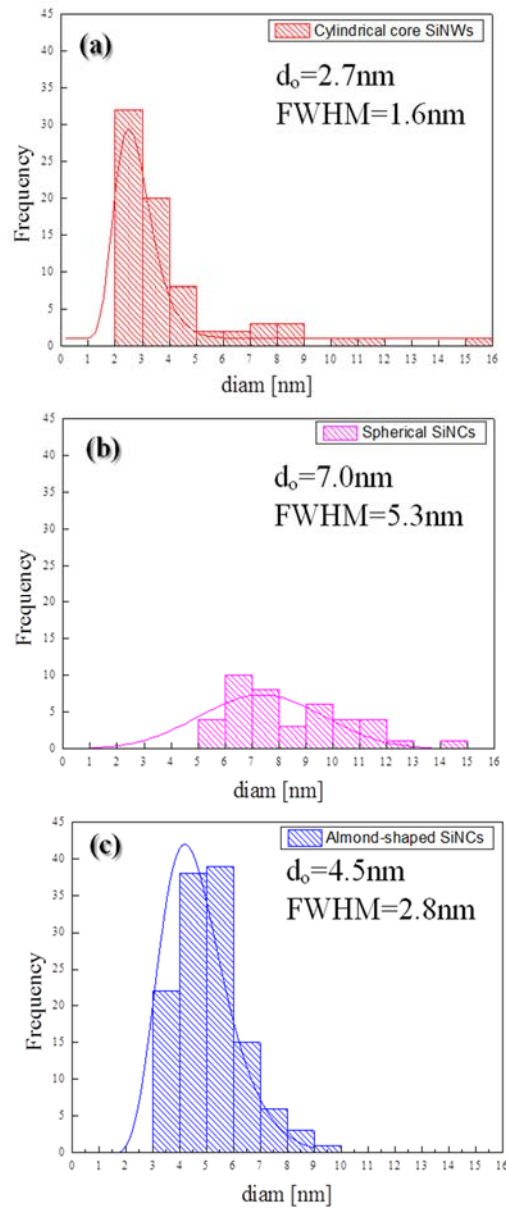


**Figure 4.5.** Diameter distributions relative to: (a) the cylindrical SiNWs, (b) almond-shaped SiNCs and (c) spherical SiNCs.

## **4.2. Growth mechanisms of ICP-produced SiNWs**

### **4.2.a SiNWs produced by Oxide Assisted Growth mechanism**

Once detailed the internal morphology of SiNWs, further investigations on their chemical composition were carried out in order to better understand the mechanism through which the SiNW growth occurs in the ICP system. First of all, it can be noticed from the EFTEM images shown in Fig. 6 (a, b, and c), that all the three morphologies of SiNWs have a common characteristic being directly grown from the silica shell covering the SiNSs, without any structural continuity with the nanosphere Si core. The continuum silica shell covering the SiNS at the root of the growing NW is clearly depicted in the bright field TEM image reported in the inset of Fig. 6(a), where the silica layer shows the typical contrast of the amorphous phase while the upper extremity of the SiNS appears dark owing to the diffraction contrast provoked by its crystalline phase.

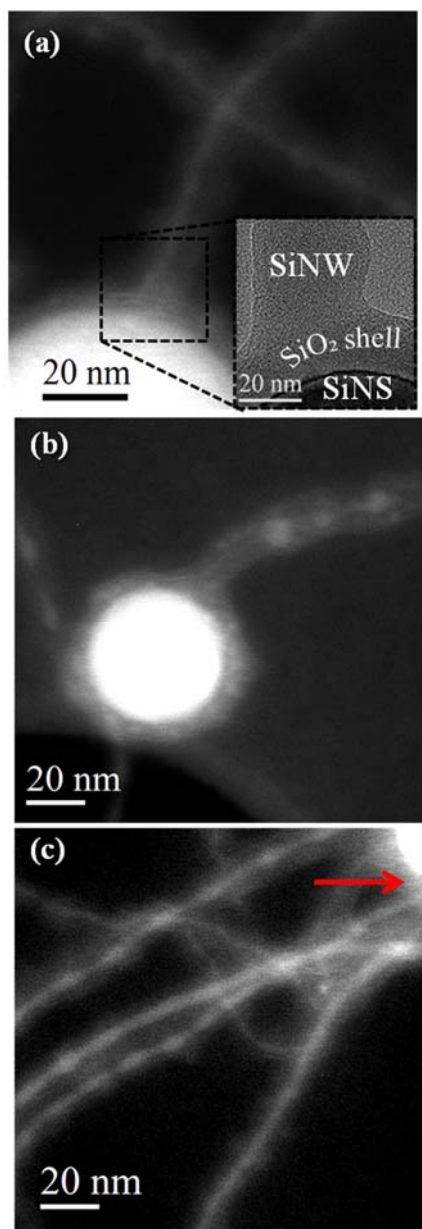


**Figure. 4.6.** EFTEM images acquired at 17 eV showing that (a) cylindrical SiNWs, as well as (b) SiNC chains and (c) chapelet-like SiNWs originate from the silica shell covering the SiNSs, as indicated by the arrow in (c) and better detailed in the inset of (a).

Moreover, by means of STEM-EDX, a chemical characterization has been performed at the nanometric scale on some tens of SiNWs and SiNSs, from which they sprout out. EDX spectra were acquired in correspondence of three different locations on each nanostructure, namely: (i) on the top of the NW (point C in the High-Angle Annular Dark Field (HAADF)-STEM image of Fig. 7, (ii) along the wire (point B), (iii) above the carbon lacey Cu grid (point A, which is used as a background reference). For ~95% of the SiNWs examined, only the Si and O signals

were observed, as shown by typical STEM-EDX spectra in Fig. 7. This is in agreement with the previous EFTEM analyses, which put in evidence the Si-silicon oxide core-shell structure.

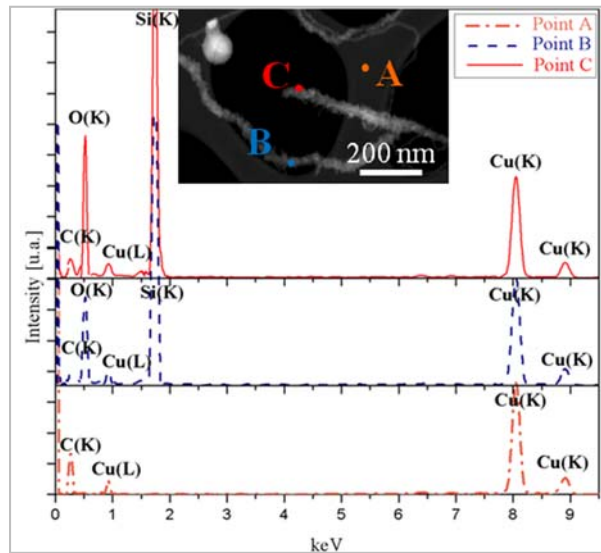


**Figure 4.7.** Typical STEM-EDX spectra relative to the 95% of the ICP-SiNWs. The spectra were acquired on the carbon lacey TEM grid (A, orange color), along the SiNWs (B, blue color), on the top of the SiNWs (C, red color), as shown in the corresponding HAADF-STEM image.

By gathering all the information obtained from the structural and chemical characterizations described so far, it has been inferred that OAG is the mechanism behind the formation of this 95% ICP-produced SiNWs. Indeed, the main feature of OAG relies on the fact that Si and O are the only chemical elements composing the SiNWs, while no metal traces are present on them [Zhang00], as it has been assessed by the statistical STEM-EDX analyses illustrated above, of which the sensitivity is  $<1$  at.%. The statement about the absence of any metallic contamination on the majority of the ICP-SiNWs has been further supported by inductively coupled plasma mass spectrometry, of which chemical sensitivity is much higher than EDX technique and which demonstrates the presence of small traces of Fe ( $\sim 0.2\%$ ), inadequate to sustain a VLS based growth of the whole SiNW population. However, we will see that such a small amount instead leads to the VLS growth of the remaining 5% of the ICP-SiNWs.

As far as the OAG mechanism is concerned, it has been already described in chapter 2 that the growth of SiNWs via OAG occurs in an environment composed of Si vapor enriched by Si-suboxide clusters. According to the OAG theory, the growth is initiated by a Si suboxide cluster that is bonded to a Si-based substrate, which can be both Si or Si oxide [Lee00]. Hence, it is possible to describe the growth of the OAG-SiNWs in the ICP system as follows. Inside the

ICP reactor the Si feedstock is partially sublimated and the resulting Si vapor actively interacts with the oxygen present in the reactor. The oxygen originates mainly from the native oxide layer at the surface of Si feedstock powder, which is partially released during the spheroidization process (it is commonly observed that powders processed by ICP exhibit enhanced purity as compared to feedstock). Theoretical models have shown that hot vapors of Si and O are largely constituted of silicon suboxide clusters, representing the appropriate environment for the occurrence of OAG-based SiNW growth [Zhang01, Zhang04]. At the same time, given the non-equilibrium conditions inside the ICP reactor, it is highly likely that the spheroidization occurs while some remaining hot vapors are present in the chamber. The SiNSs can act as substrate onto which other SiNWs can grow according to the OAG model, as schematically sketched in Fig. 8 (adapted from Fig. 5 in ref. [Lee00]). So, analogously to the OAG model, if a Si suboxide cluster deposits on a SiNS, it can act as a nucleus that adsorbs additional reactive Si suboxide clusters from the vapor. Meanwhile, the oxygen atoms may diffuse to the edge. This results in the formation of a chemically inert Si oxide shell that prevents lateral growth, so only perpendicular growth is possible [Zhao03]. This OAG based unidirectional growth is initiated by the formation of a Si-Si bonding, established between the silicon suboxide cluster and the  $\text{SiO}_2$  shell of the SiNSs, as observed in the case of our SiNWs in the inset of Fig. 6(a) and sketched in Fig. 8 [Agati16].

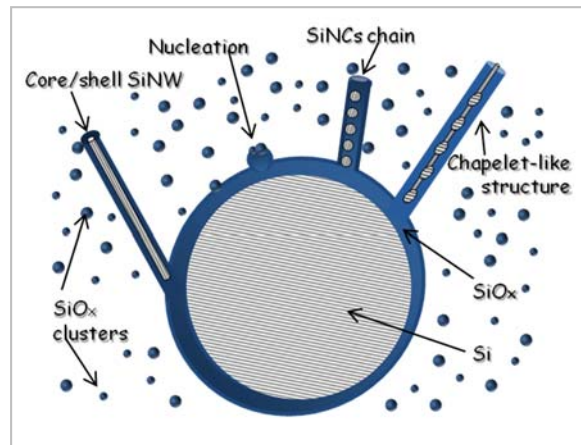


**Figure 4.8.** Sketch of SiNW formation via the OAG mechanism, illustrating the nucleation operated by a Si suboxide cluster on the silica shell of the SiNS, which represents the substrate for SiNW growth. According to this model, the formation of SiNC chains or chapelet-like nanostructures is also possible [Zhang03].

Finally, it should be added that the OAG mechanism is generally reported for synthesis temperatures between  $850^{\circ}\text{C}$ - $1100^{\circ}\text{C}$  [Lee00, Peng01,Zhang03], which are easily reached in the

post-discharge section of the induction plasma torch. Thus, it is possible to conclude that the majority of the SiNWs investigated here are formed via the OAG mechanism in the post-discharge zone of the ICP reactor.

#### 4.2.b SiNWs produced by Vapor Liquid Solid mechanism

About 5% of the ICP-SiNWs were found to exhibit diverging characteristics as compared to the ones analyzed above. They are shorter, with a length rarely exceeding 150 nm. More importantly, they show a dark spherical particle at their tip and are found to sprout out directly from the Si core of a massive underlying SiNS, as illustrated in Fig. 9, and not from the SiO<sub>2</sub> shell as the SiNWs described above. A higher magnification view of the SiNW-SiNS interface [see Fig. 9(b)] shows three SiNWs superimposed on each other. Indeed, correspondingly, we can see three nanoparticles (indicated by the arrows) at the tips of these three SiNWs growing perpendicularly from the larger SiNS. The HRTEM image of the top particle, shown in the inset of Fig. 9(b), presents a series of fringes separated by a distance equal to 0.5 nm. Such an interplanar distance is compatible with the 0.5 nm distance between (001) planes in  $\beta$ -FeSi<sub>2</sub> [Morales98].

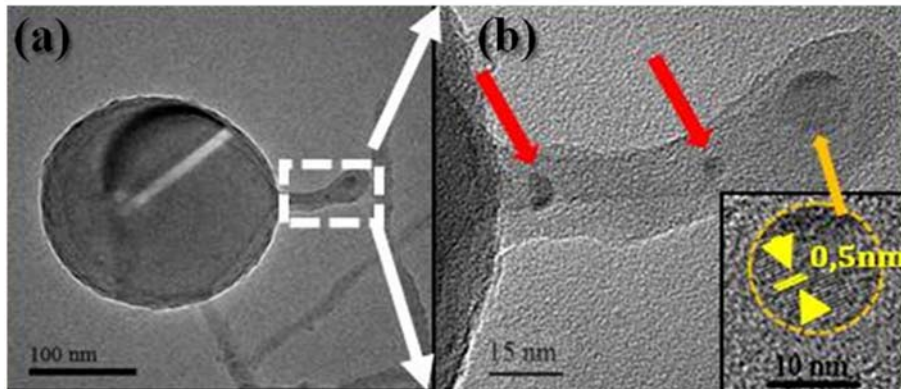


**Figure 4.9.** (a) Bright Field TEM image showing a SiNS, whose core generates three perpendicular NWs. (b) Enlarged image on the NWs. The arrows indicate three small nanoparticles at the end of each wire; in particular the top particle, enlarged in the inset, presents interference fringes corresponding to 0.5 nm interplanar distance.

The presence of such compound is in agreement with the Fe-Si phase diagram, which shows that FeSi<sub>2</sub> is the most stable compound in the Si-rich zone of the diagram at high temperatures [Morales98], a condition easily met in the ICP discharge zone. To ascertain the presence of Fe-

containing nanoparticles at the tip of these shorter SiNWs, STEM-EDX chemical analyses were performed by setting the probe (A) above the small particle at the tip of the nanowire and (B) along the nanowire. Figure 10 shows the STEM-EDX spectra along with the HAADF image where the locations A and B are illustrated. Remarkably the spectrum acquired from region A (red continuous line) clearly demonstrates the presence of Fe, while there is no evidence of any metal trace in the spectrum acquired along the SiNW (region B, blue dashed line), where only Si and O signals were detected. These observations corroborate well with the VLS model predictions, where metal-containing particles at the tip of the SiNWs are typical marks of a metal-catalyzed growth.

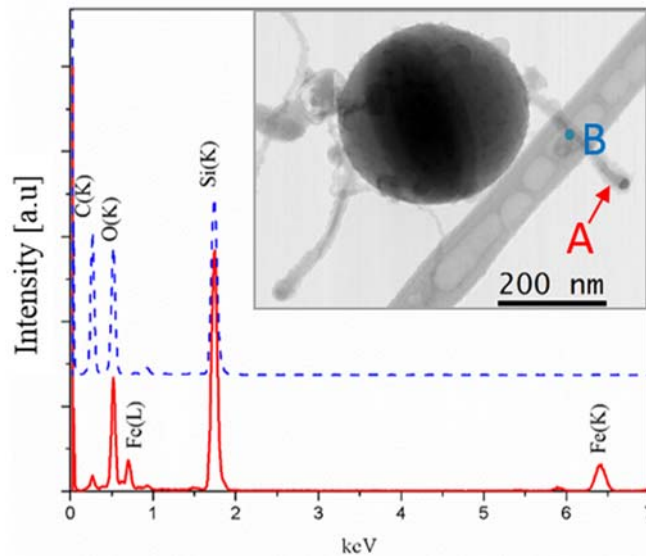


**Figure 4.10.** Typical STEM-EDX spectra exhibited by ~5% ICP-SiNWs, as the one displayed in the BF TEM image in the inset. The (A) and (B) locations are also shown.

Several STEM-EDX analyses ensure that dark nanoparticles at the tip of the SiNWs, like the ones shown in the inset of Fig. 10, always contain Fe. In addition, Fig. 11(a and b) illustrates typical EFTEM images of these 5% of the ICP-SiNWs, taken at 17 eV and 23 eV respectively (the Si and SiO<sub>2</sub> energy plasmon losses). By comparing these images, it can be noted that the catalyst nanoparticle size matches exactly the SiNW core diameter at its tip and a unique Si core continuously connects the NW and the NS from which the nanowire originated [as indicated by the arrow in Fig. 11(a)], while there exists also a structural continuity between the oxide shell of the SiNW and the SiNS.

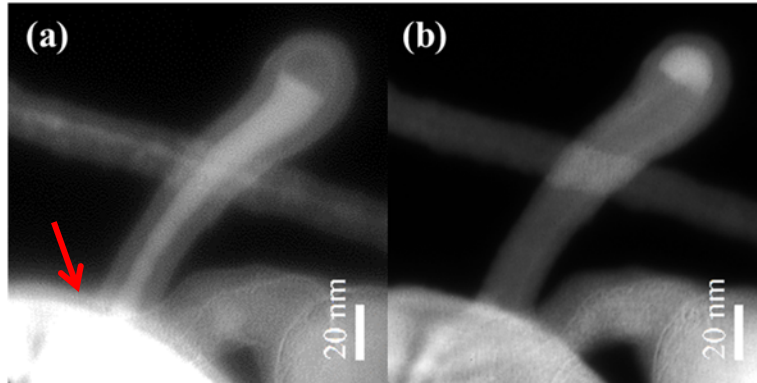


**Figure 4.11.** EFTEM images acquired at the plasmon energy loss of (a) Si, and (b) SiO<sub>2</sub>. The arrow indicates the structural connection between the Si core and the SiNS, as well as the continuity of the oxide shells of the SiNW and the SiNS.

These findings confirm that the Si core (and not the silica shell) of the SiNSs acted as a substrate for these SiNW growth, as already inferred from Fig. 9 and as required in the VLS model in which a substrate of Si is needed.

#### **4.2.c 3D reconstruction of VLS SiNWs by Scanning Transmission Electron Tomography**

A conventional 2D TEM imaging cannot definitely demonstrate whether the nanoparticle is embedded inside the SiNWs or located at their tip. To unequivocally settle this point, a 3D STEM tomography characterization at the nanoscale has been performed. Focus was put on the nanostructures shown in Fig. 12 (a). The rotating axis of the tomography holder, depicted in Fig. 12 (d), was nearly aligned to the top right NW in Fig. 12 (a), allowing us to tilt the sample from -50° to +57° with a step of 2°, without any shadowing effect caused by the C layer of the TEM grid. By following this procedure, we acquired 55 images at different projections in HAADF mode. In Fig. 12 (a, b, and c) three HAADF-STEM micrographs of this series of images are illustrated, being acquired with tilting angles of 0°, 35° and 70°. Image shift compensation and focus were manually adjusted during acquisition.

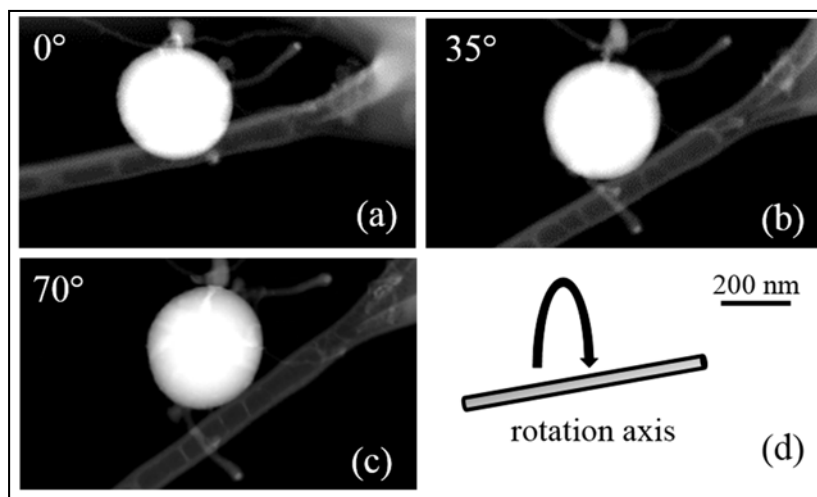


**Figure 4.12.** HAADF-STEM micrographs of a SiNS with two connected SNWs, acquired at (a) 0°, (b) 35° and (c) 70° of sample rotation along the rotation axis shown in (d).

From the inspection of Fig. 12 (a) alone we cannot discern whether the SiNW at the bottom is connected to the SiNS or not. However, when the nanostructure is tilted at 70° it appears evident that this SiNW grows directly from the SiNS. Moreover, these HAADF images clearly demonstrate that both SiNWs exhibit a nanoparticle at their top. The reconstructed 3D volume composed by the SiNWs connected with the SiNS is represented in Fig. 13. The different elements of the reconstructed volume have been shown separately in Fig. 13 (b, c, and d). This was accomplished by performing the same reconstruction four times. Thus, by combining the four different areas of interest as in Fig. 13 (a), it is possible to distinguish the SiNS in yellow, the two SiNWs in green, the two nanoparticles in darkish red and the carbon support layer in blue.

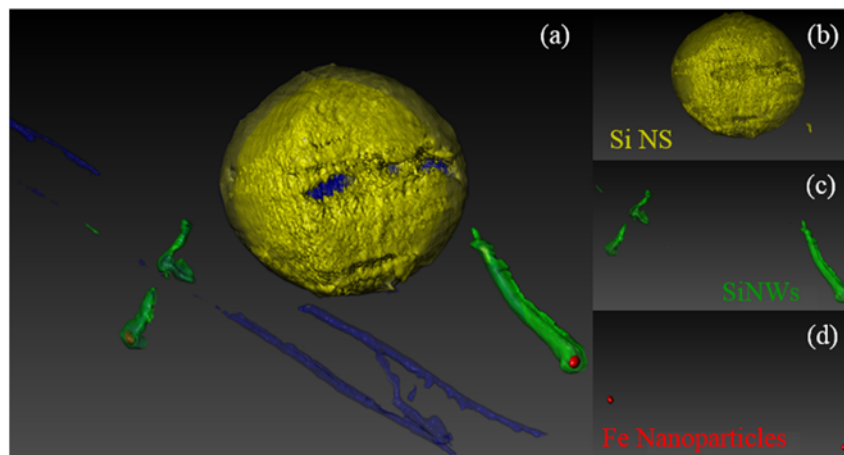


**Figure 4.13.** Volume reconstruction of the system formed of a SiNS and two SiNWs. The different areas of interest, namely the (b) SiNS, (c) the SiNWs and (d) and the Fe particles have been reconstructed separately and then combined in (a).

From this 3D reconstruction, it can be concluded that the nanoparticles are located on the top of the SiNWs, and not embedded inside them, as it could be misleadingly inferred by a conventional 2D TEM image, as the one displayed in Fig. 9. On the other hand, owing to the poor contrast in correspondence of the base of SiNWs, it was not possible to reconstruct the SiNW-SiNS interface. However, this issue is clarified by means of EFTEM images, like the ones depicted in Fig. 11, which demonstrate the connection between the SiNW core and the SiNS.

The combination of EFTEM and HAADF-STEM tomography allows to definitively demonstrate that the formation of SiNWs through the catalyzed VLS growth is also possible in the ICP reactor as long as a metal catalyst is present in the reaction zone. In the present experiment, even if the catalyzed SiNWs growth was not intended, the Si feedstock used in the spheroidization process contained some Fe impurities. The presence of iron has been ascribed to contaminations present in the feedstock. It should be noticed that the Fe concentration in the as collected powder is  $\sim 1770$  ppm (i.e. less than the 0.2%) as measured by inductively coupled plasma mass spectrometry. Therefore, we argue that some Fe nanoparticles form on the larger SiNSs during the ICP process. These Fe nanoparticles become supersaturated by the diffused Si atoms, which constitute the vapor inside the ICP chamber, as said before. Thereby the precipitation of Si occurs in the Fe-Si droplets, leading to the formation of the SiNWs. Further reaction with the oxygen derived by the native oxide of the Si feedstock causes the oxidation of the structures inducing the oxide outer-shell formation. So, this very low Fe concentration is not sufficient to sustain the growth of the whole NW population but it was found to be the responsible for the VLS growth of about the 5% of the whole population of NWs. This finding

demonstrates that the VLS growth of SiNWs is possible via the ICP technique, whereas specific metallic contents are introduced in the Si feedstock [Agati16a].

Finally, it should be noticed that some HAADF images revealed the presence of some black spots on the SiNSs' surface (as those shown over the SiNS reported in the inset of Fig. 14) from which no SiNW emerges. To better elucidate the chemical nature of this particles, EDX-spectra were acquired in correspondence of the dark spot (point A) and in correspondence of no-contrast regions (point B), as illustrated in Fig. 14.

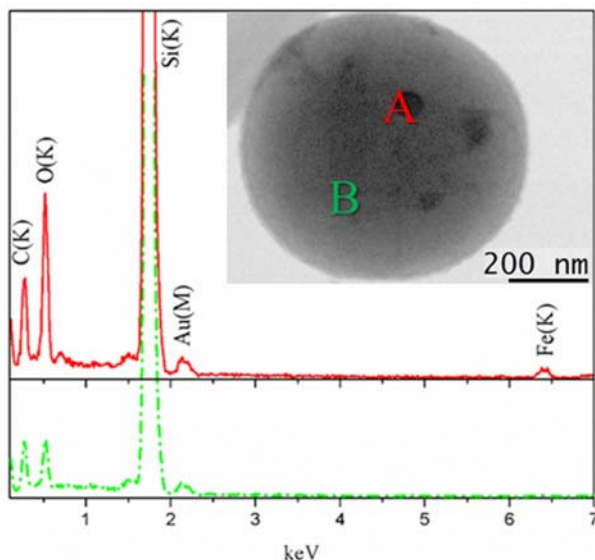


**Figure 4.14.** STEM-EDX spectra acquired in correspondence of a dark spot on the surface of the SiNS (point A in the STEM image) and above a no-contrast region, like the point B. The STEM-EDX spectrum acquired at the point A shows that although iron is present, no NW growth was induced.

It was observed that, while the peaks of Au and C comes from the supporting TEM grid, only Si and O signals are revealed in correspondence of point A (green dot-dashed line), whereas point B indicates the additional presence of iron in correspondence of the nanoparticle (red continuous line). In literature, it has been demonstrated that Fe-catalyzed VLS growth take place at temperatures not lower than 1150°C [Morales98]. This leads us to suppose that also for ICP no VLS-induced SiNW growth occurs on those SiNSs formed at temperatures lower than 1150°C, which can be reached near the borders and at the bottom of the ICP reactor [Guo10].

#### 4.2.e Surface diffusion above the Fe catalyst

An interesting feature, typical of these VLS-SiNWs, is that the diameter of the nanowire at the top is thicker than at its basis, as detailed in the EFTEM in Fig. 15 (a), suggesting that the radial growth is enhanced at the top with respect to the SiNW basis. It could be envisaged that this peculiar enlargement is due to the surface diffusion of Si atoms above the metal catalyst towards the solid-liquid interface, where they are finally incorporated into the solid phase at the three phase boundary line, as it has been described in the first paragraph of Chapter 2. Since Wang and [Wang08] demonstrated that surface diffusion above the catalyst surface is enhanced at lower temperatures [Wang08], it can be conjectured that this surface diffusion mechanism becomes competitive with respect to the axial growth during the cooling phase of the ICP process.

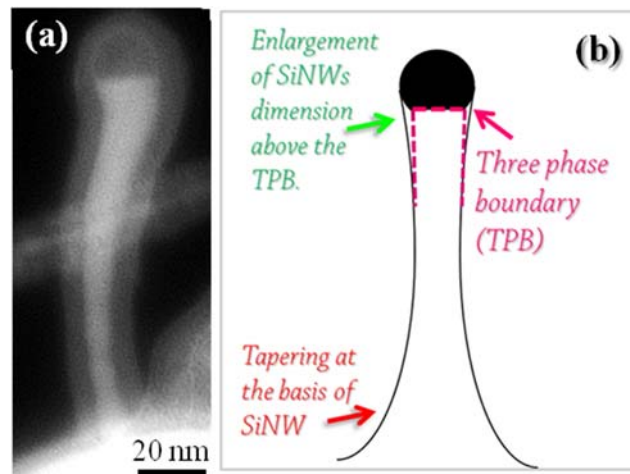


**Figure 4.15.** (a) Typical EFTEM image of an ICP-SiNW grown via VLS mechanism, which presents an enlargement of the diameter at the top, in correspondence of the Fe catalyst-NW interface; (b) sketch of a SiNW where the effect of the tapering and of the surface diffusion above the catalyst particle are evident.

In Figure 9 it can be also noticed an enlargement at the bottom of the SiNW connected to the underlying SiNS. An enlargement of the SiNW basis is commonly ascribed to the diffusion of the Si atoms on the substrate, which are then incorporated in the SiNW. This phenomenon is known as “tapering” and is often observed in VLS-grown SiNWs, becoming more important for thinner SiNWs. Both the effects of surface diffusion of Si atoms above the catalyst and the tapering are sketched in Fig. 15(b).

### 4.3. Quantum confinement effect in ICP-SiNWs

Once the TEM analyses confirmed the nanosize distribution of the ICP-SiNWs, their PL properties have been investigated in order to check the possible occurrence of light emission due to the QC effects which could arise in these Si nanostructures. Figure 16(a) shows a typical PL spectrum of the ICP-SiNWs following their excitation with a 405 nm laser beam at room temperature. This PL emission is intense and centered around 830 nm, with a full width at half maximum (FWHM) of ~185 nm. One can also notice that this broad PL spectrum is asymmetric and contains apparent shoulders, suggesting its deconvolution into different components. In fact, the PL spectrum can be fitted with three components having a FWHM of ~120 nm (this line width is close to that of ~100 nm which was reported for monodisperse silicon nanoparticles [Kang07]). Thus, the three PL components are located at ~685 nm, ~775 nm and ~855 nm, most presumably associated with light emission from electron-hole recombination into quantum confined Si nanostructures having the three different sizes and morphologies (cylindrical SiNWs, almond-shaped SiNCs and spherical SiNCs).

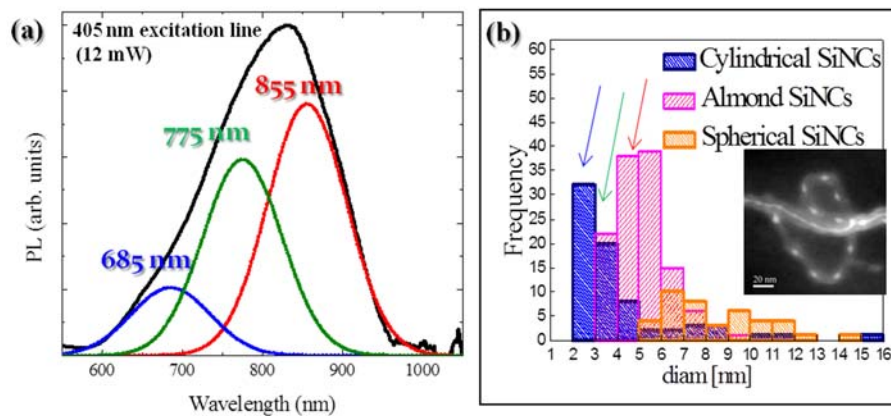


**Figure 4.16.** (a) Representative PL spectrum of the as-collected SiNWs as long as its deconvolution into three main components; (b) illustration of the diameter distributions related to the three different morphologies in the as-collected powder.

To facilitate the comparison, the superposition of the diameter distributions related to the three different morphologies in the as-collected sample (which have already been displayed separately in Fig. 5) is represented in Fig. 16(b). Firstly, 1D (the cylindrical SiNWs) and 0D (spherical and almond-shaped SiNCs) nanostructures have been distinguished in the attempt to correlate their mean size with the corresponding PL emission. It is worth pointing out that the

theoretically predicted bandgap behavior as a function of the diameter of cylindrical NWs has been elucidated by Zhao et al. [Zhao04]. The theoretical curve, shown with a continuous line in Fig. 17, predicts a bandgap of about 1.75 eV (~700 nm) for cylindrical SiNWs with ~2.7 nm-diameter, which correspond to the mean size evaluated for cylindrical ICP-SiNWs. The correlation between the measured value of SiNW mean diameter and the corresponding bandgap is indicated by the blue star in the graph in Fig. 17. Thus, it is possible to speculate that the high-energy component (around 685 nm) of the observed PL spectrum of Fig. 16 is due to the radiative recombination of electron-holes within the cylindrical SiNWs.

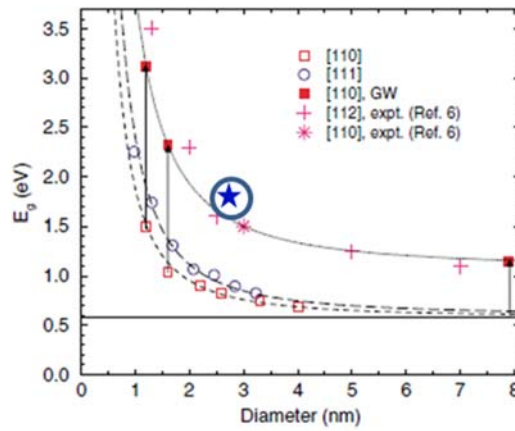


**Figure 4.17.** Theoretically predicted correlation between the size and the PL energy in SiNWs [Zhao04], whilst the blue star corresponds to the bandgap expected cylindrical ICP- SiNWs. having mean diameter ~ 2.7 nm.

On the other hand, in the case of 0D nanostructures calculations were performed by approximating the almond-shaped SiNCs to spherical SiNCs having the same diameter. Thus, the size of the silicon nanocrystals can be connected with their bandgap  $E_{PL}$  according to the following relationship [Ledoux00]:

$$E_{PL} = E_0 + \frac{3.73}{d^{1.39}} + \frac{0.881}{d} - 0.245 \quad (1)$$

where  $E_0$  is the bandgap of bulk Si ( $E_0 = 1.17 \text{ eV}$ ) and  $d$  is the SiNC diameter. This theoretical curve is plotted by the dotted line in Fig.18.

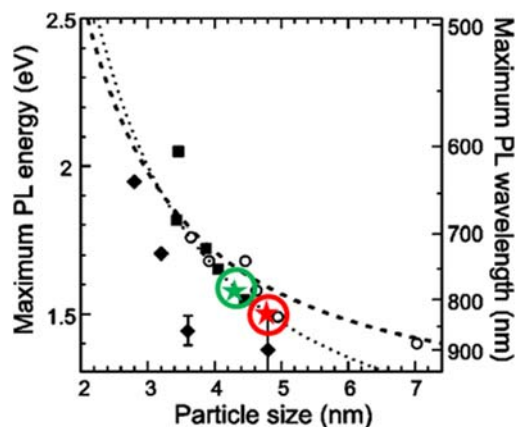


**Figure 4.18.** Theoretically predicted correlation between the size and the PL energy in SiNCs [Ledoux00], whilst the green and red stars correspond to the experimental value obtained for SiNCs having mean diameter  $\sim 3.2$  nm and  $3.8$  nm, respectively.

According to Eq. (1), the emission line at  $775$  nm ( $\sim 1.60$  eV) is expected for SiNCs having mean diameter  $\sim 4.2$  nm (green star in Fig. 18), while the low energy component located at  $855$  nm ( $1.45$  eV) corresponds to SiNCs mean diameter  $\sim 4.8$  nm (red star in Fig.18). Finally, it should be reminded that the mean diameter of the almond-shaped SiNCs composing the chapelet-like SiNWs is  $4.5 \pm 1.4$  nm and that of spherical SiNCs forming the chains is equal to  $7.0 \pm 2.7$  nm, as reported in Fig.5. Thus, the PL components at  $775$  nm and  $855$  nm are believed to be due to almond-shaped SiNCs having a mean diameter between  $4.2$  and  $4.8$  nm. Conversely, spherical SiNCs are not expected to contribute to the PL signal since their diameter ( $\geq 5$  nm) is larger than the exciton Bohr radius in Si ( $\sim 4.5$  nm) [Agati16].

#### 4.4. Conclusions

It has been demonstrated that ultra-thin SiNWs were produced by means of an high throughput (of the order of hundreds of grams per day) ICP based process. Two families of SiNWs have been identified, namely long SiNWs (up to  $2\text{-}3$  micron in length) and shorter ones ( $\sim 100$  nm). SiNWs were found to consist of a Si core (with diameter as thin as  $2$  nm) and a silica shell, of which the thickness varies from  $5$  to  $20$  nm. By combining advanced transmission electron microscopy (TEM) techniques, it has been demonstrated that the growth of the long SiNWs occurred via the Oxide Assisted Growth OAG mechanism, while the Vapor Liquid Solid mechanism is responsible for the growth of shorter ones. In addition, these ICP-SiNWs were

found to present an intriguing internal nanostructure made of cylindrical, chapelet-like and chain-like Si nanostructures, all embedded into an otherwise continuous silica nanocylinder. Such Si nanostructures provide a new kind of nanocomposite, where QC effects occur. Indeed, the room temperature PL studies confirmed the occurrence of QC in these Si nanostructures as they exhibited an intense and broad PL emission over all the visible-near infrared spectral range. In fact, three PL components have been isolated and associated with three different shapes and sizes of the ICP grown Si nanostructures.

All these studies have represented a solid basis towards the synthesis of SiNWs via ICP, thus more efforts have been put to design a procedure for the intentional synthesis of SiNWs via ICP. In this way, ICP-SiNWs were intentionally reproduced, providing a real perspective for large scale production of thin SiNWs by the ICP process. More insight of the new synthesis will be furnished as a future perspective of this work.

## Bibliography

[Agati16] M. Agati, G. Amiard, V. Le Borgne, P. Castrucci, R. Dolbec, M. De Crescenzi, M.A. El Khakani and S. Boninelli, *Sci. Rep.* 5, (2016).

[Agati16a] M. Agati, G. Amiard, V. Le Borgne, P. Castrucci, R. Dolbec, M. De Crescenzi, M.A. El Khakani and S. Boninelli, *Beilstein J. Nanotechnol.* 8, (2016).

[Guo95] J. Y. Guo, F. Gitzhofer and M.I. Boulos, *J. Mater. Sci.* 30, (1995).

[Guo10] J. Guo, F. Xiaobao, R. Dolbec, X. Siwen, J. Jurewicz and M. Boulos, *Plasma Sci. Technol.* 12, 2 (2010).

[Kang07] Z. Kang, C. H. A. Tsang, Z. Zhang, M. Zhang, N. Wong, J. A. Zapien, Y. Shan and S. T. Lee, *J. Am. Chem. Soc.* 129, 17 (2007).

[Ledoux00] G. Ledoux, O. Guillois, D. Porterat, C., Reynaud, F. Huisken, B. Kohn and V. Paillard, *Phys. Rev. B* 62, 23 (2000).

[Lee00] S. T. Lee, N. Wang and C. S. Lee, *Mater. Sci. Eng. A* 286, 1 (2000).

[Morales98] A. M. Morales and C. M. Lieber, *Science* 279, 5348 (1998).

[Peng01] H. Y. Peng, Z. W. Pan, L. Xu, X. H. Fan, N. Wang, C. S. Lee and S. T. Lee, *Adv. Mater.* 13, 5 (2001).

[Wang08] N. Wang, Y. Cai, and R. Q. Zhang, *Mater. Sci. Eng. R-60*, 1 (2008).

[Zhang00] Y.F. Zhang, Y.H. Tang, C. Lam, N. Wang, C.S. Lee, I. Bello, S.T. Lee, *J. Cryst. Growth* 212, 1 (2000).

[Zhang01] R.Q. Zhang, T.S. Chu, H.F. Cheung, N.Wang, S.T. Lee, *Phys. Rev. B* 64, 11 (2001).

[Zhang03] R-Q. Zhang, Y. Lifshitz and S-T. Lee, *Adv. Mater.* 15, 7-8 (2003).

[Zhang04] R.Q. Zhang, M.W. Zhao, S.T. Lee, *Phys. Rev. Lett.* 93, 9 (2004).

[Zhao04] X. Zhao, C. M.Weil, L. Yang and M.Y. Chou, *Phys. Rev. Lett.* 92, 23 (2004).

## **CHAPTER 5:**

### **SORTING PROTOCOL TO EXTRACT SINWS**

As it has been described in the previous chapter, the as-collected ICP powder contains both Si spheres and SiNWs, the sizes of the spheres ranging from 50 up to 500 nm, while the nanowires are 1-2  $\mu\text{m}$  long and have radius from few nm up to few tens of nm. The as-collected powder represents the by-product of the spheroidization process intended to produce Si microspheres, so the presence of spherical particles is not surprising. In the previous chapter the origin of the SiNWs has also been explained. Since the synthesis of ICP-SiNWs was not intentional, it resulted in such a mixture of Si nanostructures having a wide size distribution.

In this chapter it will be described a protocol developed to select the size of ICP Si nanostructures. Indeed, calculation of the Svedberg coefficient, which describes the behavior of particles (both Si spheres and SiNWs) subject to a centrifugal force, leads to propose a centrifugation process as a suitable procedure to select the size of ICP Si nanostructures. By changing the acceleration in the centrifugation process, a procedure has been identified to sort SiNWs with specific mean size. The efficacy of the purification effect, in terms of size selection, has been evaluated via PL as well as SEM measurements. PL spectroscopy allowed to associate any shift of the emission peak to the mean size of SiNWs via the QC effect. However, since Si spheres result massive to produce any PL emission in the visible range according to QC, SEM statistical analyses have been performed to evaluate the size distribution of the Si spheres resulting from the purification process. It has been confirmed that a centrifugation based protocol is effective to sort SiNWs and Si spheres with smaller mean size. Moreover, the presence of the more massive spheres decreases after centrifugation, thereby leading to conclude that a sample more purely composed of SiNWs can be obtained after centrifugation, which thus constitutes a purification procedure to extract SiNWs from the mixture of ICP Si nanostructures.

In the first paragraph of this chapter the definition of the Svedberg coefficient will be given as well as an estimation of this coefficient in the case of both Si spheres and SiNWs. Hence the centrifugation based experiments will be described. In the second paragraph, the PL spectra will be presented and their correlation with the size distribution of the SiNWs will show the size selection effect of the centrifugation process for SiNWs. Finally, the SEM analyses, which allow to evaluate the size distribution of the Si spheres, will be discussed in the fourth paragraph.

## 5.1. Purification process performed by centrifugation

In order to evaluate the possibility to achieve a selection of the size of the Si nanostructures, a study based on the different Svedberg coefficients of Si spheres and SiNWs has been made [LeBorgne]. Svedberg coefficient describes the sedimentation of particles with different mass and shape giving the rate at which a particle sediments under the action of the centrifugation force [Slonczewski09]. Hence, it depends on the mass, density and shape of a given particle, being expressed by the formula:

$$S = \frac{m}{6 \pi \eta r_0} \quad (1)$$

where  $m$  and  $r_0$  are the mass and the radius of the particle respectively, while  $\eta$  is the viscosity of the medium where the particle is dispersed. The sedimentation coefficient has the dimensions of a unit of time and corresponds to the time at which the particle sediments. As a result, the higher is the Svedberg coefficient the faster is the sedimentation process under the action of a force applied to a particle by gravity or by a centrifuge (measured typically in multiples of thousands of gravities in an ultracentrifuge). Since the mass can be expressed as  $m = \rho V$ , the formula (1) can also be written as:

$$S = \frac{\rho V}{6 \pi \eta r_0} \quad (2)$$

where  $\rho$  is the density of Si in our case. Given the volume of a spherical particle  $V_s$ :

$$V_s = \frac{4}{3} \pi R_s^3 \quad (3),$$

while the volume of the nanowires  $V_w$  being represented by the formula for a cylinder:

$$V_w = \pi R_w^2 L_w \quad (4)$$

the ratio between the Svedberg coefficients of a SiNW  $S_W$  and a Si sphere  $S_S$  can be calculated as:

$$\frac{S_S}{S_W} = \frac{V_S}{V_W} \cdot \frac{R_W}{R_S} \quad (5).$$

Considering as an example a sphere with radius  $R_s= 100$  nm and a wire with radius  $R_w=10$  nm and length  $L_w= 1.5$   $\mu\text{m}$ , the ratio between the Svedberg coefficients of both the spheres and nanowires can be evaluated after calculation of the volume of each particle.

Given the dimensions mentioned above, the Eq. (5) results to be

$$S_S = \frac{V_S}{V_W} \cdot \frac{R_W}{R_S} \cdot S_W \sim 90\% S_W \quad (6).$$

So, the different Svedberg coefficients of Si spheres and SiNWs are comparable, i.e. both nanostructures react to the centrifugation similarly. Moreover, it can be observed that, since the volume increases with the cube of the radius, the relation (5) depends on the square of the Si nanosphere radius. Thus, Si spheres with radius larger than 100 nm have higher Svedberg coefficients than wires and sediment more quickly. In conclusion, a centrifugation procedure appears suitable to select the size of both Si spheres and SiNWs when the radius of the Si spheres is less than 100 nm. Furthermore, when the Si spheres have a radius larger than 100 nm, the centrifugation has the effect of separating the SiNWs from the more massive Si spheres.

To confirm these assumptions, centrifugation-based experiments have been performed by varying the centrifugation force. To this aim, solutions with well-defined concentrations (0.5mg/ml) have been prepared and centrifuged for 1 hour at acceleration values ranging from 1'000 g to 20'000 g, where g is the gravity constant. Figure 1 illustrates the solution formed by dispersion of the as collected sample and the solution after centrifugation at 1.000 g, 5.000 g and 15.000 g.

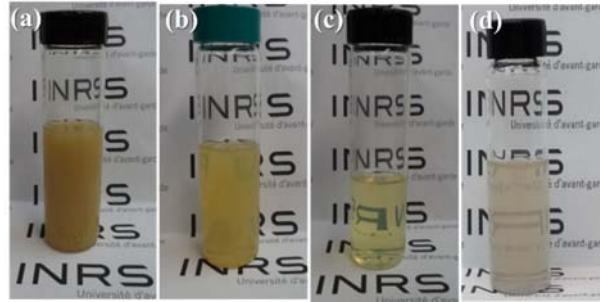


**Figure 5.1.** Comparison of solutions (a) before centrifugation and after centrifugation at (b) 1.000 g, (c) 5.000 g and (d) 15.000 g.

It can be noticed that the color of the solution depicted in Fig. 1(a) is brown and more opaque than the solutions illustrated on the right, which become progressively light yellow and translucent [Fig. 1(b and c)], then changing again into a slightly opaque solution [Fig. 1(d)]. Since we expect that at higher centrifugation force the more massive particles are removed, the change of color and transparency of the solutions seems to be related to the composition of the samples, indicating a more pure composition in the sample shown in Fig 1(c) in terms of the presence of bigger particles. However, a more quantitative description of the effectiveness of centrifugation processes is required to confirm any qualitative hypothesis on the composition of the samples. For this reason, PL measurements as well as SEM investigation have been made, as described in the following two paragraphs.

## 5.2. Photoluminescence tuning by size selection

Since the optical emission of SiNWs is related to their mean size, PL spectroscopy offers a tool to evaluate the efficacy of the different centrifugation procedures, where the blue-shift of the PL peak is related to the sorting of thinner SiNWs. Thus, PL measurements have been performed on samples centrifuged at different centrifugation forces. To this aim, the samples in solution have been deposited onto quartz by a spray coating method in order to obtain films made of ICP-Si nanostructures with uniform thickness [LeBorgne]. The substrates were heated at temperature of 80°C to lead to the evaporation of the alcohol. The PL measurements were performed with a 405 nm (12 mW) solid state laser excitation line. The emitted light was collected through an optical fiber into a USB5000 Ocean optics CCD spectrometer, with a 405 nm notch filter placed between the laser and the sample as well as a 475 nm long pass filter

placed between the sample and the spectrometer. All PL spectra were corrected for the system response curve.

The normalized PL spectra at different centrifugation forces, namely 1.000 g, 2.500 g, 5.000 g, 10.000 g, are shown in Fig. 2. With this method, the as-collected material results to have a very intense and broad infrared PL response that is peaked at 900 nm and extends from 750 nm to 1100 nm. Then, a progressive blue-shift has been evidenced for sample centrifuged at 1.000 g, 2.500 g, 5.000 g. Finally, at the highest centrifugation force (10.000 g) the PL is far less intense and shifted back to the near infrared. In particular, the sample centrifuged at 5.000 g has a PL emission, extending from 600 nm to 950 nm and peaked at ~820 nm, with a narrow FWHM (~180 nm) compared to the other spectra. As it has been shown on the previous chapter, the PL emission of the as-collected sample is related to the size distribution of SiNWs and SiNCs which constitute the inner Si core of the NWs in the frame of QC effect. The blue-shift of the PL peak with respect to the as-collected sample thus indicates removal of larger SiNWs, which is an indication of the size-sorting effect achieved via the centrifugation.

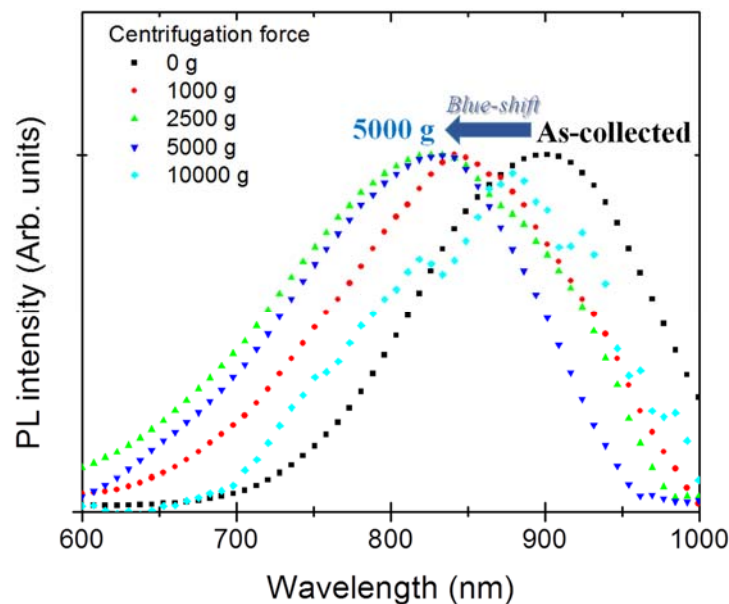


**Figure 5.2.** Normalized PL spectra of the as-collected sample and of samples centrifuged at different accelerations: 1'000 g, 2'500 g, 5'000 g and 10'000 g.

Nevertheless, the PL emission seems to show that the size distribution at higher centrifugation forces once again includes larger structures, as it can be seen in the spectrum

related to the sample centrifuged at 10.000 g, in Fig. 2. It is highly likely that for acceleration values  $\geq 10.000$  g SiNWs and Si spheres are affected by the same sedimentation rate and cannot be separated at such high centrifugation force, i.e. there is no difference in the behaviour of SiNWs and Si spheres in a centrifugation process [LeBorgne].

In conclusion, PL measurements have been demonstrated as a suitable tool to evaluate the efficacy of the centrifugation process in terms of the size-selection of the SiNWs. Indeed, on the light of the QC model, the blue-shift of the PL peaks observed up to acceleration of 5.000 g demonstrates that a partial selection of SiNW diameters can be achieved by means of centrifugation procedures, whereas smaller diameter SiNWs are present in the sample centrifuged at 5.000 g. Conversely, the mean diameters of SiNWs present in the samples centrifuged at both lower and higher acceleration result to be larger, confirming that 5.000 g is the optimal value for the sorting of thinner SiNWs.

### **5.3. Evaluation of the purification efficacy by SEM**

In order to quantitatively evaluate the action of centrifugation in terms of removal of the massive Si spheres, SEM analyses were also conducted. To this purpose, after centrifugation, the supernatant was deposited onto Si substrates in order to form a monolayer of Si nanostructures and thus distinguish SiNWs from Si spheres in the SEM images. Hence, a systematic study has been accomplished to evaluate both the percentage of residual Si spheres and their mean diameter. Statistical analyses have been performed on tens of SEM images of the same sample, by collecting several hundred of nanostructures. The images were analysed by means of the ImageJ software to evaluate the ratio between the area covered by the Si spheres and the whole area covered by both SiNWs and spheres. This ratio has been considered as a parameter to evaluate the percentage of spherical structures present in the sample before and after purification. In addition, the mean radius of the spherical structures present in the various samples has also been measured.

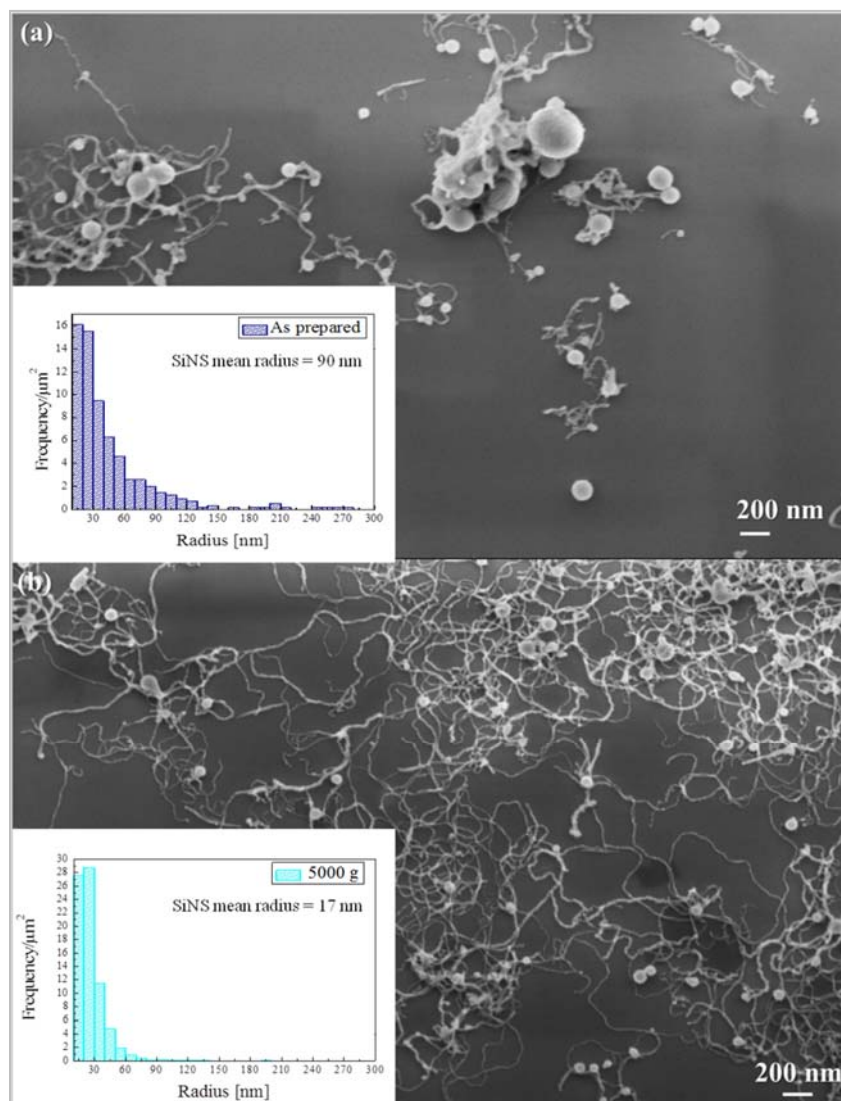


**Figure 5.3.** Typical SEM image depicting (a) the as-collected sample and (b) the sample centrifuged at 5.000 g. In the inset, the corresponding Si spheres size distributions are also shown.

Since PL studies suggested the centrifugation at 5.000 g as the optimum to achieve the size selection of the thinner SiNWs, the sample centrifuged at 5.000 g will be focused hereafter, in order to estimate its purity in terms of the presence of the most massive Si spheres. Figure 3 shows a comparison between the SEM images of the as collected powder and the one purified at 5.000g. In the inset the corresponding Si sphere size distributions have been also illustrated. It can be seen that there are some Si spheres with size of the order of hundreds of nm in the as-collected sample [Fig. 3(a)]. For this sample, the Si spheres mean radius results to be  $\sim 90$  nm, while the percentage of Si spheres with respect to the total amount of nanomaterial is  $\sim 78\%$ . By

increasing the centrifugation forces up to 5.000 g, it turns out that not only the percentage of Si spheres decreases, but also their average dimension results to be smaller. In Figure 3(b) it has been illustrated a typical SEM image of the sample centrifuged at 5.000 g as well as the result of the statistical analysis. The mean radius of the spheres decreases significantly in this sample, being equal to ~17 nm, while the ratio between the area covered by the spherical structures and the area covered by both SiNWs and spheres is ~15%. By comparing the histograms in the insets Fig. 3(a) and 3(b) it can be noted that after centrifugation at 5.000 g the biggest Si spheres with size of the order of hundreds nm have been removed, leaving just SiNSs having sizes of few tens of nm. It is thus possible to conclude that the centrifugation procedure acts also as a purification process, whereas the most massive Si particles are removed and a sample more purely composed of SiNWs can be obtained, as it can be also inferred by comparison of the SEM images reported in Fig. 3. A centrifugation protocol performed at acceleration equal to 5.000 g results to be the optimal method, since it allows to achieve a more pure sample not only in terms of the presence of the Si spheres, which result to decrease in number, but also the largest and most massive particles are removed leaving Si spheres with mean radius of few tens of nm.

## 5.4. Conclusions

In conclusion, in this chapter it has been demonstrated the suitability of a centrifugation based process to select the size of ICP Si nanostructures with otherwise larger size distribution. Calculations based on the Svedberg coefficients of both SiNWs and Si spheres led to propose a centrifugation procedure as a suitable tool to select the size of SiNWs and Si spheres. Moreover, the removal of the Si spheres having larger diameter (>100 nm) is expected. These hypotheses were confirmed by performing different centrifugation processes by varying the centrifugation forces. The centrifugation selects the mean size of the SiNWs extracted from the ICP-samples, as inferred from PL results. Furthermore, SEM studies allow to evaluate both the presence of the spherical particles and their mean size. In this way, centrifugation processes have been also identified as a purification protocol to sort the SiNWs from the by-product of the ICP system, separating the SiNWs from the most massive Si spheres remaining from the spheroidization. A procedure effectuated at 5.000 g results to be the optimal strategy to achieve a sample more purely composed of ultra-thin SiNWs, as demonstrated by combining both PL results and SEM imaging.

## **Bibliography**

[Kang07] Z. Kang, C. H. A. Tsang, Z. Zhang, M. Zhang, N. Wong, J. A. Zapien, Y. Shan and S. T. Lee, *J. Am. Chem. Soc.* 129, 17 (2007).

[LeBorge] V. Le Borgne, M. Agati, S. Boninelli, P. Castrucci, M. De Crescenzi, R. Dolbec, M. A. El Khakani, *Nanotechnology* 28, (2017).

[Slonczewski09] J. L. Slonczewski and J. W. Foster, *Microbiology: An Evolving Science*, WW Norton & Company (2009).

## CHAPTER 6: THERMAL TREATMENT TO FORM SI NANOCOMPOSITES VIA RAYLEIGH INSTABILITY

Once inferred the growth mechanisms of the SiNWs formed via the ICP technique, the presence of the three different morphologies of the Si inner core has yet to be explained. As described in the fourth chapter, the Si core of the ICP-SiNWs grown via OAG mechanism displays three different configurations, namely cylindrical as well as chapelet-like SiNWs and SiNC chains, enveloped in a silica shell. These nanostructures constitute a novel and intriguing kind of Si-based nanocomposite, whose high intrinsic degree of structural order deserves to be studied in detail. Indeed, in self-assembled nanostructures a such high level of structural control at the nanoscale is often difficult to achieve.

Similar chain-like nanostructures have already been observed and three possible mechanisms of formation were individuated:

- (1) periodic change of temperature or pressure during the synthesis, resulting in the change of the diameters of the Si nanowires [Zhang98, Peng01];
- (2) renucleation of the nanowire during growth [Wang98];
- (3) spheroidization of SiNWs due to a high-temperature induced instability, known as Rayleigh instability phenomenon [Peng01].

Nonetheless, it has been demonstrated that the phenomenon (1) occurs for metal catalyzed growth [Zhang98], while the diameters of SiNWs grown via OAG are not sensitive to the pressure [Peng01]. The mechanism (2) has been observed only for relatively short nanoparticle chains [Lee99], while in our case  $\mu\text{m}$ -long SiNWs have been found. Thus, in order to understand if the third mechanism is at the basis of the three different morphologies of the inner Si core of ICP-SiNWs, their thermal stability has been studied. To this aim, thermal annealing have been performed in-situ within a TEM, allowing to observe real time the structural evolution of the Si core. Furthermore, ex-situ annealing in furnace have also been performed and the samples have been examined by statistical EFTEM analyses.

The study of the thermal stability of ICP-SiNWs will be presented in the first paragraph of this chapter, while the interpretation of the results of both in-situ and ex-situ analyses will be discussed in the second paragraph of this chapter, where also the mechanism of formation of the three different configurations of the ICP-SiNWs will be elucidated.

## 6.1. Study of the thermal stability of SiNWs

### 6.1.a In situ TEM analyses

In order to investigate the thermal stability of ICP-SiNWs, in-situ TEM analyses have been firstly performed. The sample was prepared by dropcasting the solution of the as-collected ICP-SiNW powder on  $\text{Si}_3\text{N}_4$  TEM grid, which is resistant up to  $1000^\circ\text{C}$ . The analyses were performed in EFTEM mode at 17 eV, i.e. the Si plasmon energy loss, by heating the sample via a smart heater control from room temperature up to  $990^\circ\text{C}$ . The temperature was increased at steps of  $200^\circ\text{C}$  each  $\sim 5$  minutes up to  $900^\circ\text{C}$ , then at steps of  $15^\circ\text{C}$  each 4 minutes up to  $990^\circ\text{C}$ . Then, the temperature was maintained fixed for about 1 hour. Focus was put in different regions of the sample in order to observe any structural change induced by the heating during the time.

Figure 1(a) represents an EFTEM image depicting a cylindrical SiNW, as indicated by the red arrow, that emerges from a SiNS at the beginning of our observation ( $t=0$ , room temperature). The diameter of the SiNW is about 3 nm. The EFTEM image reported in Fig. 1(b) shows the same SiNW after  $\sim 1$  hour and 45 min, when the temperature reached  $990^\circ\text{C}$ . It can be noted that the Si core becomes thinner and breaks at periodic points, as indicated by the red arrows. The fragments composing the SiNW result thicker, being  $\sim 4$  nm, most likely owing to the Si diffusion from the breakpoints where the wire splits.

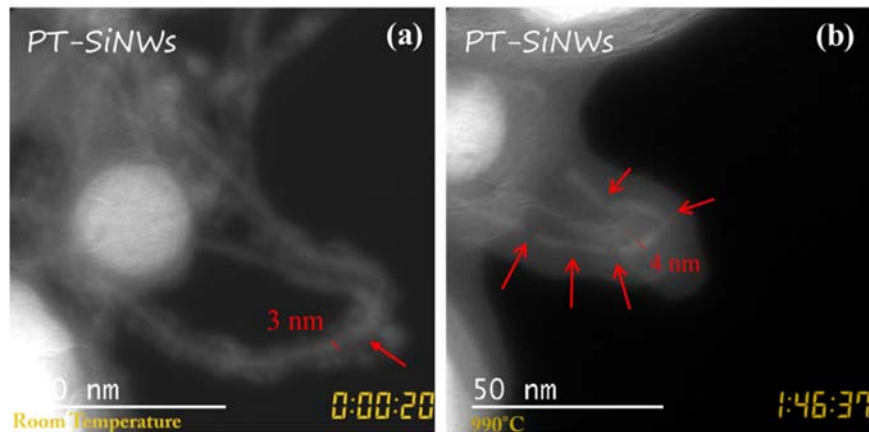


**Figure 6.1.** EFTEM images of (a) a cylindrical SiNW at  $t=0$  and (b) the same SiNW after  $\sim 1$  hour and 45 min: it can be seen that the SiNW broke up into Si crystalline fragments.

In Figure 2(a) it has been reported an EFTEM image illustrating another region of the sample at  $\sim 940^\circ\text{C}$  after  $\sim 30$  minutes of annealing. It depicts a chapelet-like nanostructure with

almond-shaped SiNCs having diameter of about  $\sim 5$  nm. It is also possible to note the presence of residuals of the thin wire connecting the SiNCs. Nonetheless, after  $\sim 1$  hour, when the temperature reached  $990^\circ\text{C}$ , there are no traces of the Si wire between adjacent SiNCs, which result to have a slightly larger diameter ( $\sim 6$  nm), thus approaching the SiNC chain configuration as can be seen in Fig. 2(b). Also in this case, the slight enlargement of the SiNCs can be attributed to the diffusion of Si composing the thin wire which connects two nearby SiNCs. Hence, the observation of the structural changes of the Si inner core in the SiNWs during the annealing treatment is a clear indication of the role played by the temperature in the morphological evolution of these Si nanostructures.

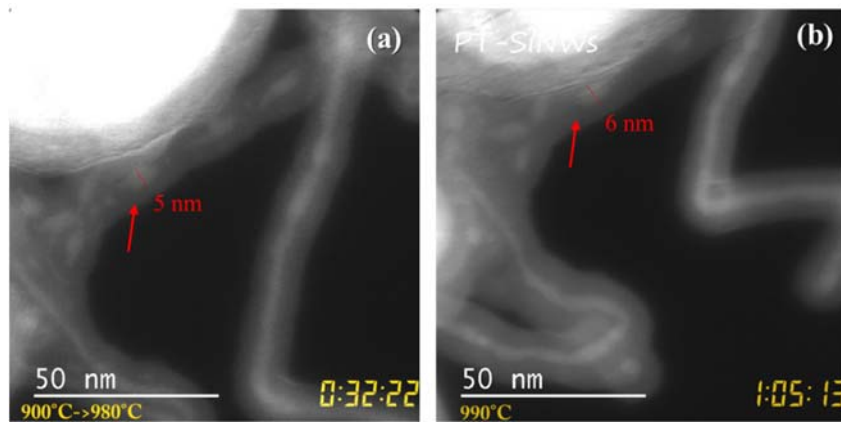


**Figure 6.210.** (a) EFTEM image of a chapelet-like SiNW subject to in-situ thermal annealing after  $\sim 30$  minutes; (b) the same nanostructures after almost 1 hour show an evolution towards a SiNC chain morphologies.

It is worthy to note that the structural transitions, as those observed in Figs. 1 and 2, initiate at temperature higher than  $900^\circ\text{C}$ . At such high temperature conditions the Si core is most likely in semi-liquid phase, being the melting point of Si nanostructures much lower than in bulk Si [Safaei10], thus the evolution of the otherwise stable Si nanostructures is favored. Hence, the breaking of the SiNW core displayed in Fig. 1 most likely indicates the structural transition from cylindrical core towards almond-shaped SiNC forming the chapelet-like configuration. On the other hand, in Fig. 2 it can be observed the evolution from almond-shaped SiNCs, still connected by a thin wire, towards separated and spherical SiNCs. It is possible to note that the transformation from cylindrical SiNW towards the chapelet-like is slower, becoming apparent after almost 2 hours [Fig 1(b)], while the transition from almond shaped to spherical SiNCs is revealed after  $\sim 30$  minutes.

In conclusion, in situ TEM analyses gave further insights on the structural evolution of ICP-SiNWs under thermal treatment, supporting the assumption about the occurrence of a

temperature-driven instability. Nevertheless, it is highly likely that the thermal budget is not enough high to further induce significant morphological changes in this time scales. Being 990 °C the highest temperature reachable inside our TEM, we could not go further with the in-situ annealing. For this reason ex-situ thermal treatments at higher temperatures have been performed in conventional furnace, as described in the next section.

### **6.1.b Ex-situ analyses**

Ex-situ analyses have been performed by annealing the as-collected powder in a horizontal furnace for 1 hour in N<sub>2</sub> environment, where the N<sub>2</sub> flux was set at 5 liters per minute. The powders have been annealed separately at 800°C, 1000°C and 1200°C. After the thermal treatments, the powders have been dissolved in isopropyl alcohol and sonicated for 5 minutes, then the solution has been dropcasted on carbon lacy TEM grids to perform TEM analyses. Hence EFTEM studies have been conducted on each of the three annealed samples at 17 eV, by examining hundreds of Si nanostructures in order to evaluate the occurrence of the three different configurations as a function of the temperature. Figures 3(b, c and d) illustrate three representative EFTEM images of the samples annealed at 800°C, 1000°C and 1200°C. For comparison, the as collected sample has also been shown in Fig. 3(a). We can see that in both the as collected and in the samples annealed at 800°C and 1000°C, respectively shown in Figs. 3(a, b and c), both chapelet-like and chain nanostructures are visible as well as continuous cylindrical Si cores. Nevertheless, in the sample annealed at 1200°C, spherical SiNC chains appear to be predominant, as it is illustrated in Fig. 3(d).

In order to quantitatively estimate the presence of the three different morphologies in each sample, statistical EFTEM investigations have been performed. The results are reported in Fig. 3(e, f, g and h) for the as collected as well as for the annealed ICP-SiNWs. As already mentioned in the fourth chapter, the cylindrical SiNWs constitute the major component of the as collected sample, being the 53% of the SiNW population, while the percentage of the chapelet-like nanostructures is equal to the 36% and the SiNC chains represent only the 11% of the total amount of ICP-SiNWs [see Fig. 3(e) in the fourth chapter].

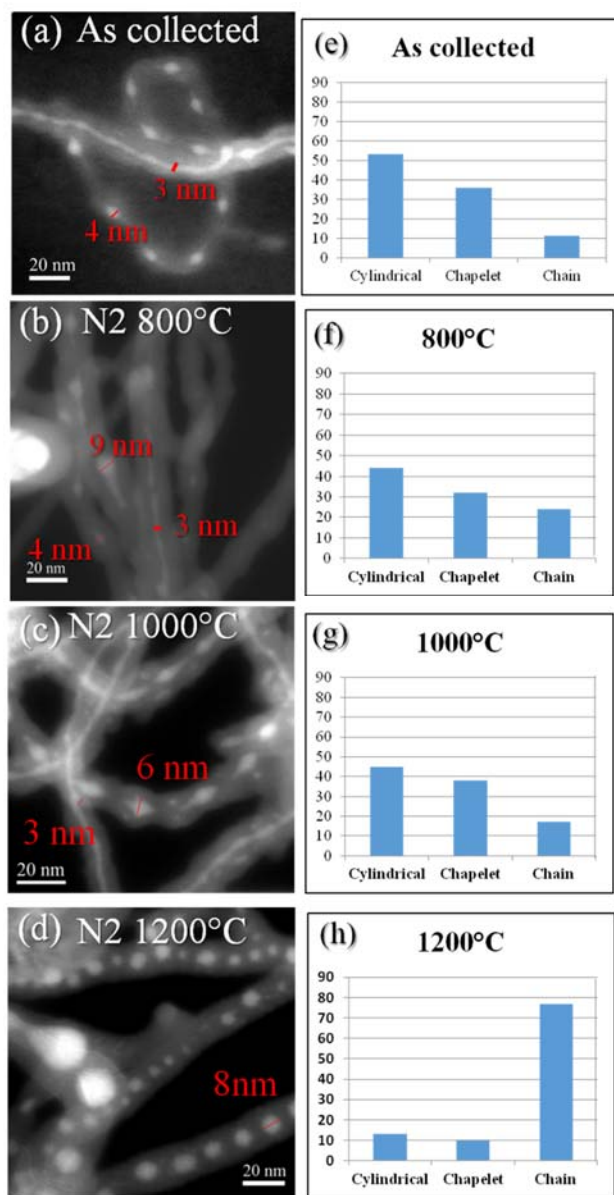


**Figure 6.3.** EFTEM images of (a) the as-collected sample and the samples annealed at (b) 800°C, (c) 1000°C and (d) 1200°C in N<sub>2</sub> for 1 hour. (e-h) Corresponding statistical distribution of the occurrence of the three different SiNW morphologies.

The percentage of both cylindrical and almond-shaped SiNWs decreases in the samples annealed at 800°C and 1000°C with respect to the as-collected sample, being ~44% and 45% respectively. It is evident that there is a progressive decreasing of the number of cylindrical SiNWs in favor of the SiNC chains (~20% in the samples annealed at 800°C and 1000°C), as it can be observed in Figs. 3(f) and (g). The SiNC chain configuration clearly prevails in the sample annealed at 1200°C, being ~80% of the whole SiNW population [Fig. 3(h)], while the

cylindrical SiNWs represent the ~10% and the chapelet-like nanostructures correspond to the ~10%. Hence, it is evident that the thermal treatment induces a structural evolution of cylindrical morphologies towards SiNC chains, being the chapelet-like configuration a sort of intermediate configuration. Such a structural transformation is accelerated at higher temperatures, as demonstrated by the preponderance of SiNC chains at 1200°C.

Furthermore, the statistical distributions of the diameters of Si cylinders, almond-shaped SiNCs and spherical SiNCs have been evaluated for each sample (Fig. 4). It can be seen that the cylinder mean size increases from ~2 nm after annealing at 800°C and 1000°C up to 7 nm in the sample annealed at 1200°C. Moreover, the almond-shaped SiNC diameters evolve from ~4 nm after annealing at 800°C and 1000°C up to 6 nm in the sample annealed at 1200°C. The spherical SiNCs also have larger diameter in the sample annealed at 1200°C, being about 7 nm, while this value is reduced at ~5 nm in the samples annealed at lower temperatures.

Hence, summarizing the results of the statistical analyses displayed in Figs. 3 and 4, it can be inferred that the thermal treatment favors the transformation of those cylindrical SiNWs having smaller diameters towards chapelet-like SiNWs and, finally, spherical SiNCs. The final configuration has larger dimension than the initial Si cylinder, suggesting that Si diffuses and accumulates in periodic points where the spherical SiNCs take shape. In the sample annealed at 1200°C large cylindrical and chapelet SiNWs remain stable, indicating that their structural evolution requires higher thermal budgets.

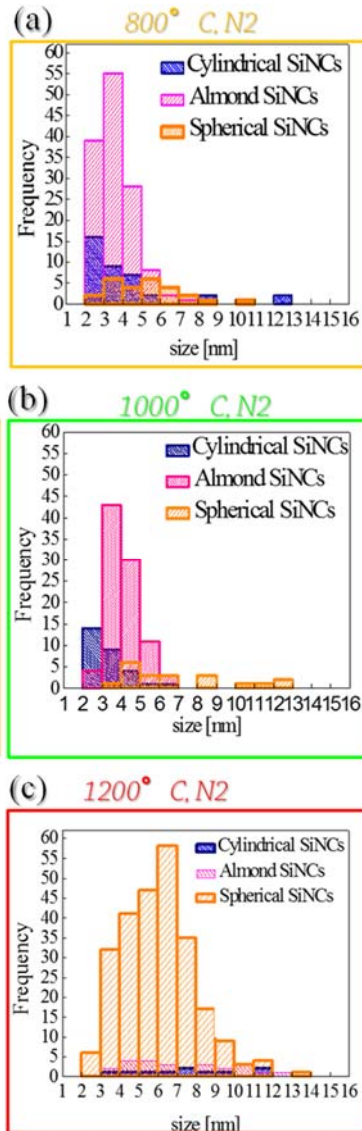


**Figure 6.4.** Size distributions of the diameters of Si cylinders (blue color), almond-shaped SiNCs (magenta color) and spherical SiNCs (orange color) in the samples annealed at: (a) 800°C, (b) 1000°C, (c) 1200°C.

## 6.2. Rayleigh instability

The results concerning the investigation of the thermal stability of ICP-SiNWs support the hypothesis that a thermally driven instability, indicated as Rayleigh instability [Peng01], induces the structural transformation of ICP-SiNW. Rayleigh theory predicts the morphological transformation of cylindrical fluids after their shape becomes unstable under the influence of surface tension at elevated temperatures [Rayleigh78]. As a result, the cylinder breaks up into

regularly-spaced spheres with the same diameter, where both the distance between the spheres and their size obey to a mathematical model. Lord Rayleigh prosecuted Plateau's studies on liquid cylinders [Plateau63], where Plateau had already demonstrated that a cylindrical liquid structure with radius  $r$  is unstable against sinusoidal perturbations having wavelength  $\lambda$  greater than the circumference of the initial cylinder. Such instability induces the fragmentation of the cylinder into spherical drops, driven by the minimization of the total surface energy. Lord Rayleigh concluded that the interdistance  $\lambda$  between the droplets and their radius  $R$  is described by the formula  $\lambda/R = \text{constant}$  [Rayleigh78]. The theoretical constant can be estimated by assuming  $\lambda = 9.02 R$ , as in the case of internal volume diffusion [Peng01], and  $\langle D \rangle = 3.78R$  as mean diameter  $\langle D \rangle$  of dewetted particles [Frantz03]. Hence, the theoretical ratio  $\lambda/R$  results to be equal to  $\sim 4.8$ .

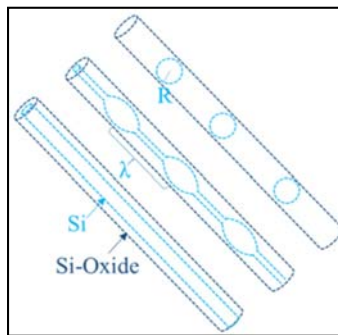


**Fig. 5.** The three different stages of Rayleigh instability occurring in SiNWs [Peng01].

The occurrence of Rayleigh instability in nanostructures has been studied in previous works [Kolb05, Qin08, Rauber12], indicating that the temperature to induce Rayleigh instability is related to the diameter of the cylinder: the phenomenon occurs at higher temperature for larger NW diameters. So, it could be inferred that Rayleigh instability drove the structural transformation of ICP-SiNWs towards the modulated Si core featuring the chapelet-like SiNWs, finally leading to the SiNC chain and the temperature at which the phenomenon is observed is higher for larger SiNWs, as illustrated in Fig. 5.

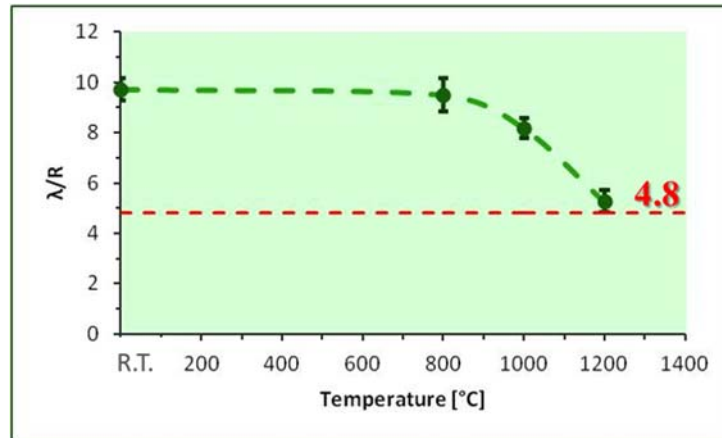


**Figure 6.6.** Graph showing the trend of the ratio  $\lambda/R$  in samples annealed at different temperatures; at 1200°C, the value of  $\lambda/R$  is in agreement with the theoretical value of 4.8, represented by the red line.

In order to definitely assert that the annealing induced the Rayleigh instability in ICP-SiNWs, the theoretical value predicted by Rayleigh model should be compared with the experimental ratio  $\lambda/R$  characteristic of ICP-SiNWs. To calculate the ratio  $\lambda/R$ , the diameters of ~100 SiNCs (both almond-shaped and spherical) and the distance between them have been measured in the EFTEM images. The results of this analysis are represented in the graph in Fig. 6. It is worth noting that the  $\lambda/R$  value obtained for as collected NWs and after 800°C is ~ 10, clearly confirming that the transition was not still activated at low temperature, while it is progressively approaching the theoretical value at 1000°C. Finally, we can observe that this ratio is equal to 5.2 at 1200°C, indicating that the complete structural transformation is driven by the Rayleigh instability where the theoretical expectation of  $\lambda/R=4.8$  is reached within the statistical error ( $\sigma =0.4$ ).

In conclusion, these results definitely confirm that the annealing treatments induce a progressive thermal instability from 800°C up to 1000°C, while the complete structural transformation driven by the Rayleigh instability can be observed at 1200°C.

### 6.3. Conclusions

The mechanism driving the structural transformation of ICP-SiNWs has been individuated, being due to the Rayleigh instability phenomenon induced by thermal treatments. Because of the Rayleigh instability, ICP-SiNWs evolve from the cylindrical shape towards a configuration of SiNC chains, whereas the chapelet-like configuration represents the

intermediate stage of the transformation. Such structural transformation is completed at 1200°C, leading to a mean size distribution of the three different morphologies which is larger than at lower temperatures and where the SiNC chains constitute almost the total amount of the Si nanostructures. This has been demonstrated via both in-situ analyses and ex-situ EFTEM analyses. This study allows to explain the presence of the three configurations also in the as collected ICP-SiNWs. This is believed to result from Rayleigh instability due to rapid post-synthesis heating of the SiNWs before their cooling down in the final part of the reactor.

Such Si nanostructures provide a new kind of nanocomposite formed via the self-assembly of Si crystalline nanostructures. Rayleigh instability, induced by post-synthesis thermal treatments, allows to produce structures characterized by a high level of structural order at the nanoscale, where a well-determined ratio between the diameters of the SiNC and their inter-distance could be handle by the opportune setting of the annealing process.

## Bibliography

[Frantz03] E. Frantzeskakis: 'Analysis of the potential applications for the template dewetting of metal thin films', Dipl. Eng. Mining Engineering and Metallurgy, National Technical University of Athens (2003).

[Kolb05] F.M. Kolb, H. Hofmeister, M. Zacharias and U. Gösele, *Appl. Phys. A* 80, 7 (2005).

[Lee99] S. T. Lee, Y. F. Zhang, N. Wang, Y. H. Tang, I. Bello, and C. S. Lee, *J. Mater. Res.* 14, 12 (1999).

[Plateau63] Plateau, J. *Transl. Annual Reports of the Smithsonian Institution*, 1873, p. 1863.

[Peng01] H. Y. Peng, N. Wang, W. S. Shi, Y. F. Zhang, C. S. Lee, and S. T. Lee, *J. Appl. Phys.* 89, 1 (2001).

[Rauber12] M. Rauber, F. Muench, M. E. Toimil-Molaes and W. Ensinger, *Nanotechnology* 23, 47 (2012).

[Rayleigh78] Rayleigh, L. *Proc. London Math. Soc.* 10, 4 (1878).

[Safaei10] A. Safaei and M. Attarian Shandiz, *Phys. Chem. Chem. Phys.* 12, 47 (2010).

[Wang98] N. Wang, Y. H. Tang, Y. F. Zhang, C. S. Lee, and S. T. Lee, *Phys. Rev. B* 58, 24 (1998).

[Qin08] Y. Qin , S.-M. Lee , A. Pan , U. Gösele and M. Knez, *Nano Lett.* 8, 1 (2008).

[Zhang98] H. Z. Zhang, D. P. Yu, Y. Ding, Z. G. Bai, Q. L. Hang, and S. Q. Feng, Appl. Phys. Lett. 73, 23 (1998).

## **CHAPTER 7:**

### **Conclusions and perspectives**

#### **7.1. Conclusions**

SiNWs synthesized via the ICP technique have been investigated thoroughly and the results concerning the study of their nanostructural and optoelectronic properties as well as their thermal stability have been presented and discussed in this PhD project. ICP technique emerges as a novel approach to produce SiNWs in the panorama of the methods currently employed for SiNW synthesis, which have been discussed in chapter 2. ICP was commonly exploited as a well-established procedure to fabricate micro and nanopowders at industrial scale through a spheroidization mechanism of a rough powder feedstock, so the use of ICP technique for the bulk-synthesis of SiNWs deserves to be examined, potentially constituting an innovative route to produce SiNWs.

ICP-SiNWs have been observed for the first time as constituent of the by-product of a Si micropowder synthesis process. More precisely, SEM imaging shows the presence of an ensemble of filamentary nanostructures as well as spherical particles derived from the spheroidization process at the basis of ICP micropowder synthesis. The most massive particles can be eventually eliminated via a purification procedure performed by means of centrifugations in order to obtain a sample more purely composed of SiNWs. It has been demonstrated that centrifugation represents also a good strategy to sort ultra-thin SiNWs by selecting the diameter of both Si spheres and SiNWs.

However, in a process optimized for the assembly of spherical particles the mechanism of SiNW formation was yet to be explained. To this purpose, an approach based on the employment of TEM-based techniques has been used to accomplish the investigation of SiNW structural and chemical characteristics and thus infer their growth mechanism. The synergetic use of EFTEM, HRTEM, electron tomography and STEM-EDX are at the basis of the main conclusions concerning ICP-SiNWs and presented here. The TEM based investigations revealed that the vast majority (~95%) of the ICP produced SiNWs grew according to the OAG mechanism, as no catalyst was intentionally introduced in the feedstock. Indeed, these OAG

grown SiNWs were found to grow directly onto larger SiNSs and have diameters of ~ 2-15 nm and lengths as long as 2  $\mu\text{m}$ . Some of these OAG synthesized SiNWs were found to present an intriguing internal nanostructure, made of chapelet-like Si nanocrystals, eventually connected by an extremely thin SiNW and embedded into an otherwise continuous silica nanocylinder. This is believed to result from Rayleigh instability due to rapid post-synthesis heating of the SiNWs before their cooling down in the final part of the ICP reactor.

Such Si nanostructures provide a new kind of nanocomposite, where the cylindrical cores, the chapelet-like nanostructures and the SiNC chains represent the three stages of a structural evolution predictable by the Rayleigh model. Our investigations also demonstrated that the VLS growth is also possible in the ICP synthesis, given that an appropriate catalyst is used along with the silicon feedstock. In fact, with some Fe impurities present inside the ICP reaction zone, we have found that almost 5% of the SiNWs grew through the VLS mechanism. These VLS-grown SiNWs exhibited different characteristics, as they are shorter (no longer than 150 nm), grow from the Si core of the larger SiNSs and present a Fe-rich nanoparticle at their tip. We conclude that the formation of SiNSs is mainly due to the spheroidization process inside the plasma chamber, while the SiNWs can grow according to both the OAG and VLS mechanisms (with a predominance of the OAG mechanism if no intentional metal catalyst is added).

The optoelectronic properties of the as-collected sample have also been probed by means of PL spectroscopy and correlated with the nanostructural characteristics of the ICP-SiNWs, assessing the occurrence of QC effect in the ICP-SiNWs. Indeed, our PL studies confirmed the occurrence of QC in these Si nanostructures as they exhibited an intense and broad PL emission over all the 620-950 nm spectral range. The PL curve has been deconvolved into three components, which have been associated with three different shapes and sizes of the ICP grown Si nanostructures.

In a second step of this project, the effect of post-synthesis thermal treatments on the nanostructural changes of these SiNWs has been studied. In this way, by exploiting the Rayleigh instability already noticed in the as-collected ICP-SiNWs, the structural transformation of the SiNWs into SiNC chains has been induced via thermal annealing in  $\text{N}_2$ . Such structural transformation is completed at 1200°C, emerging as a procedure to induce the self-assembly of Si crystalline nanostructures with a high level of order at the nanometric scale.

All these results constitute a solid basis towards the production of SiNWs via the ICP technique, where the content and nature of the catalyst can be controlled. The ICP is a genuinely bulk process, which can be advantageously exploited for large scale fabrication of thin SiNWs needed to integrate Si into attractive large-area optoelectronic devices and flexible

electronics. For this reason, a better-controlled procedure for the intentional synthesis of SiNWs via ICP technique has been designed. Preliminary results concerning this aspect will be presented in the following paragraph as a demonstration of the feasibility of SiNWs synthesis via ICP.

## **7.2. Perspectives: exploitation of a novel ICP process**

Once the growth mechanisms beyond the SiNW formation in ICP system has been understood, further efforts have been put in the optimization of an ICP-based process for the intentional synthesis of SiNWs. Two main routes can be identified, the former aiming to produce SiNWs mainly via OAG, the latter being intended to the synthesis of SiNWs via VLS (by intentionally adding a metal catalyst in the feedstock). Unlike the previous process, where the as-prepared powders were produced in the reactor designed for the spheroidization, for this synthesis an ICP reactor commonly exploited for nanopowder synthesis has been used. As described in chapter 3, the main difference between the apparatus for nanopowder production and for the spheroidization process relies in the presence of the quenching zone, which allows to control the cooling rate and thus the temperature gradient during the in-flight nucleation of the nanostructures. Different parameters have been changed in order to find the conditions to reproduce the ICP-SiNWs. It is possible to distinguish two main directions: the former concerning the most suitable plasma environment for SiNWs synthesis, whereas in the latter focus has been put on the Si-based feedstock. To reproduce SiNWs via the OAG mechanisms no metal contamination has been intentionally added in the feedstock, while, to induce SiNW formation via VLS growth different percentages of Al (5%, 10% and 15%) as metal catalyst have been considered, in both a Si feedstock and in a SiO<sub>2</sub> feedstock. As far as the gas environment is concerned, we tried with pure Ar as plasma gas as well as with Ar/He and Ar/H<sub>2</sub> mixtures. Hence, the various feedstocks and the different gas conditions were combined to give 30 different procedures. The diverse schemes exploited are summarized in Table 1.

**Table 7.1.** Scheme of the different conditions exploited for the intentional synthesis of ICP-SiNWs.

<u>Feedstock</u>		<u>Carrier Gas</u>	
Si +	SiO <sub>2</sub> +	Ar	Ar +
•0% Al	•0% Al	•pure	
•5% Al		• + H <sub>2</sub> 1 lpm	•He 1 lpm
•10% Al	•10% Al	• + H <sub>2</sub> 2.5 lpm	•He 2.5 lpm
•15% Al			

The main result concerning the intentional production of SiNWs via the ICP systems is related to the fact that SiNWs have been successfully reproduced, but the conditions at which SiNW synthesis occurs have been still kept confidential by Tekna in the perspective of a patent filling. Here, we report some preliminary TEM analyses concerning the sample where SiNWs have been observed. An approach based on TEM investigation has been pursued similarly to the previous class of samples in order to characterize the new nanomaterial, but also to understand the degree of SiNW reproducibility via the ICP technique.

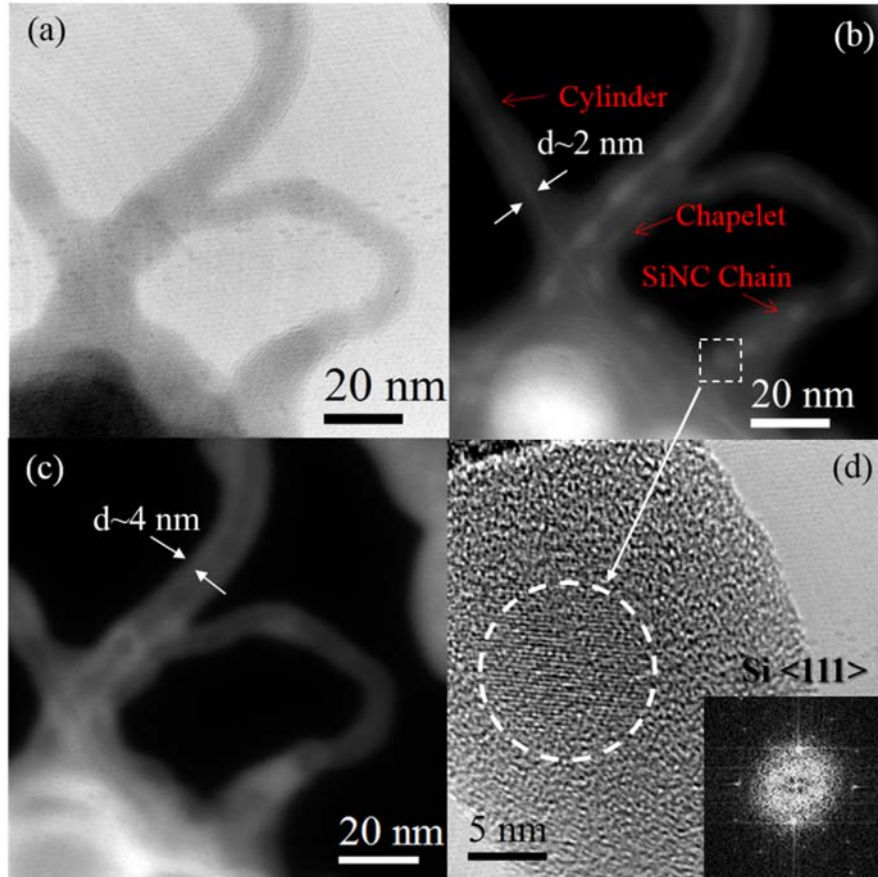


**Figure 7.1.** TEM images of SiNWs reproduced via intentional ICP synthesis: (a) BF TEM; (b) EFTEM image acquired at the Si plasmon energy loss; (c) EFTEM image acquired at the SiO<sub>2</sub> plasmon energy loss; (d) HRTEM depicting a spherical SiNC with the corresponding Fast Fourier Transform.

A bright field (BF) TEM image of the newly as-prepared powder has been reported in Fig. 1(a), while Figs. 1(b) and (c) depict the correspondent EFTEM images acquired at the plasmon energy loss of Si and SiO<sub>2</sub> respectively. From these images it can be noted the presence of a core/shell Si/SiO<sub>2</sub> structure, where the cylindrical core has diameter as thin as 2 nm while the oxide shell is ~4 nm thick. Furthermore, chapelet-like nanostructures have been observed, where almond-shaped SiNCs with diam. of ~3 nm are connected by a SiNW as thin as ~2 nm, as it can be seen in Fig. 1(b). Finally, in Figure 1(b) also the configuration composed of SiNC chains enveloped in a silica nanocylinder can be observed [a HRTEM image of a spherical SiNC is illustrated in Fig. 1(d)]. Hence, the three morphologies of the SiNW core have been reproduced with the same structural characteristics of the previous samples. Moreover, analogously to the previous sample, few percent of SiNWs are shorter with a particle at the tip. Figure 2 displays the EFTEM images correspondent to the BF TEM illustrated in the inset: these images demonstrate that the particle at the tip is composed of neither Si nor SiO<sub>2</sub>. Further EDX

spectroscopic analyses should be performed in order to determine the nature of these particles located at the tip of the SiNWs, most probably being metallic catalysts that promoted SiNW growth in the experimental conditions exploited during this ICP intentional synthesis.

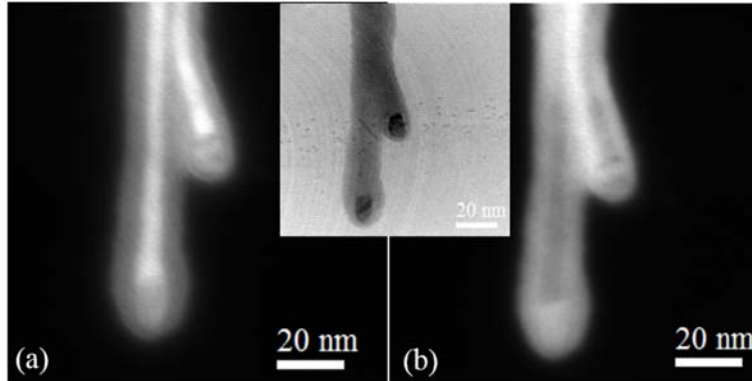


**Figure 7.2.** EFTEM images acquired at the plasmon energy losses of (a) Si and (b) SiO<sub>2</sub> of two SiNWs having a dark particle at their tips, as shown in the inset.

Preliminary studies about the thermal stability of these newly reproduced SiNWs have also been made in order to understand whether they react similarly to the previous ones and develop a thermal-driven instability which is described by the Rayleigh model. To this aim, the newly synthesized SiNWs have been annealed at 1200°C in N<sub>2</sub> ambient gas. A typical EFTEM image of this sample is shown in Fig. 3. Preliminary statistical EFTEM analyses ensure that almost the totality of the SiNWs break up into SiNC chains, but further analyses are demanded to assure that the ratio  $\lambda/R$  is in agreement with the Rayleigh instability phenomenon.

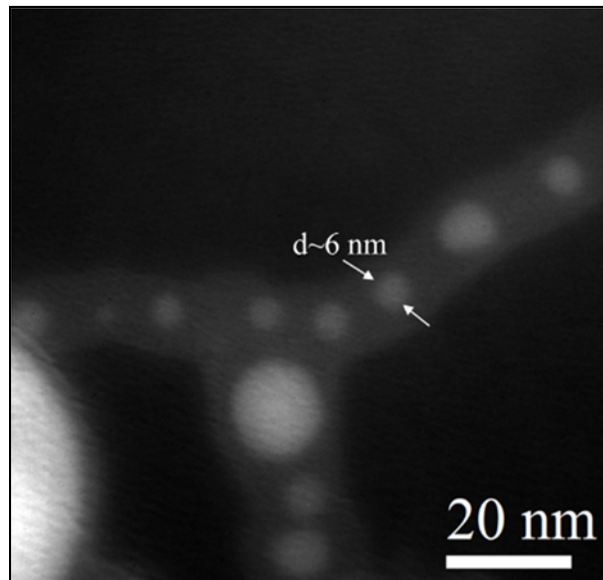


**Figure 7.3.** Representative EFTEM image of the sample annealed at 1200°C in N<sub>2</sub> acquired at the Si plasmon energy loss, showing the SiNC chain configuration.

In conclusion, the intentional synthesis of SiNWs via an ICP-based process has been successfully accomplished. Notably, the ICP reactor exploited for this process presents a quenching zone, thus allowing a slower cooling rate of the in-flight nucleated nanomaterial. Different conditions have been combined to reproduce the SiNW formation inside the ICP system via both OAG and VLS mechanisms. Among the various attempts, the successful procedure which has been demonstrated to reproduce the ICP-SiNWs is still confidential. Preliminary TEM-based investigations attest the presence of core/shell Si/SiO<sub>2</sub> nanostructures, whereas the Si core exhibits the three different morphologies similarly to the previous ones, but with a thinner silica shell. The majority of the newly produced SiNWs is highly likely formed via an OAG mechanism. Moreover, SiNWs with a dark nanoparticle at their tip let us to assume the coexistence of a VLS-based growth. Finally, these ICP-SiNWs transform their shape after thermal treatments, leading to ordered chains of SiNC formation inside the silica NW.

All these results are promising for the systematic synthesis of ultra-thin SiNWs which present remarkable optical properties, owing to the occurrence of both quantum confinement phenomena, and surface effects, related to their increased aspect-ratio.



